



EXHAUST PLUME THERMODYNAMIC EFFECTS ON NONAXISYMMETRIC NOZZLE AFTERBODY PERFORMANCE IN TRANSONIC FLOW

C. E. Robinson
ARO, Inc., a Sverdrup Corporation Company

PROPULSION WIND TUNNEL FACILITY
ARNOLD ENGINEERING DEVELOPMENT CENTER
AIR FORCE SYSTEMS COMMAND
ARNOLD AIR FORCE STATION, TENNESSEE 37389

August 1978

Final Report for Period 24 November — 4 December 1976

Approved for public release; distribution unlimited.

Prepared for

AIR FORCE FLIGHT DYNAMICS LABORATORY/FXM
WRIGHT-PATTERSON AIR FORCE BASE, OHIO 45433

NOTICES

When U. S. Government drawings, specifications, or other data are used for any purpose other than a definitely related Government procurement operation, the Government thereby incurs no responsibility nor any obligation whatsoever, and the fact that the Government may have formulated, furnished, or in any way supplied the said drawings, specifications, or other data, is not to be regarded by implication or otherwise, or in any manner licensing the holder or any other person or corporation, or conveying any rights or permission to manufacture, use, or sell any patented invention that may in any way be related thereto.

Qualified users may obtain copies of this report from the Defense Documentation Center.

References to named commercial products in this report are not to be considered in any sense as an indorsement of the product by the United States Air Force or the Government.

This report has been reviewed by the Information Office (OI) and is releasable to the National Technical Information Service (NTIS). At NTIS, it will be available to the general public, including foreign nations.

APPROVAL STATEMENT

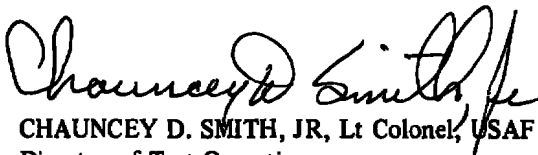
This report has been reviewed and approved.



TOMAS GONZALES, Captain, USAF
Test Director, PWT Division
Directorate of Test Operations

Approved for publication:

FOR THE COMMANDER



CHAUNCEY D. SMITH, JR, Lt Colonel, USAF
Director of Test Operations
Deputy for Operations

UNCLASSIFIED

REPORT DOCUMENTATION PAGE		READ INSTRUCTIONS BEFORE COMPLETING FORM
1 REPORT NUMBER AEDC-TR-78-24	2 GOVT ACCESSION NO.	3 RECIPIENT'S CATALOG NUMBER
4. TITLE (and Subtitle) EXHAUST PLUME THERMODYNAMIC EFFECTS ON NONAXISYMMETRIC NOZZLE AFTERBODY PERFORMANCE IN TRANSONIC FLOW		5 TYPE OF REPORT & PERIOD COVERED Final Report, 24 Nov - 4 Dec 1976
		6. PERFORMING ORG REPORT NUMBER
7. AUTHOR(s) C. E. Robinson, ARO, Inc.		8 CONTRACT OR GRANT NUMBER(s)
9 PERFORMING ORGANIZATION NAME AND ADDRESS Arnold Engineering Development Center Air Force Systems Command Arnold Air Force Station, TN 37389		10. PROGRAM ELEMENT, PROJECT, TASK AREA & WORK UNIT NUMBERS Program Element 62201F Project 1476 Task 02
11 CONTROLLING OFFICE NAME AND ADDRESS Air Force Flight Dynamics Laboratory/FXM Wright-Patterson Air Force Base OH 45433		12 REPORT DATE August 1978
		13. NUMBER OF PAGES 96
14 MONITORING AGENCY NAME & ADDRESS (if different from Controlling Office)		15 SECURITY CLASS. (of this report) UNCLASSIFIED
		15a DECLASSIFICATION/DOWNGRADING SCHEDULE N/A
16 DISTRIBUTION STATEMENT (of this Report) Approved for public release; distribution unlimited.		
17 DISTRIBUTION STATEMENT (of the abstract entered in Block 20, if different from Report)		
18 SUPPLEMENTARY NOTES Available in DDC.		
19 KEY WORDS (Continue on reverse side if necessary and identify by block number) <div style="display: flex; justify-content: space-between;"> <div> wind tunnels turbojet exhaust nozzleless nozzle afterbody plume </div> <div> simulator transonic flow pressure drag </div> </div>		
20 ABSTRACT (Continue on reverse side if necessary and identify by block number) <p>An experimental investigation was conducted in the AEDC Propulsion Wind Tunnel (16T) to determine the effect of exhaust plume thermodynamic properties on a nonaxisymmetric nozzle afterbody. The model consisted of a strut-mounted cone-cylinder with an isolated nozzle afterbody. The shape of the nozzle afterbody was generally based on the early configurations of the General Electric ADEN design. An ethylene/air combustor was used to vary the thermodynamic properties by varying</p>		

UNCLASSIFIED

UNCLASSIFIED

20. ABSTRACT (Continued)

fuel-to-air ratio. Data were obtained at four fuel-to-air ratios representing exhaust plume temperatures of approximately 500°F (cold flow, fuel-to-air = 0), 1,200, 1,500, and 1,900°R. Pressure measurements of the nozzle afterbody surface were obtained from which drag coefficients along the rows of pressure orifices were calculated. The investigation was conducted over a range of Mach numbers from 0.6 to 1.4 at a Reynolds number per foot of 2.5×10^6 . Limited data were obtained at $M_\infty = 0$ and at $M_\infty = 0.7$ for Reynolds numbers of 2.0 and $3.0 \times 10^6/\text{ft}$. Generally, the nozzle afterbody drag decreased with increasing exhaust plume temperature over the entire Mach number range. Limited gas dynamic measurements in the exhaust plume were also obtained.

UNCLASSIFIED

PREFACE

The work reported herein was conducted by the Arnold Engineering Development Center (AEDC), Air Force Systems Command (AFSC), at the request of the Air Force Flight Dynamics Laboratory (AFFDL/FXM), AFSC, under Program Element 62201F. The results presented were obtained by ARO, Inc., AEDC Division (a Sverdrup Corporation Company), operating contractor for the AEDC, AFSC, Arnold Air Force Station, Tennessee. The work was conducted under ARO Project Number P41T-D0A, and the data analysis was completed on August 30, 1977. The manuscript was submitted for publication on March 14, 1978.

CONTENTS

	<u>Page</u>
1.0 INTRODUCTION	5
2.0 APPARATUS	
2.1 Wind Tunnel	5
2.2 Experimental Hardware	5
2.3 Instrumentation	6
3.0 PROCEDURES	
3.1 Experimental Procedures	7
3.2 Data Reduction Procedures	7
4.0 RESULTS	
4.1 Effects of Nozzle Pressure Ratio on Pressure Distribution	9
4.2 Effect of Exhaust Plume Properties on NAB Pressure Distribution	10
4.3 Nozzle Afterbody Pressure Drag Coefficient	11
4.4 Pressure Distribution on Internal Cowl Surface	12
4.5 Exhaust Plume Gas Dynamics	14
5.0 CONCLUSIONS	15
REFERENCES	17

ILLUSTRATIONS

Figure

1. Basic Model Dimensions and Locations in Test Section	19
2. Model Internal Geometry	20
3. Nozzle Afterbody Geometry	21
4. Photograph of Model Installation	22
5. Gas Dynamics Probe Arrangement	24
6. Nozzle Afterbody Pressure Distribution at Mach Number 0.85	26
7. Nozzle Afterbody Pressure Distribution at Mach Number 1.4	34
8. Circumferential Pressure Distribution	42
9. Nozzle Afterbody Pressure Distribution at Four Exhaust Plume Temperatures, $M_\infty = 0.85$	44
10. Effect of Mach Number on Nozzle Afterbody Pressure Distribution, $\theta = 0$	52
11. Pressure Drag Coefficient as Function of NPR for Four Exhaust Plume Temperatures, $M_\infty = 0.85$	59

<u>Figure</u>	<u>Page</u>
12. Effect of Mach Number on Pressure Drag Coefficient at Four Exhaust Plume Temperatures, $\theta = 0$	67
13. Effect of Mach Number on Pressure Drag Coefficient at Four Exhaust Plume Temperatures, $\theta = 180$ deg	74
14. Effect of Free-Stream Mach Number on Pressure Distribution, Internal Cowl Surface at an NPR of 3.0	81
15. Effect of Pressure Ratio on Pressure Distribution, Internal Cowl Surface	83
16. Effect of Exhaust Plume Temperature on Pressure Distribution, Internal Cowl Surface	84
17. Flow Angularity Measured in the Exhaust Plume at Three Downstream Locations, $M_\infty = 0.8$	85
18. Flow Angularity Measured in the Exhaust Plume at Three Downstream Locations, $M_\infty = 0.9$	87
19. Total Pressure Profile of Exhaust Plume at Three Downstream Locations, $M_\infty = 0.85$	88

TABLES

1. Nozzle Afterbody Pressure Tap Locations	89
2. Test Matrix	93
NOMENCLATURE	95

1.0 INTRODUCTION

The next generation of military aircraft probably will be required to meet certain specifications with regard to infrared exhaust plume signatures. In order to obtain information necessary to satisfy this future requirement a series of nozzle afterbody (NAB) configurations has been designed and is being tested. An earlier design of this type was the General Electric ADEN configuration. This NAB design is a nonaxisymmetric shape which does not lend itself to easy analytical predictions of its performance parameters; therefore, extensive cold flow exhaust plume simulation testing has been conducted to experimentally determine the performance of this NAB design. To augment the results and quantify the effect of exhaust plume thermodynamic properties on the nonaxisymmetric NAB performance, the Air Force Flight Dynamics Laboratory (AFFDL/FXM) requested the current investigation. This investigation was designed to experimentally determine the effect of exhaust plume temperature on NAB performance. An ethylene/air combustor was used to provide the exhaust plume with the desired thermodynamic properties. The investigation was conducted at the AEDC in the Propulsion Wind Tunnel Facility (PWT) 16-foot Propulsion Wind Tunnel (16T) over the Mach number range from 0.6 to 1.4. Results from this investigation are documented in this report.

2.0 APPARATUS

2.1 WIND TUNNEL

The AEDC 16-ft Propulsion Wind Tunnel (16T) is a continuous flow, closed-circuit wind tunnel capable of operation within a Mach number range from 0.20 to 1.60. Tunnel 16T can be operated within a stagnation pressure range from 120 to 4,000 psfa, depending on Mach number, with a stagnation temperature variation capability from approximately 80°F to a maximum of 160°F. Tunnel air is removed and replaced with conditioned make-up air from an atmospheric dryer to control the specific humidity of the tunnel air.

2.2 EXPERIMENTAL HARDWARE

The experimental hardware used was the AFFDL/Lockheed isolated nozzle model reported in Refs. 1 and 2. The model is an axisymmetric, strut-mounted cone-cylinder which has provisions for mounting various nozzle afterbody (NAB) configurations on the aft end. The cone has a 14-deg half angle which is faired into the primary model diameter of 9.86 in. The model support system is a tapered strut with an average sweep angle of 35 deg. The strut thickness to chord ratio varied from 0.053 at the model to 0.088 at the tunnel floor. Air for cold flow exhaust simulation and for combustion with

ethylene in the hot exhaust duplication is supplied to the model through passages in the strut. The blockage of the tunnel cross section by the model/strut assembly is 0.88 percent. A dimensional sketch of the model and strut is presented in Fig. 1.

The ethylene/air combustor used to provide hot exhaust jet duplication is described in detail in Refs. 1 and 2. Ethylene (C_2H_4) is a hydrocarbon and when burned in air exhibits thermodynamic properties similar to those of JP-4 burned in air. The internal arrangement of the combustor is shown in Fig. 2.

The external contour of the NAB is a nonaxisymmetric configuration based generally on the early configuration of the General Electric ADEN design. Cross sections at four axial stations as well as the NAB profile are shown in Fig. 3. The upper surface of the NAB extends beyond the throat and forms a cowl whereas the lower surface terminates near the throat (Fig. 3). The exhaust plume will, therefore, be a combination forced expansion, conforming to the boundary provided by the cowl internal surface, and a free expansion from the lower lip of the nozzle.

For structural reasons, the NAB was installed on the isolated body in the inverted position for this experimental program. A photograph of the NAB installed in the tunnel is shown in Fig. 4.

Because of the nonaxisymmetric characteristics of the NAB being investigated, a water jacket cooling system would have been complicated. For this reason, the NAB was fabricated from high temperature Inconel[®] and operated without external cooling.

2.3 INSTRUMENTATION

The primary instrumentation used during this investigation measured model static pressures. One hundred eleven (111) external surface pressure taps were used to measure the pressure distribution of the nonaxisymmetric NAB. In addition, 41 pressure taps were located on the internal surface and the throat of the NAB. The locations are shown in Table 1. The Tunnel 16T precision pressure balance system (PPB) was used to measure the model pressures. The PPB system has uncertainties of ± 2.36 and ± 3.6 psf at differential pressures of 144 and 1,440 psf, respectively. This corresponds to uncertainties in CP of ± 0.008 at CP = 0 and ± 0.012 at CP = 3.0. The CP measurements repeated to within ± 0.001 at duplicate test conditions, however. Mass flow rates of the air and ethylene were measured using critical flow venturis. Exhaust plume temperature was calculated based on fuel-to-air ratio as discussed in Section 3.2.

The exhaust plume Mach number, flow angularity, and total and static pressure distributions were measured with the aid of a traversing/rotating rake. The mechanism (shown in Fig. 5) was capable of translation from 1 to 50 in. downstream from the

nozzle exit. The rake could also rotate 180 deg about its centerline, and the support strut of the rake mechanism could be rotated ± 30 deg from vertical about a point on the test section floor. The various motions (measured with linear potentiometers) allowed a complete x-y-z coordinate mapping of the exhaust plume.

3.0 PROCEDURES

3.1 EXPERIMENTAL PROCEDURES

The technique used to determine the effect of exhaust plume thermodynamic properties on NAB performance was to obtain experimental data at constant plume properties (constant fuel-to-air ratio) over a range of nozzle pressure ratios for each Mach number. The experimental procedure is outlined below.

1. Wind tunnel Mach number and Reynolds number conditions were established, and jet-off data were obtained.
2. Cold flow was established through the model, and a series of nozzle pressure ratios was set. Data were obtained at each ratio.
3. The combustor was ignited, and the fuel/air ratio was set to obtain the desired temperature. A series of nozzle pressure ratios was set by varying fuel and airflow to maintain a constant fuel/air ratio. Data were obtained at each nozzle pressure ratio. The nozzle pressure ratio survey was conducted at three fuel/air ratios.

3.2 DATA REDUCTION PROCEDURES

The primary performance parameters included in this report are calculated directly from the pressure measurements. Pressure coefficients (CP) are calculated from

$$CP_i = \frac{P_i - P_\infty}{q_\infty} \quad (1)$$

where the subscript i represents the individual pressure measurements, the subscript ∞ represents the free-stream static conditions, and q is the dynamic pressure.

Because of the nonaxisymmetric shape of the nozzle afterbody and lack of sufficient static pressure measurements, a definitive integration scheme for calculating total drag was not formulated. Pressure drag was calculated for each row of pressures, however, using the following relationship:

$$CPD\theta = -\frac{1}{A_{Ref}} \sum_i CP_i (A\theta_i) \quad (2)$$

where A_{Ref} is the maximum body cross-sectional area, CP_i is the local pressure coefficient, and $A\theta_i$ is the forward projection of the local area associated with the i^{th} pressure tap. The area is based on a longitudinal 1-in.-wide strip along the body axis with the pressure located at the center. (Physical measurements of the NAB contour were used.) The term θ refers to the angular location of the subject row of pressures (see Fig. 3 and Table 1).

The nozzle total pressure was calculated from the average of four static pressure measurements located at 90-deg intervals in the combustor, using the isentropic equation

$$PTC = PCS \left(\frac{PT}{P} \right) \quad (3)$$

The term (PT/P) is the subsonic pressure ratio based on the nozzle contraction ratio of 2.77 and the ratio of specific heats, γ , of the exhaust products based on 100-percent combustion efficiency. Since PT/P is an extremely weak function of γ (PT/P decreases approximately 0.15 percent for a change in γ from 1.40 to 1.26), use of γ based on 100-percent combustion efficiency introduces no significant error in the calculation of PTC.

Exhaust plume total temperature was calculated from a fifth-order numerical equation with fuel/air ratio (F/A) as the independent parameter, as follows:

$$TGAS = \sum_{i=1}^5 C_i (F/A)^i \quad (4)$$

Two temperatures were calculated using this relationship. The first (TTGAS) was based on 100-percent combustion efficiency and utilized the theoretical thermodynamic properties of ethylene to determine the constants. For the second exhaust temperature (TGAS) calculated from the above relationship [Eq. (4)], experimental measurements of temperature versus F/A were used to determine the required constants. These experimental measurements were taken from a previous investigation (Ref. 2).

Measurements from hemispherical head gas dynamics probes were used to calculate static pressure, Mach number, and flow angularity in the jet from the following equations:

$$\text{Static pressure, } PS = \frac{\sum KP_i (P_i)}{\sum KP_i}, \quad (5)$$

where KP_i is either "1" or "0" and i varies from 1 to 4.

$$\text{Mach number, } MP_i = \sum_{k=0}^5 B_k (PS/PT), \quad (6)$$

where B_k values are constants determined experimentally from the calibration of similar hemispherical probes.

$$\text{Flow pitch angularity, } \alpha = CC_2 \frac{P_1 - P_3}{PT}, \text{ deg}, \quad (7)$$

where CC_2 values are constants taken from calibrations of similar probes. Flow yaw angularity, β , is calculated from Eq. (7) by substituting P_2 and P_4 for P_1 and P_3 .

4.0 RESULTS

An experimental program was conducted to investigate the effect of exhaust plume thermodynamic properties on the performance of a nonaxisymmetric NAB. Axial pressure distributions along the model surface were measured at eight radial positions and integrated in the manner described in Section 3.2 to obtain pressure drag. Data were obtained at Mach numbers from 0.6 to 1.4 (limited data were obtained at $M_\infty = 0$) over a range of nozzle pressure ratios (NPR) from 1.0 to 6.0. Data were obtained at four approximate exhaust plume temperatures (500, 1,200, 1,500, and 1,900°R) at each tunnel condition. The complete matrix of test conditions investigated during this program is shown in Table 2.

In addition to the effects of exhaust properties on external pressure distribution, the distribution along the internal surface of the cowl will be discussed. Also, limited gas dynamic measurements in the exhaust plume were obtained and will be discussed.

4.1 EFFECTS OF NOZZLE PRESSURE RATIO ON PRESSURE DISTRIBUTION

The axial pressure coefficient distribution for each of the eight rows of orifices is shown in Figs. 6a through h for a total gas temperature of 509°R, a Mach number of 0.85, and NPR values of 2, 3, 4, and 5. The critical pressure coefficient corresponding to Mach number 1, based on one-dimensional isentropic flow theory, is -0.3 for the Mach number presented here. As shown by the pressure coefficient distribution, this critical CP was not reached on the external surface. For all eight rows of pressures, recompression

occurred over most of the length of the NAB. Nozzle pressure ratio, because of the nonaxisymmetrical shape of the NAB, affected the rows of orifices in a different manner. Around the lower portion of the NAB (from $\theta = 90$ to 270 deg) the expansion and recompression maintained a lower level of CP at the lower pressure ratio and generally increased with increasing pressure ratio (Figs. 6c through g). Over the surface of the extended cowl the opposite effect was observed (Figs. 6a, b, and h), with the exception of the highest pressure ratio. At an NPR of 5, the trend was reversed, and a stronger recompression was reached at the higher pressure ratio.

The axial pressure coefficient distribution for each of the eight rows of pressure orifices is shown in Figs. 7a through h for a gas total temperature of 508°R , a supersonic Mach number of 1.4, and pressure ratios of 2, 3, 4, and 5. Because of the nonaxisymmetric nature of the NAB the shock location is different for the various portions of the NAB. In the upper quadrant, from 0 plus or minus 45 deg, the shock occurs at an axial station of approximately 13 in. On the NAB sides at 90 and 270 deg, the shock occurs at approximately 9 in., and in the lower quadrant, the shock occurs at 7 in. In the upper quadrant, increasing NPR moves the shock location forward, except at the highest NPR. The shock location and recompression at an NPR of approximately 5 on the model upper quadrant occurred downstream of that observed at an NPR of approximately 4. On the sides and lower quadrant of the model, the shock location moved forward with increasing NPR.

Since the nozzle afterbody is nonaxisymmetric, the expansion/recompression variation with NPR is different for each of the rows of pressure orifices (see Figs. 6a through h). Because the variation is different, different levels of static pressure occur around the external surface at the same axial position. These differences in static pressure introduce crossflow around the external surface. Figures 8a through g show the NAB circumferential pressure distributions at eight axial stations for a free-stream Mach number of 0.85. The gaps in the curves at the downstream positions result because the cowl extends 6 in. downstream of the lower surfaces. Unfortunately, no flow visualization was used in this experimental effort, and as a result the extent of crossflow cannot be documented.

4.2 EFFECT OF EXHAUST PLUME THERMODYNAMIC PROPERTIES ON NAB PRESSURE DISTRIBUTION

The NAB performance at three fuel-to-air ratios resulting in exhaust plume total temperatures of approximately $1,200$, $1,500$, and $1,900^\circ\text{R}$ was investigated, as was the NAB performance with a cold flow (no combustion, $T \cong 500^\circ\text{R}$) exhaust plume, for

comparative purposes. Exhaust plume temperature will be used in this discussion to indicate the different exhaust plume thermodynamic properties.

The effect of exhaust plume temperature and specific heat ratio on the NAB pressure distribution at a free-stream Mach number of 0.85 and an NPR of 3.0 is shown in Figs. 9a through h. The level of CP along the NAB surface generally increases with increasing exhaust plume temperature for all eight rows of pressure orifices. However, the CP distribution measured with the cold flow exhaust plume tends to cross over from the minimum value to the maximum recompression near the end of the nozzle afterbody. The reason for this crossover is not understood by the author.

Nozzle afterbody pressure distributions were experimentally determined at seven free-stream Mach numbers during this investigation (Table 2). The behavior of the CP distributions was the same at all subsonic Mach numbers, and those distributions shown in Figs. 6a through h for a free-stream Mach number of 0.85 are typical. The CP distribution along the 0-deg pressure orifice row is shown in Figs. 10a through g for each of the free-stream Mach numbers investigated. At the two supersonic Mach numbers (1.2 and 1.4), the recompression is more strongly influenced by the exhaust plume properties (Figs. 10f and g). At Mach number 1.4 the general trend of increasing recompression with increasing exhaust plume temperature observed at the subsonic Mach number is still valid. However, at Mach number 1.2 the strongest recompression is experienced at the intermediate temperature of 1,441°R, whereas the weakest recompression is observed at the highest temperature, 1,832°R (Fig. 10f).

4.3 NOZZLE AFTERBODY PRESSURE DRAG COEFFICIENT

The CP distributions were integrated in the manner described in Section 3.2 to obtain pressure drag coefficient ($CPD\theta$) along each of the eight rows of pressure orifices. The pressure drag coefficient for each of these orifice rows is shown in Figs. 11a through h as a function of nozzle pressure ratio for each of the exhaust plume temperatures investigated, at a free-stream Mach number of 0.85. The $CPD\theta$ variation with NPR displays different characteristics as a function of radial position on the NAB surface. On the external cowl surface (orifice rows at 0, 45, and 315 deg), $CPD\theta$ increases with increasing NPR until a peak is reached, at an NPR of 4.0 (Figs. 11a, b, and h). $CPD\theta$ then decreases with further increases in NPR. At angular positions of 90 and 270 deg (the NAB sides), $CPD\theta$ showed only a slight decrease with increasing NPR (approximately three drag counts)(Figs. 11c and g). On the lower portion of the NAB, $CPD\theta$ decreased with increasing NPR (Figs. 11d through f).

The pressure drag coefficient generally decreased with increasing exhaust plume temperature on the external surface of the cowl (Figs. 11a, b, and h) as well as on the lower surface of the NAB, which has a very high closure rate. This trend of decreasing CPD with increasing exhaust plume temperatures is consistent with NAB temperature effects measured on axisymmetrical NAB's which were reported in Refs. 1 and 2. No effect of exhaust plume temperature variation was observed on the NAB sides (90 and 270 deg), however.

The effect of Mach number on $CPD\theta$ will be shown for both the 0- and the 180-deg pressure orifice rows because of the different characteristics of $CPD\theta$ variation with NPR caused by geometry. Figures 12a through g present $CPD\theta$ at the different levels of exhaust plume temperature as a function of NPR for each of the eight Mach numbers (Table 2) for the 0-deg pressure orifice row. The behavior of $CPD\theta$ with both increasing exhaust plume temperature and NPR was the same as discussed in the paragraph above for all subsonic Mach numbers investigated. For Mach number 1.2, however, the variation of $CPD\theta$ with NPR at various temperatures does not conform to this classic behavior. The drag coefficient decreases with increasing NPR until a minimum value is reached, at which point $CPD\theta$ increases with increasing NPR (Fig. 12f). The pressure ratio at which this minimum is obtained appears to be a function of exhaust plume temperature. The minimum value of $CPD\theta$ occurred at an NPR of approximately four for both the cold flow exhaust plume temperature (500°R) and the highest exhaust plume temperature (~1,910°R). At the intermediate temperatures, ~1,200 and ~1,500°R, the minimum $CPD\theta$ occurred at an approximate NPR of 5. The reason for this behavior or its dependence on exhaust plume temperature is unknown. A full investigation of the behavior would require more NPR's and exhaust plume temperatures. The same characteristics were observed at Mach number 1.4 with the exception that the minimum value of $CPD\theta$ was observed at a pressure ratio of 5 for all three combustion temperatures.

Figures 13a through g present the $CPD\theta$ variation with NPR for the seven Mach numbers for the 180-deg row of pressure orifices. $CPD\theta$ decreases with increasing NPR for all Mach numbers presented. The effect of exhaust plume temperature on the $CPD\theta$ variation with NPR is larger for the supersonic Mach numbers than for the subsonic Mach numbers. When the plume was composed of combustion products, $CPD\theta$ decreased with increasing exhaust plume temperature at a given value of NPR. However, the cold flow plume produced the lowest CPD except at $M_\infty = 1.4$.

4.4 PRESSURE DISTRIBUTION ON INTERNAL COWL SURFACE

The nonaxisymmetric NAB design utilized during this investigation has a large, contoured cowl which extends beyond the nozzle throat (Fig. 3). The internal surface of

this cowl acts as an expansion/deflection nozzle contour for the exhaust plume. The remainder of the NAB terminates just downstream of the nozzle throat, and the exhaust plume is allowed unrestricted expansion. The pressure distribution on the internal cowl surface is affected by free-stream Mach number, nozzle pressure ratio, and exhaust plume thermodynamic properties. The effects of these parameters are discussed in the following sections.

4.4.1 Effect of Free-Stream Mach Number

The effect of free-stream Mach number on the pressure distribution of the internal cowl surface (at $\theta = 0$) is shown in Figs. 14a through e at an NPR of 3.0 and an exhaust plume temperature of approximately 500°R (cold flow). The pressure distribution shows a normal expansion to a pressure ratio of approximately 0.23, at which point a shock occurs. The free-stream pressure ratio is 0.32. Therefore, the ratio at the shock of 0.23 represents an over-expansion of 28 percent. (Theoretically, according to Sutton (Ref. 3), a convergent-divergent nozzle can sustain an over-expansion of 60 percent.) Two subsonic free-stream Mach numbers are shown in Figs. 14b and c ($M_\infty = 0.6$ and 0.85). The shock location is approximately the same for both these subsonic Mach numbers as for the $M_\infty = 0$ case. The over-expansion for both subsonic Mach numbers was 30 percent, which is consistent with the no external flow case.

The shock location on the internal cowl surface for free-stream Mach numbers of 1.2 and 1.4 moved downstream from the "no external flow" case by approximately 1 in. (Figs. 14d and e). An over-expansion of approximately 51 percent was sustained on the cowl surface at these supersonic Mach numbers.

The present data indicate no observable effects of external free-stream Mach number on the internal cowl surface pressure distribution for subsonic Mach numbers. For supersonic free-stream Mach numbers, however, the shock location moves downstream, and the over-expansion is increased.

4.4.2 Effect of Nozzle Pressure Ratio

The effect of nozzle pressure ratio on the pressure distribution of the internal cowl surface at $\theta = 0$ is shown for two selected Mach numbers in Figs. 15a and b. Pressure ratios of 2, 3, 4, and 5 are shown. For the subsonic Mach number (0.85), the location of the shock moves downstream with increasing NPR. The over-expansion prior to the shock was 16, 28, 36, and 35 percent for NPR's of 2, 3, 4, and 5, respectively. The shock location also moves downstream with increasing NPR for Mach number 1.4 (Fig. 15b). The over-expansion is relatively constant at about 58 percent for pressure ratios of 2, 4, and 5 and is 47 percent at an NPR of 3.

4.4.3 Effect of Exhaust Plume Temperature

The effect of exhaust plume temperature on the pressure distribution of the internal cowl surface is presented in Figs. 16a and b for free-stream Mach numbers 0.85 and 1.4 at an NPR of 3.0. Exhaust plume temperatures of approximately 500 (cold flow) 1,200, 1,500, and 1,900°R are presented. For the subsonic Mach number the location of the shock moves downstream with increasing exhaust plume temperature (Fig. 16a). The shock location is farthest downstream for TGAS of about 1,200°R; however, the pressure ratio shown is approximately 3.3, rather than the 3.0 used for the remainder of the data. This increase in NPR would tend to move the 1,200°R TGAS shock location further downstream and augment the effect of temperature on shock location.

The shock location at the supersonic Mach number (Fig. 16b) is in the same position for the exhaust plume temperatures of 1,200, 1,500, and 1,900°R and is upstream of that observed for the cold flow case. The general shape of the pressure distribution curve for the cold flow case is different from that for the exhaust plume at elevated temperatures.

4.5 EXHAUST PLUME GAS DYNAMICS

A probe system which was designed to map the exhaust plume from near the nozzle exit plane to approximately 36 in. downstream was used to obtain limited gas dynamics measurements. Gas dynamic measurements were made at two subsonic Mach numbers (0.8 and 0.9) at three axial positions downstream from the nozzle exit plane ($XD = 1, 9,$ and 21.7 in.). Flow angularity and total pressure profile measurements will be discussed.

Flow angularity measurements are presented in Figs. 17a through f for the three axial stations. Pitch and yaw measurements were obtained in the horizontal plane across the plume at a free-stream Mach number of 0.80. The opening of the nozzle exit is shown for reference. In the survey plane near the cowl tip ($XD = 1$) large gradients in flow angularity were observed. The probe consisted of a rake with two hemispherical flow angularity heads located 5.2 in. apart. The different symbols represent the independent measurements from these two probes. The trends measured with the two independent probes agree well; however, the absolute value of the flow angle measurement is systematically different between the two measurements. This difference in the absolute values is believed to be caused by a probe misalignment with the rake axis. The variation of α , which represents the angle in the z-plane (pitch), horizontally across the plume at $XD = 1$ is symmetric and reaches a peak at the plume centerline (Fig. 17a). The variation of β , which represents the angle in the y-plane (yaw) horizontally across the plume at $XD = 1$ is shown in Fig. 17d. As the rake moves from right to left across the flow field the yaw angle assumes a negative value of 12 deg near the plume

boundary. The negative yaw angle indicates that the flow is expanding away from the plume centerline. As the probe moves across the plume, the yaw angle increases toward a value of zero on the plume centerline. No data were obtained in the region immediately to the left of the plume centerline. However, the dashed curve in Fig 17d is the probable profile shape, assuming that the flow on the left expands away from the centerline in the same manner as does that on the right. At the two downstream stations ($XD = 9$ and 21.7) the large gradients in β horizontally across the plume observed at $XD = 1$ were not present (Figs. 17e and f). The symmetrical variation in α across the plume was observed at both $XD = 9$ and $XD = 21.7$; however, the magnitude of the variation decreased with increasing distance downstream (Figs. 17b and c).

Figures 18a through c present the flow angularity in the horizontal plane (β) at the three axial stations for $M_\infty = 0.90$. The flow angularity measurements obtained agree closely with those measured at $M_\infty = 0.80$. Therefore, this increase in free-stream Mach number had no significant effect on the exhaust plume flow angle measurements.

The total pressure profiles across the horizontal plane at $M_\infty = 0.80$ are presented in Figs. 19a through c for the three axial positions ($XD = 1, 9$, and 21.7). At the $XD = 1$ station a large gradient in total pressure was measured across the nozzle exit face (Fig. 19a). A peak in the total pressure profile was observed. This peak in pressure profile is characteristic of the ethylene/air combustor and is believed to be caused by the placement of the doughnut ring flame holder. The total pressure gradient across the horizontal plane decreased at the $XD = 9$ plane and was essentially dissipated at the $XD = 21.7$ plane (Figs. 19b and c).

5.0 CONCLUSIONS

The experimental results of an effort to document the performance of a nonaxisymmetric nozzle afterbody (NAB) based on the early configuration of the General Electric ADEN nozzles are summarized below. Nozzle total pressure ratio and exhaust plume temperature were varied over a range of transonic Mach numbers.

1. At a subsonic Mach number of 0.85, recompression occurred over almost the entire length of the NAB. On the lower surface of the NAB, the recompression level increased with increasing nozzle pressure ratio. On the external surface of the extended cowl the recompression level decreased with increasing nozzle pressure ratio except for the highest nozzle pressure ratio (Fig. 6).

2. The afterbody shock at supersonic Mach numbers occurred at varying axial stations because of the nonaxisymmetric design. Over the entire surface of the NAB, however, the highest level of recompression was achieved at the largest NPR (Fig. 7).
3. The recompression on the NAB surface increased with increasing exhaust plume temperature for both the supersonic and subsonic Mach numbers (Figs. 9 and 10). Exhaust plume temperature had a more pronounced effect at the supersonic free-stream Mach numbers.
4. The integrated pressure drag coefficient (CPD) on the upper external cowl surface increased to a maximum value at a nozzle pressure ratio of approximately 4.0 and then decreased with further pressure ratio increases at the subsonic Mach numbers. At the supersonic free-stream Mach numbers, CPD decreased to a minimum value and then increased with increasing nozzle pressure ratio. For both subsonic and supersonic cases the lower surfaces of the nozzle afterbody, CPD, decreased with increasing nozzle pressure ratio.
5. Integrated pressure drag coefficient (CPD) generally decreased with increasing exhaust plume temperature for the subsonic Mach numbers. At the supersonic Mach numbers, the exhaust plume temperature affected the nozzle pressure ratio at which the minimum drag occurred (Figs. 12 and 13).
6. A variation in free-stream Mach number through the subsonic range displayed no observable effect on the pressure distribution of the internal cowl surface. For supersonic free-stream Mach numbers, the shock location moved downstream from the position observed with no external flow. The over-expansion also increased, over that observed with no external flow, at the supersonic free-stream Mach numbers (Fig. 14). Increasing the nozzle pressure ratio moved the shock location downstream for both subsonic and supersonic Mach numbers (Fig. 15). The shock location on the internal cowl surface also moved downstream with increasing exhaust plume temperatures for the subsonic free-stream Mach numbers. For the supersonic free-stream Mach number with combustion products, the shock was located in a fixed position which was further upstream than was the cold flow shock location. The characteristic shape of the pressure distribution for the cold flow was different from that for the three higher exhaust plume temperature cases (Fig. 16).

7. At an axial station 1 in. downstream from the cowl tip, the steep flow angular gradients measured in the yaw plane as the plume is traversed horizontally from right to left indicate that the flow is expanding away from the centerline. The variation of the pitch angle in the horizontal plane was less severe than was the yaw angle. The gradients measured in both yaw and pitch flow angles dissipated and were not measured at the two downstream stations (Fig. 17). No effect of Mach number was noted over the limited range investigated ($M_\infty = 0.80$ and 0.90) (Figs. 17 and 18).
8. A steep gradient in total pressure was measured across the nozzle exit at the horizontal plane close to the cowl tip. The gradient dissipated at the downstream positions (Fig. 19).

REFERENCES

1. Robinson, C. E. and High, M. D. "Exhaust Plume Temperature Effects on Nozzle Afterbody Performance over the Transonic Mach Number Range." AEDC-TR-74-9 (AD781377), July 1974.
2. Galigher, L. L., Yaros, S. F., and Bauer, R. C. "Evaluation of Boattail Geometry and Exhaust Plume Temperature Effects on Nozzle Afterbody Drag at Transonic Mach Numbers." AEDC-TR-76-102 (ADA030852), October 1976.
3. Sutton, George P. Rocket Propulsion Elements: An Introduction to the Engineering of Rockets. John Wiley and Sons, Inc., New York, 1956 (Second Edition).

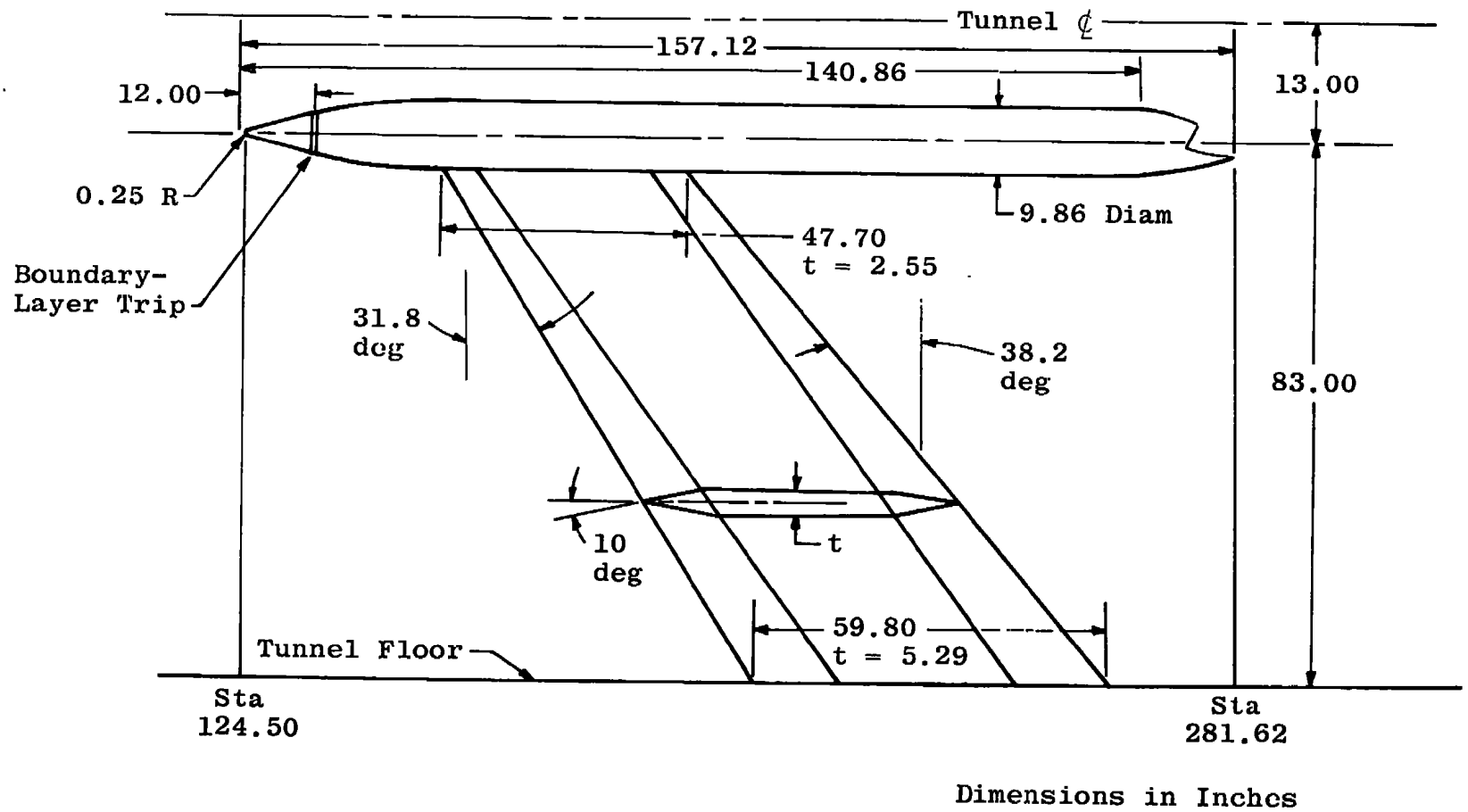


Figure 1. Basic model dimensions and locations in test section.

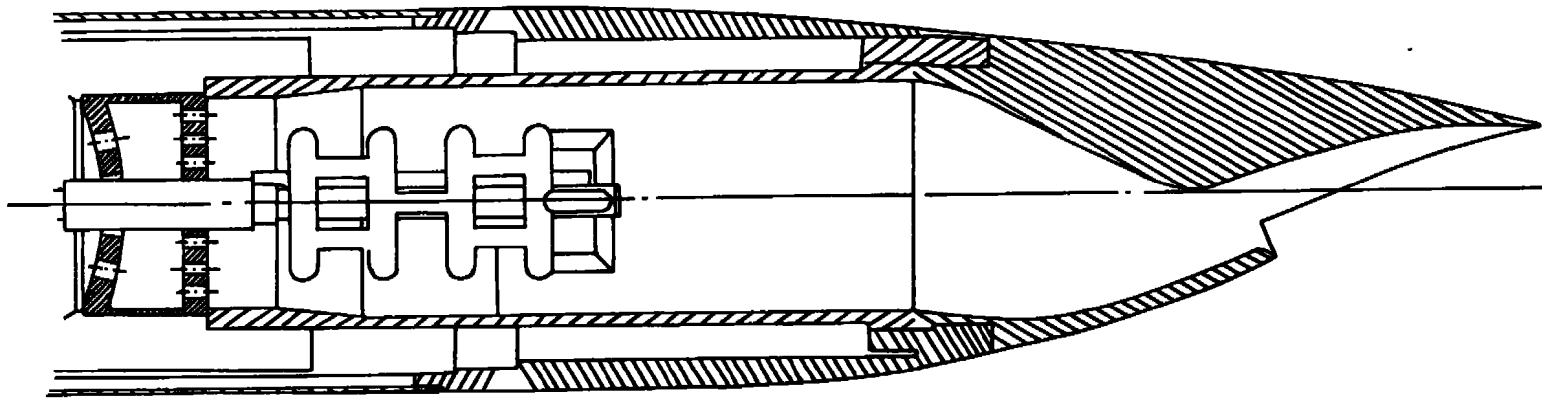


Figure 2. Model internal geometry.

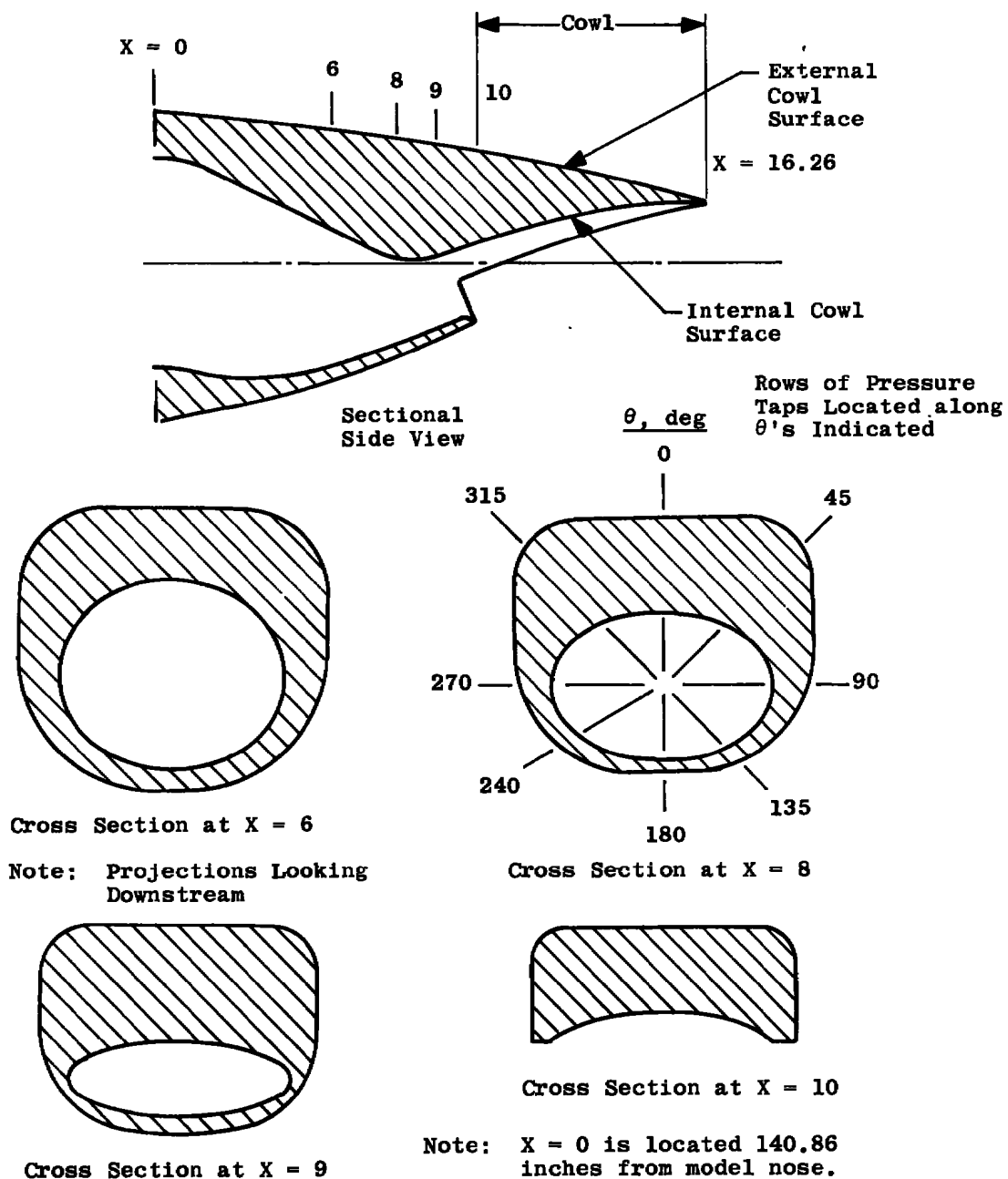
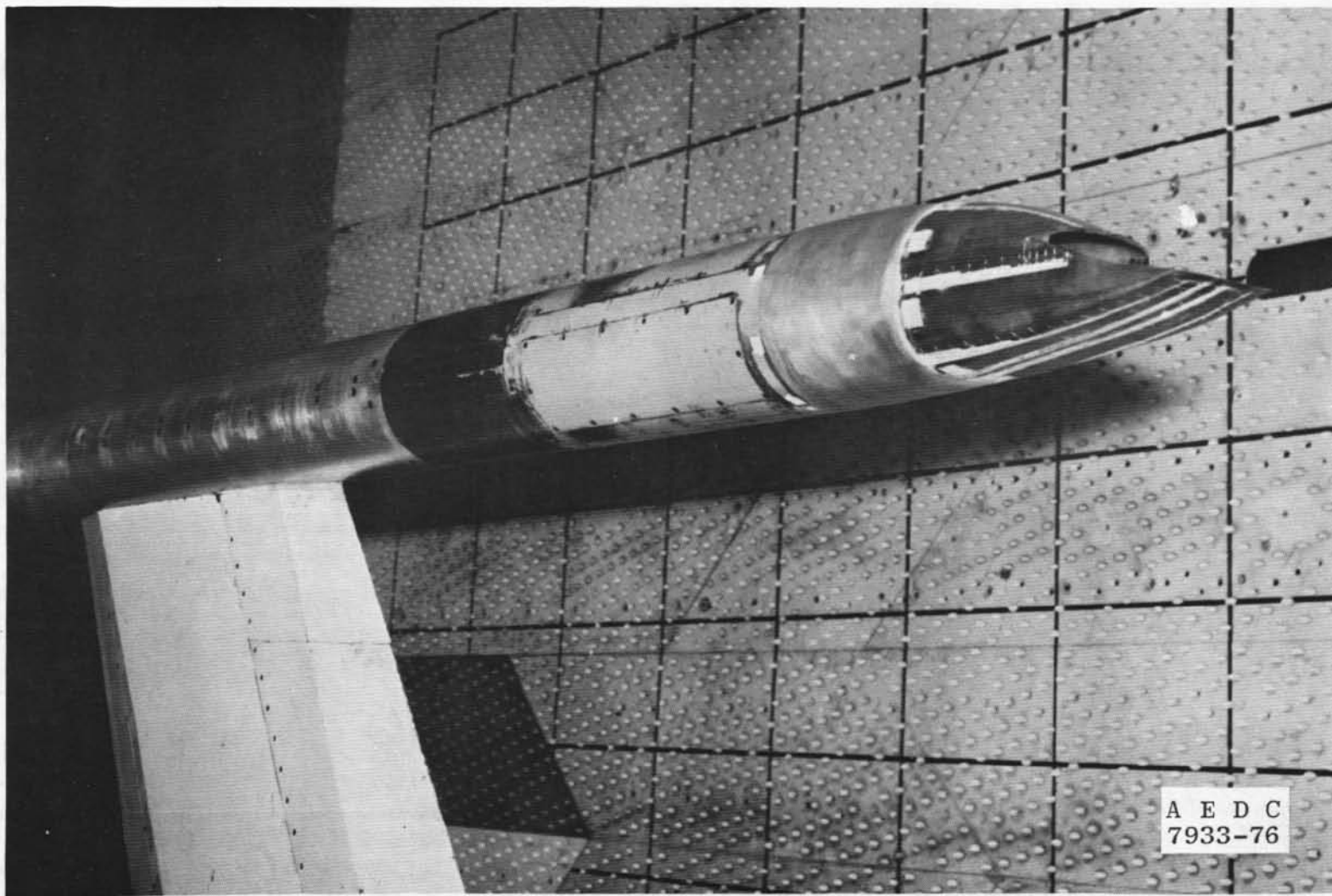
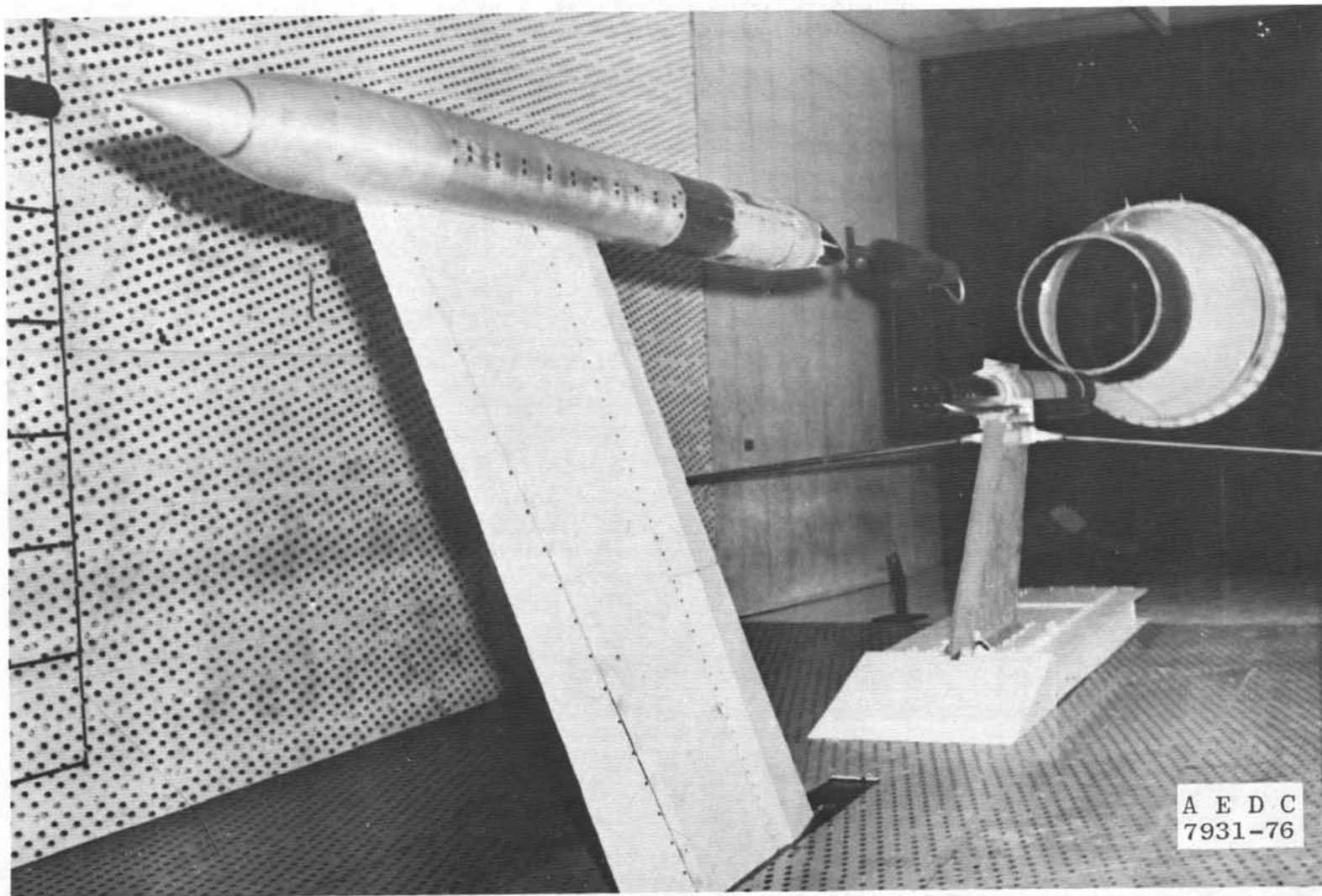


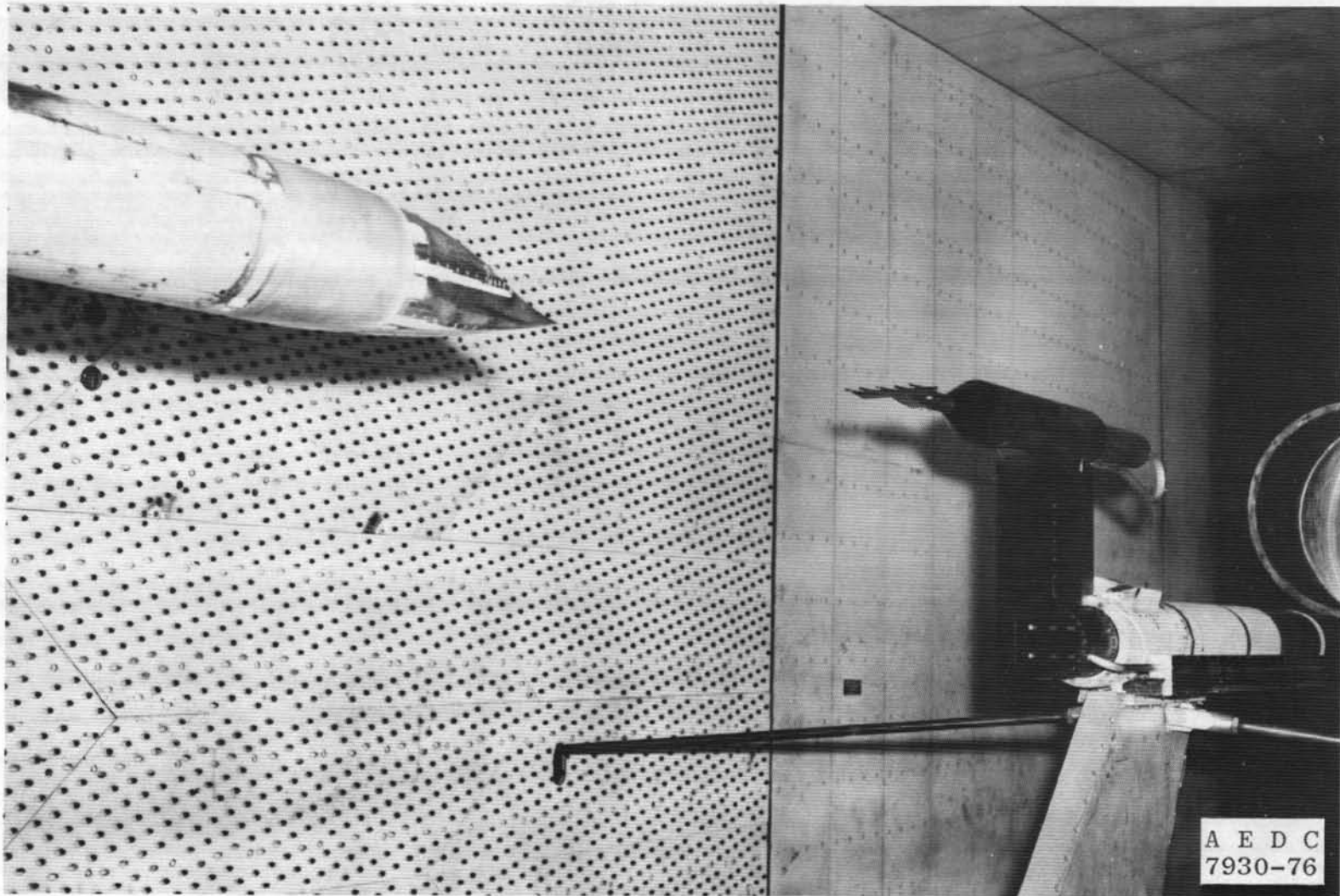
Figure 3. Nozzle afterbody geometry.



a. View of NAB looking forward
Figure 4. Photograph of model installation.

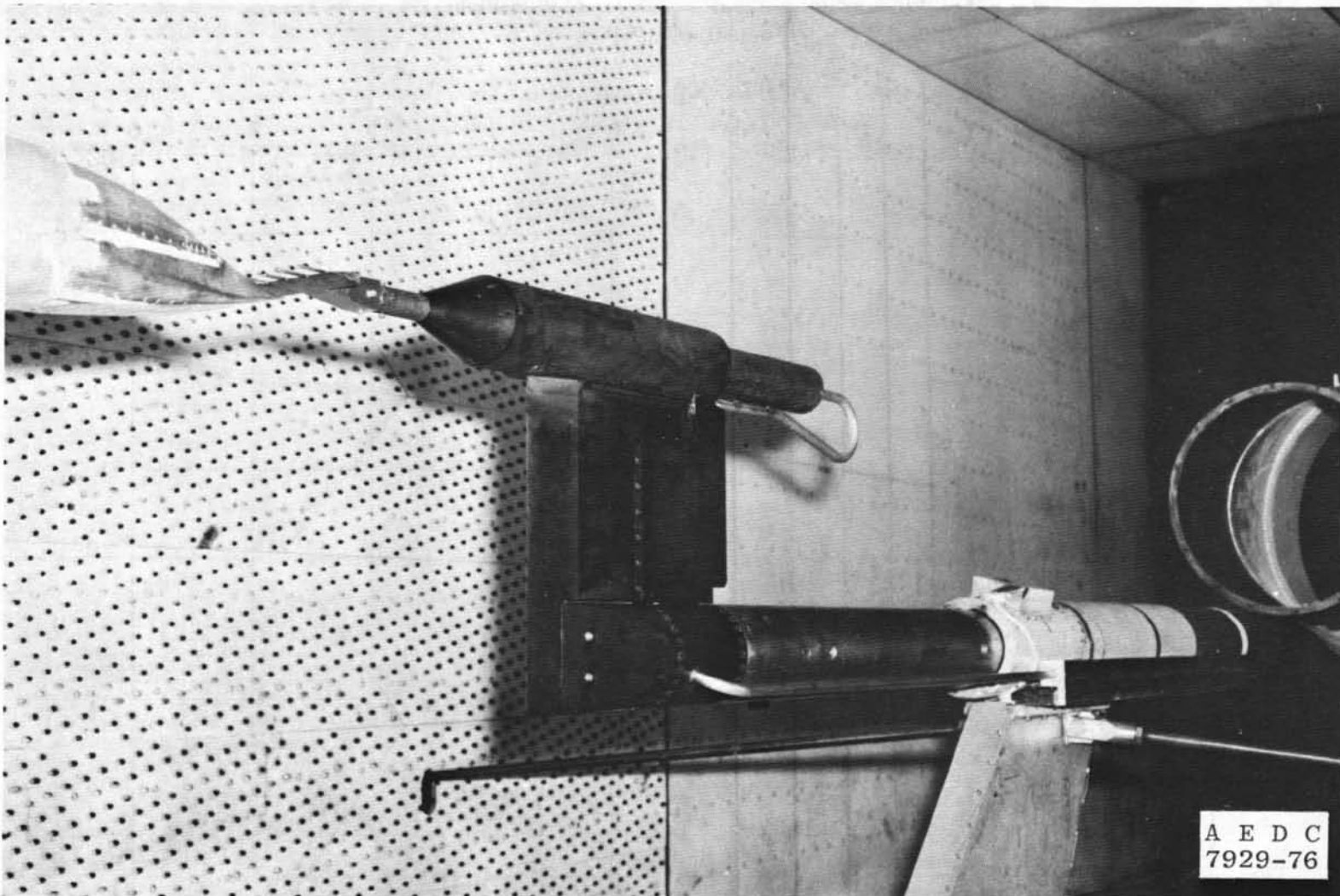


b. Overall view of model and gas dynamics rake, looking downstream
Figure 4. Concluded.

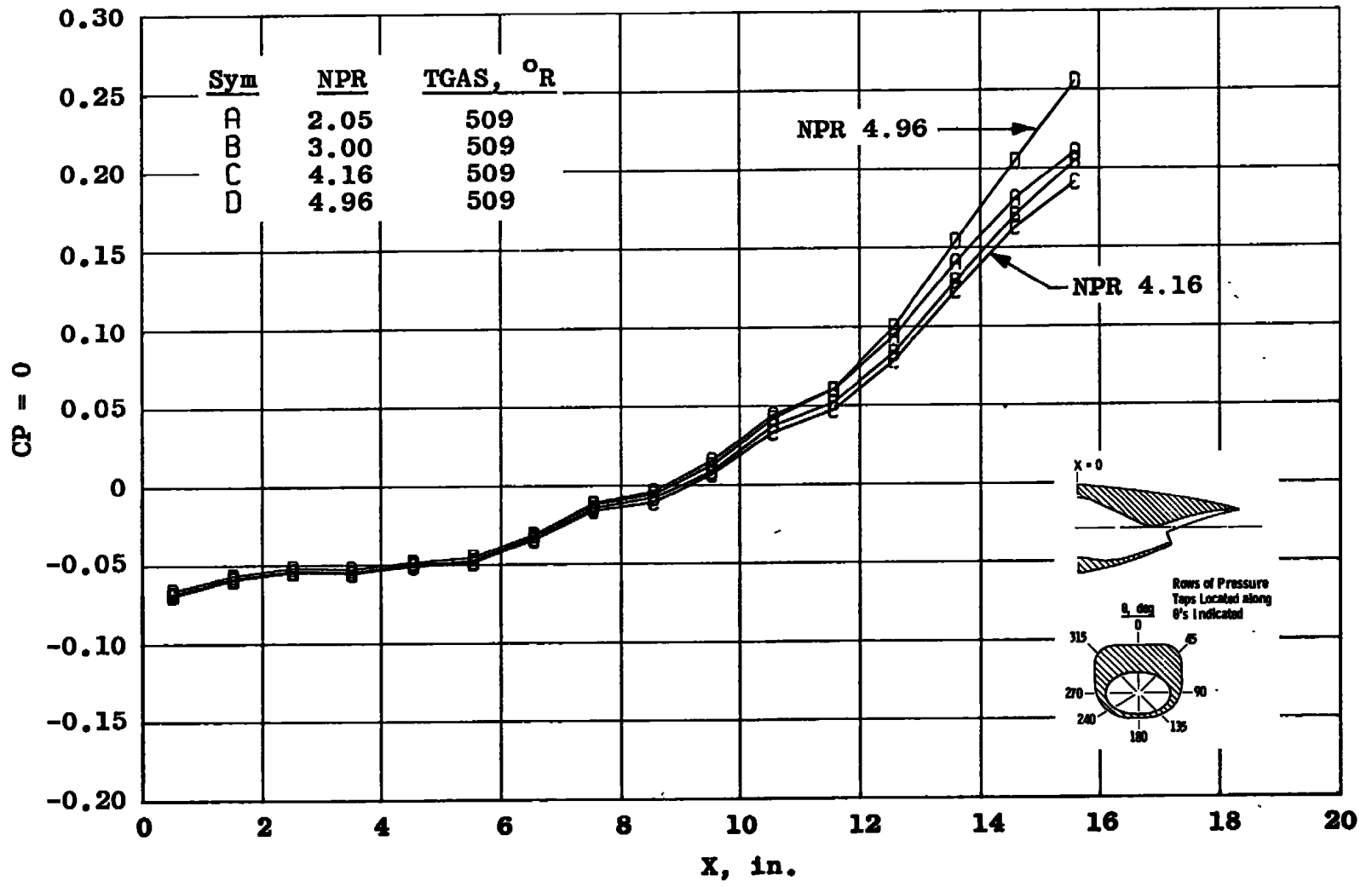


a. Fully retracted

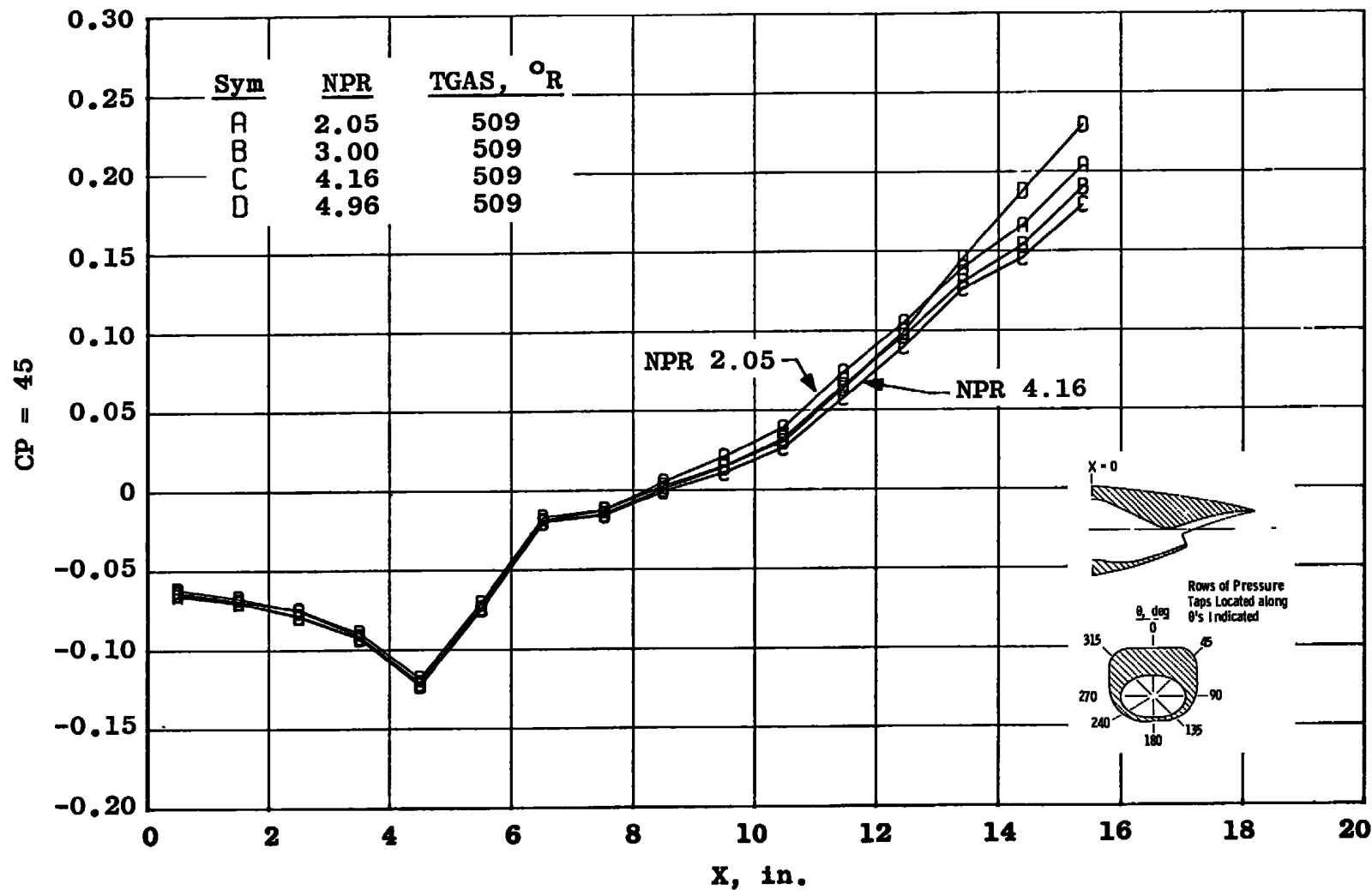
Figure 5. Gas dynamics probe arrangement.



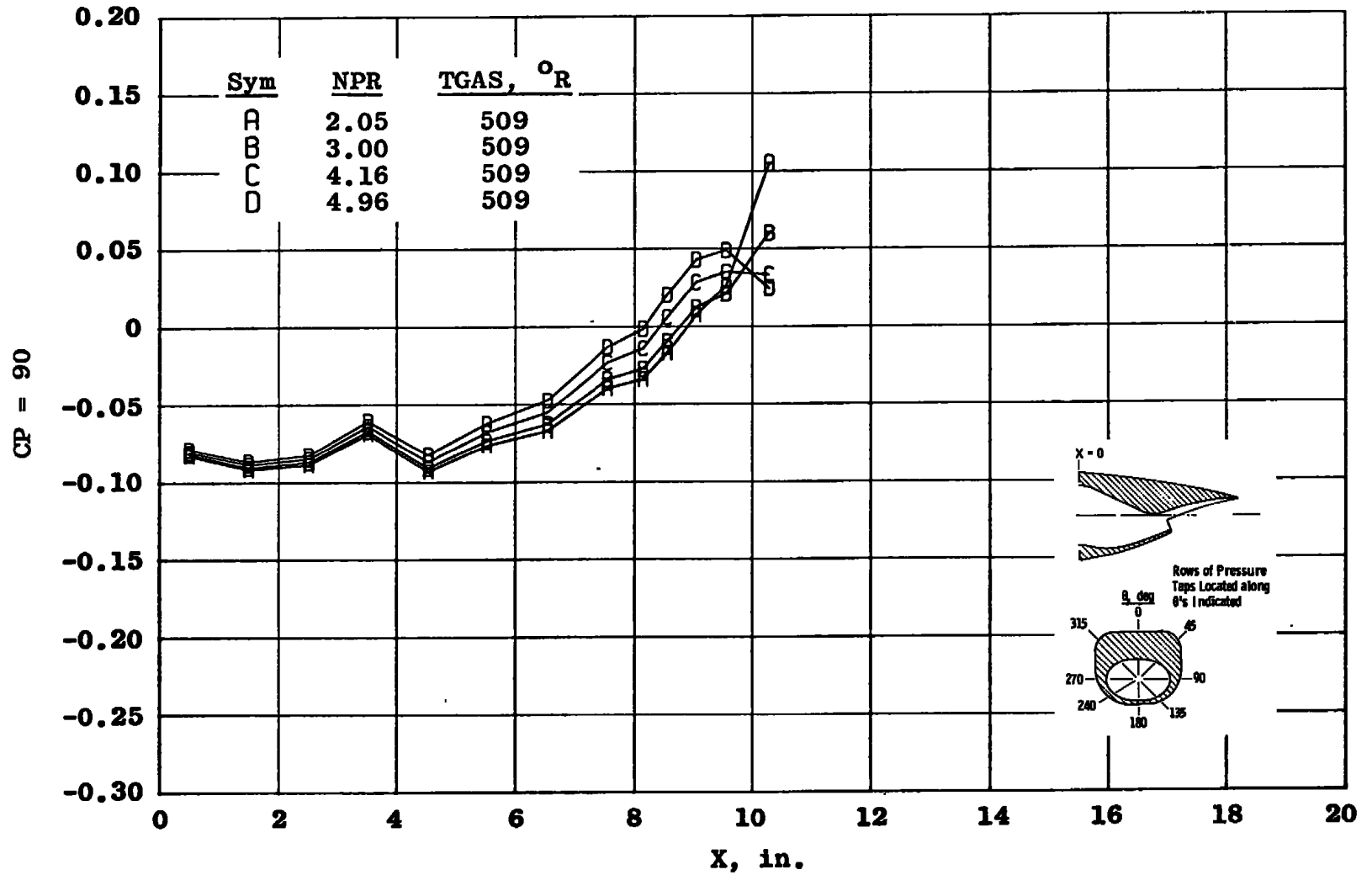
b. Fully extended
Figure 5. Concluded.



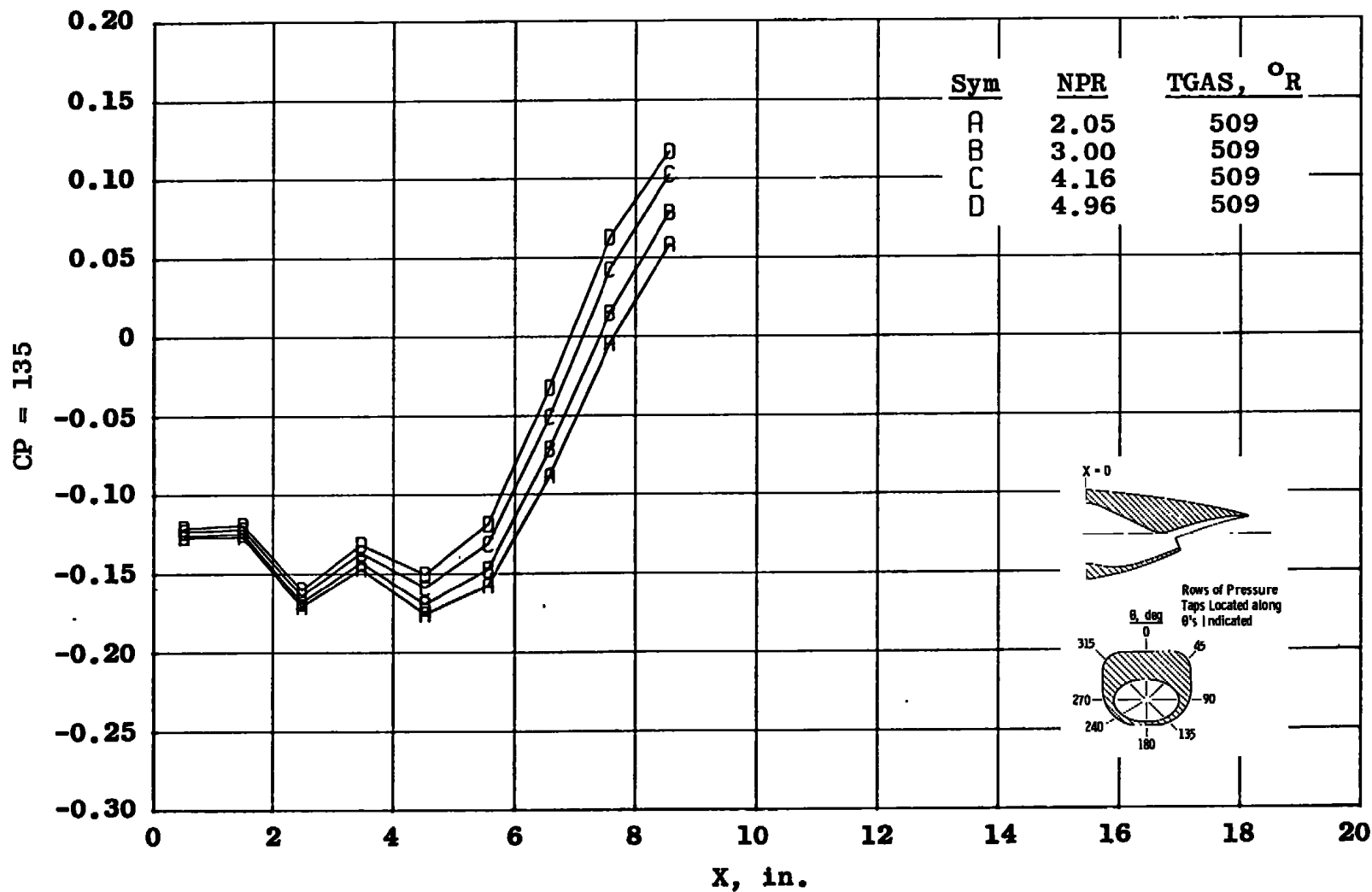
a. $\theta = 0$
 Figure 6. Nozzle afterbody pressure distribution at Mach number 0.85.



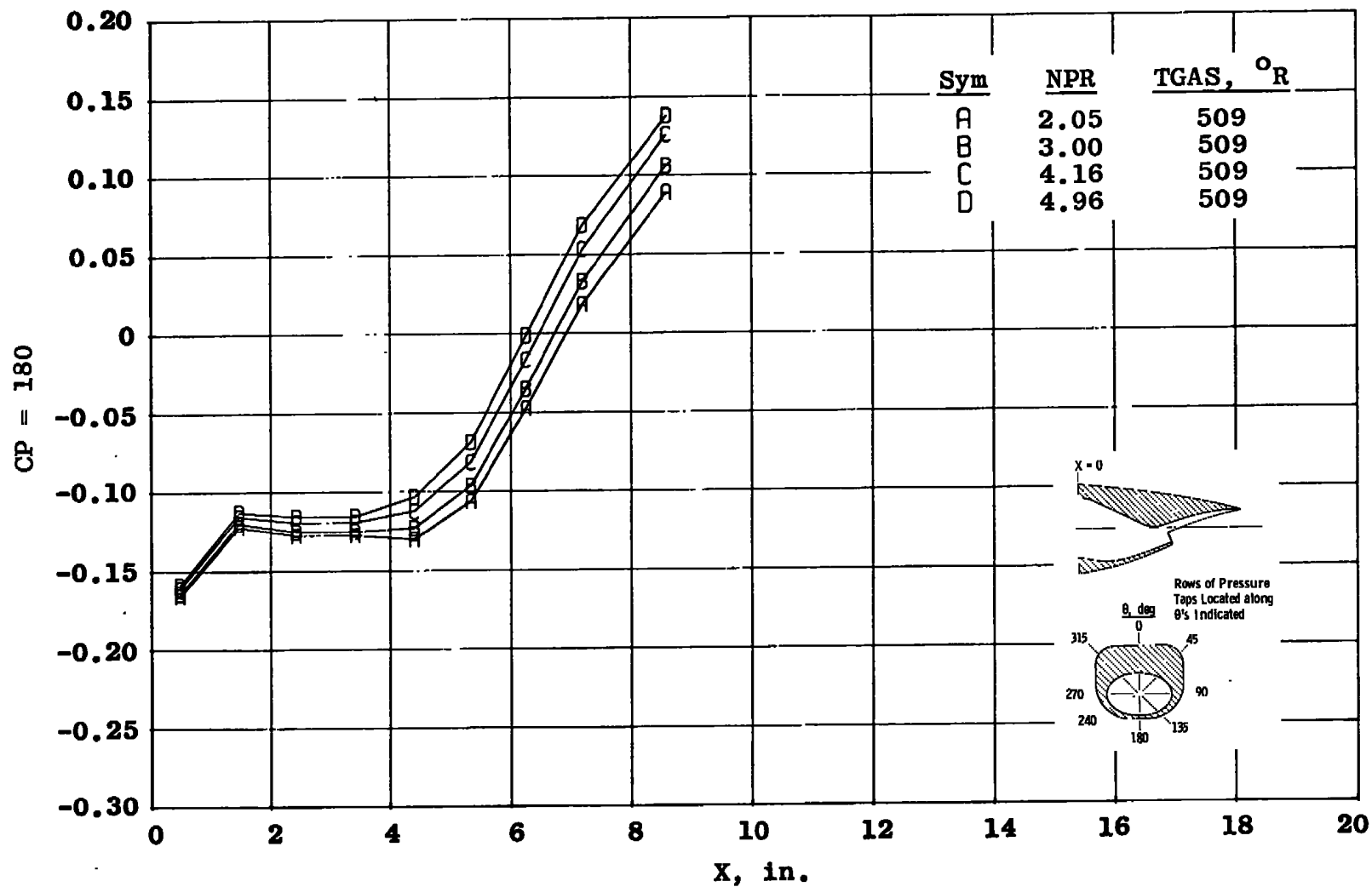
b. $\theta = 45$ deg
Figure 6. Continued.



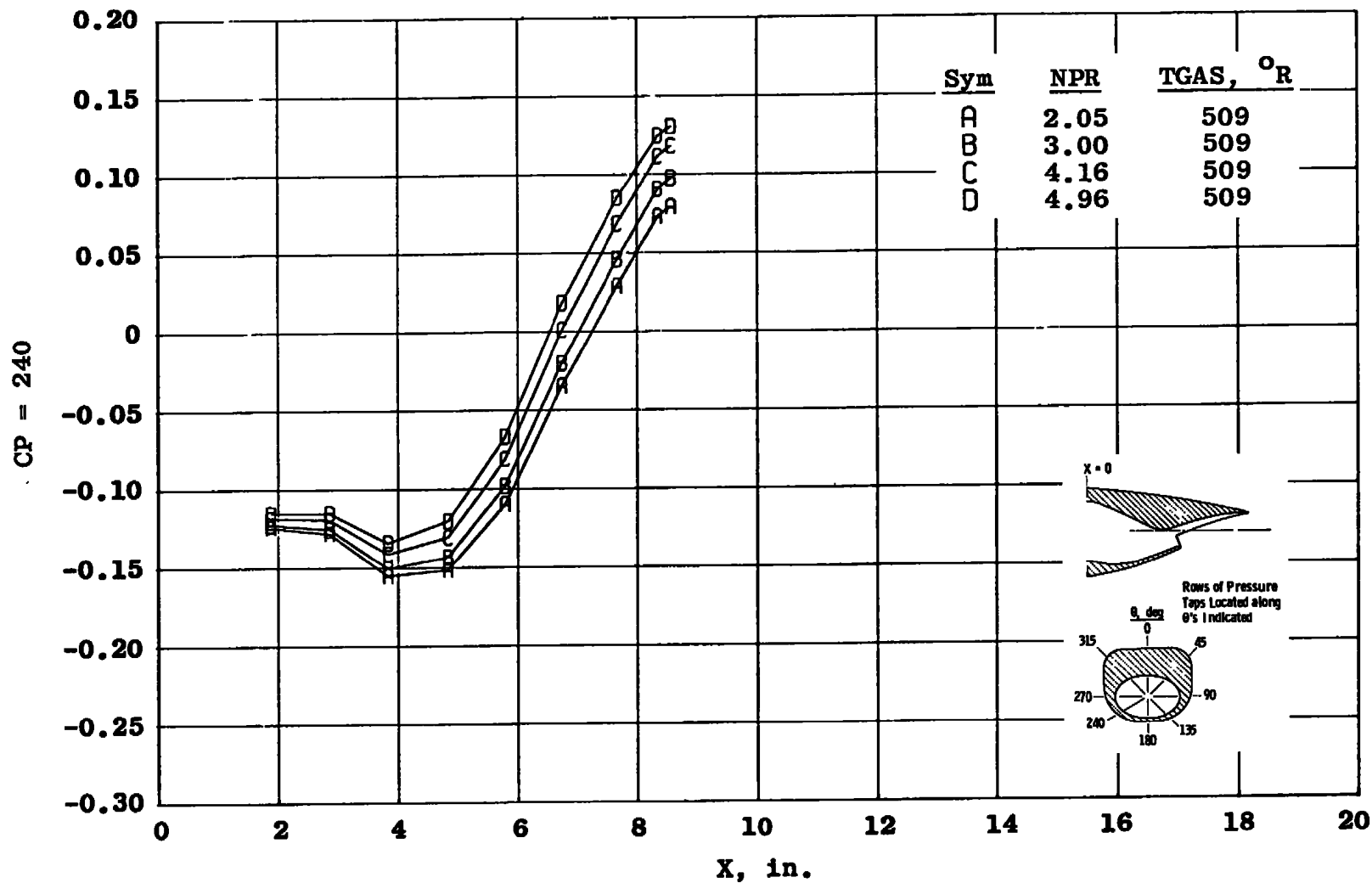
c. $\theta = 90$ deg
Figure 6. Continued.



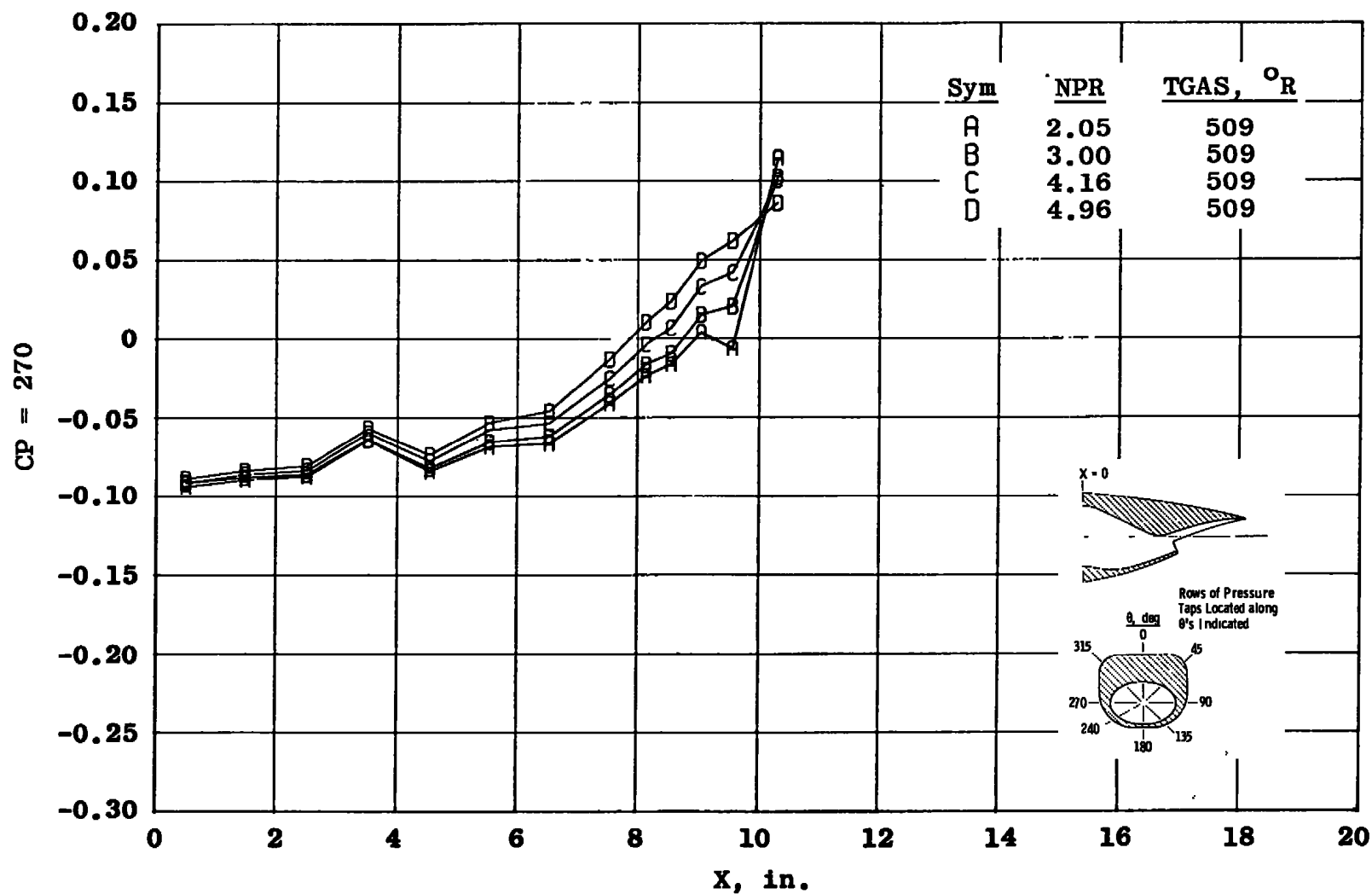
d. $\theta = 135$ deg
Figure 6. Continued.



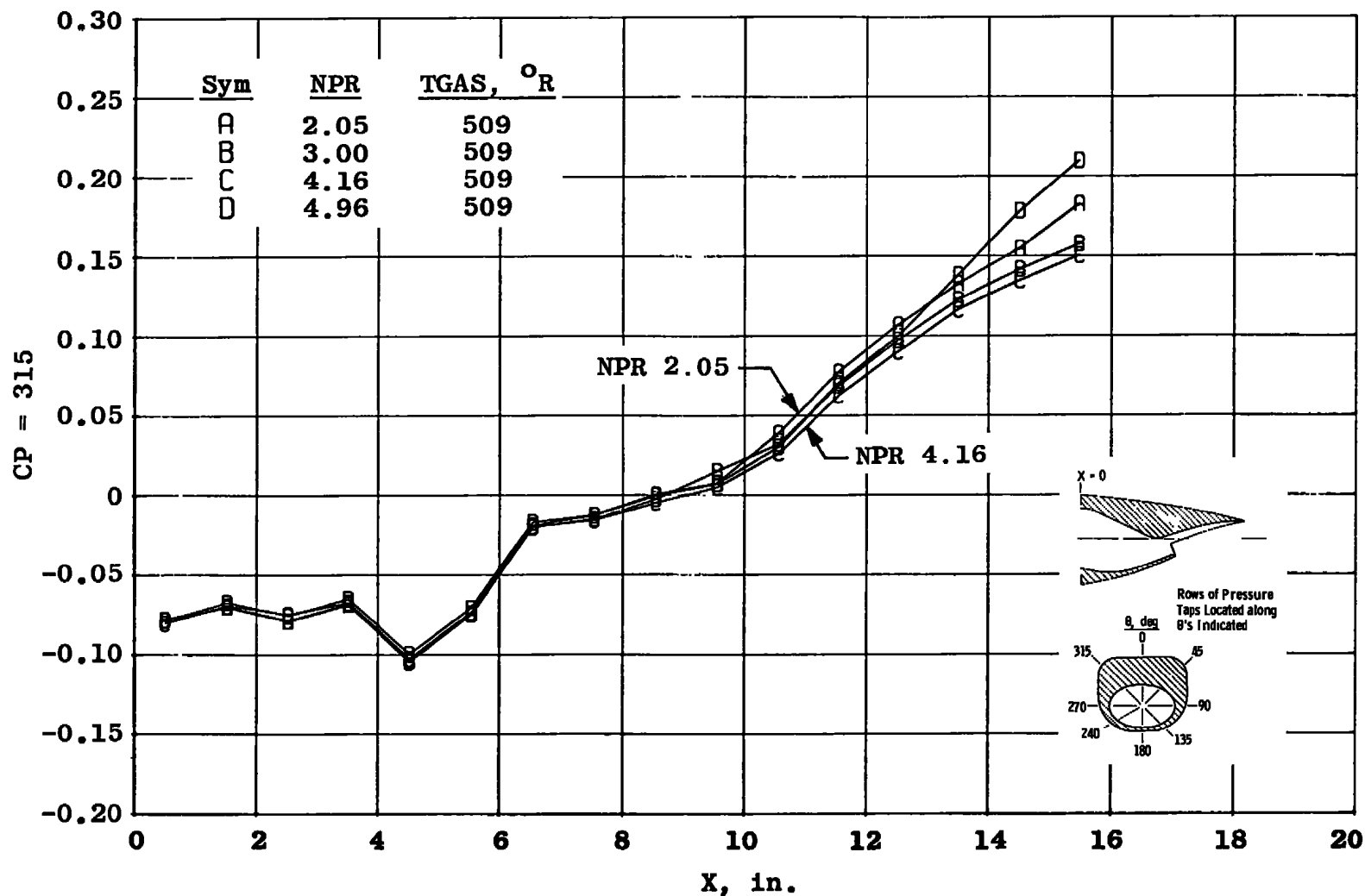
e. $\theta = 180$ deg
Figure 6. Continued.



f. $\theta = 240$ deg
Figure 6. Continued.



g. $\theta = 270$ deg
Figure 6. Continued.



h. $\theta = 315$ deg
Figure 6. Concluded.

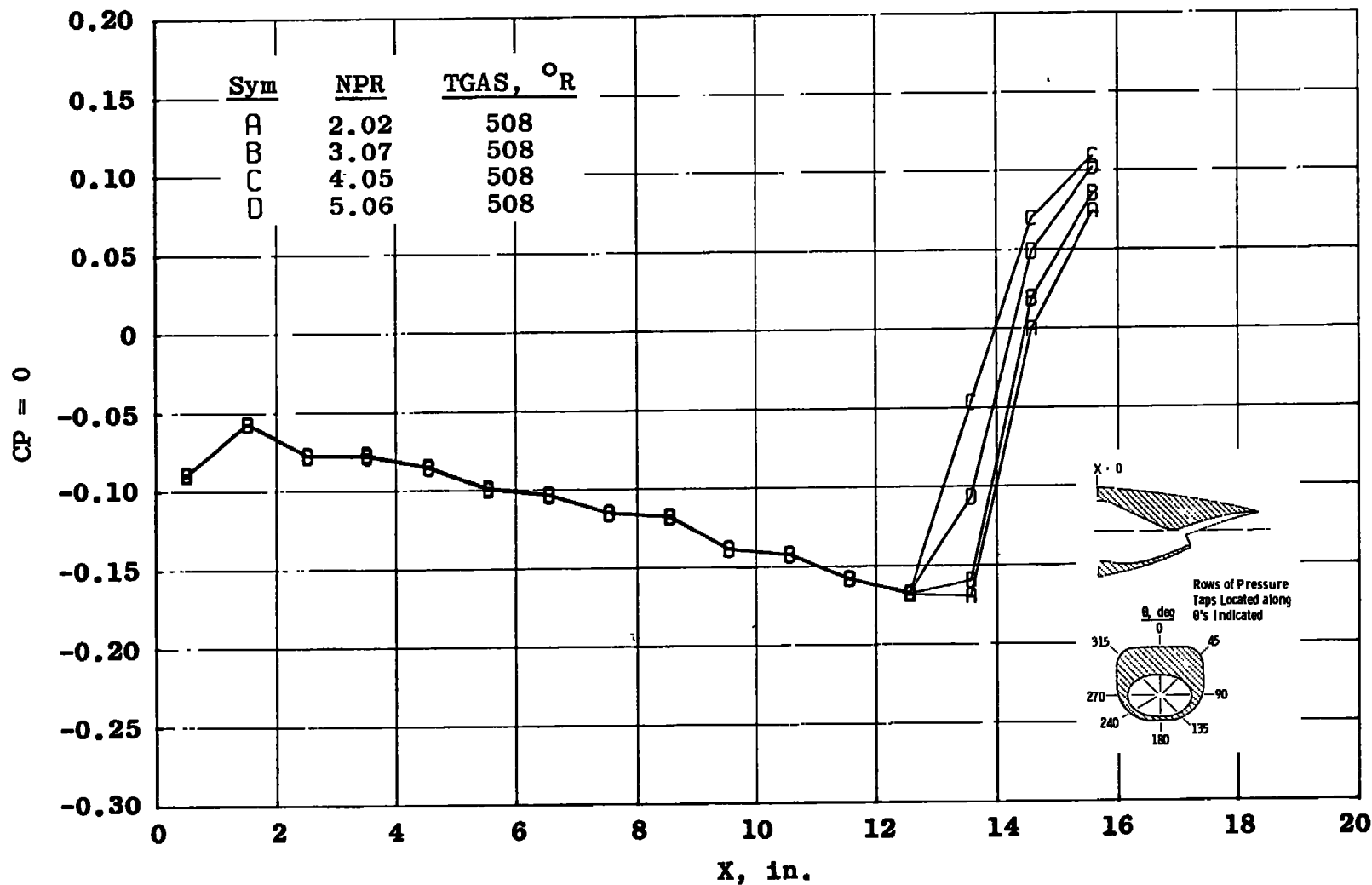
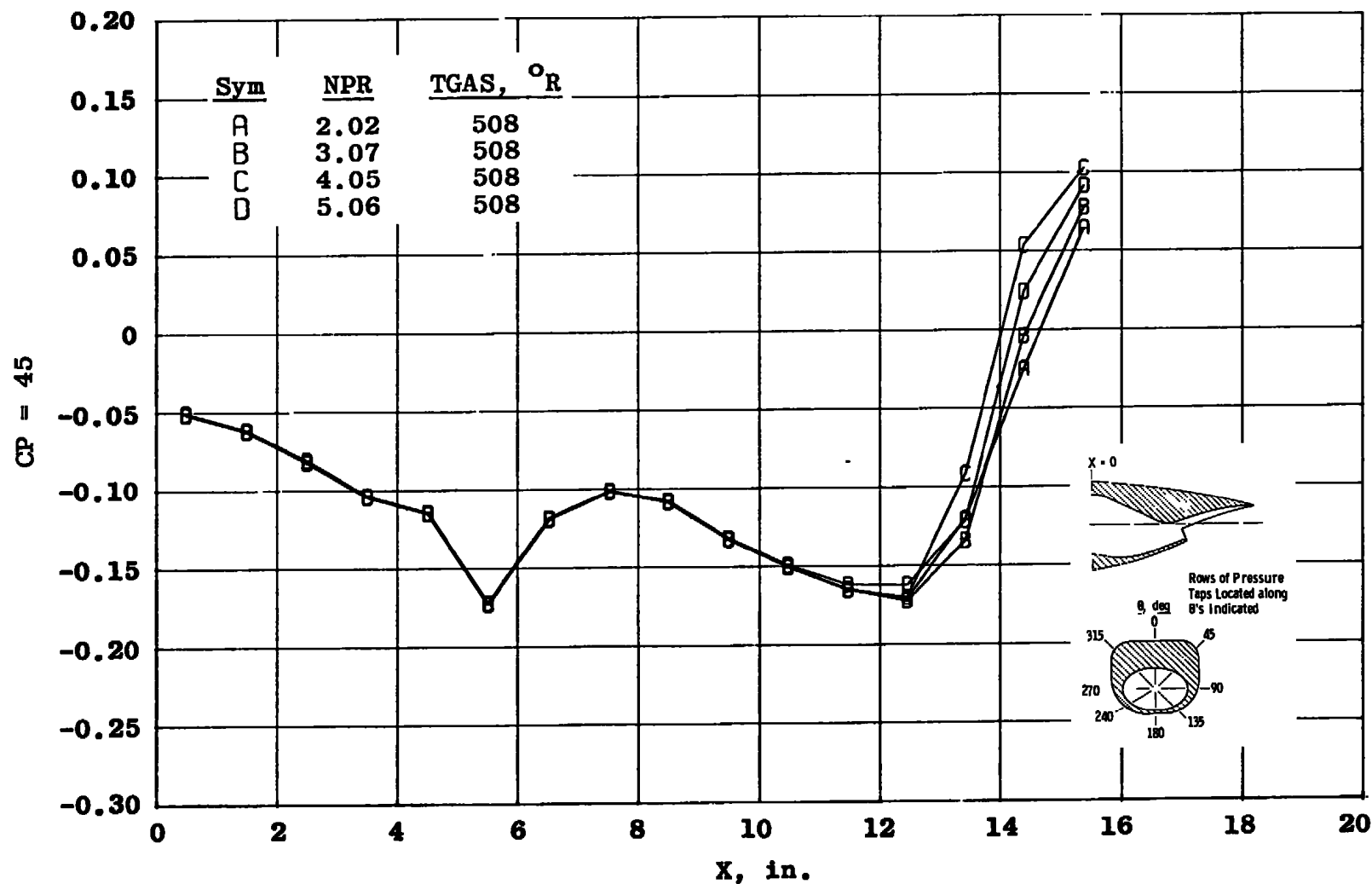
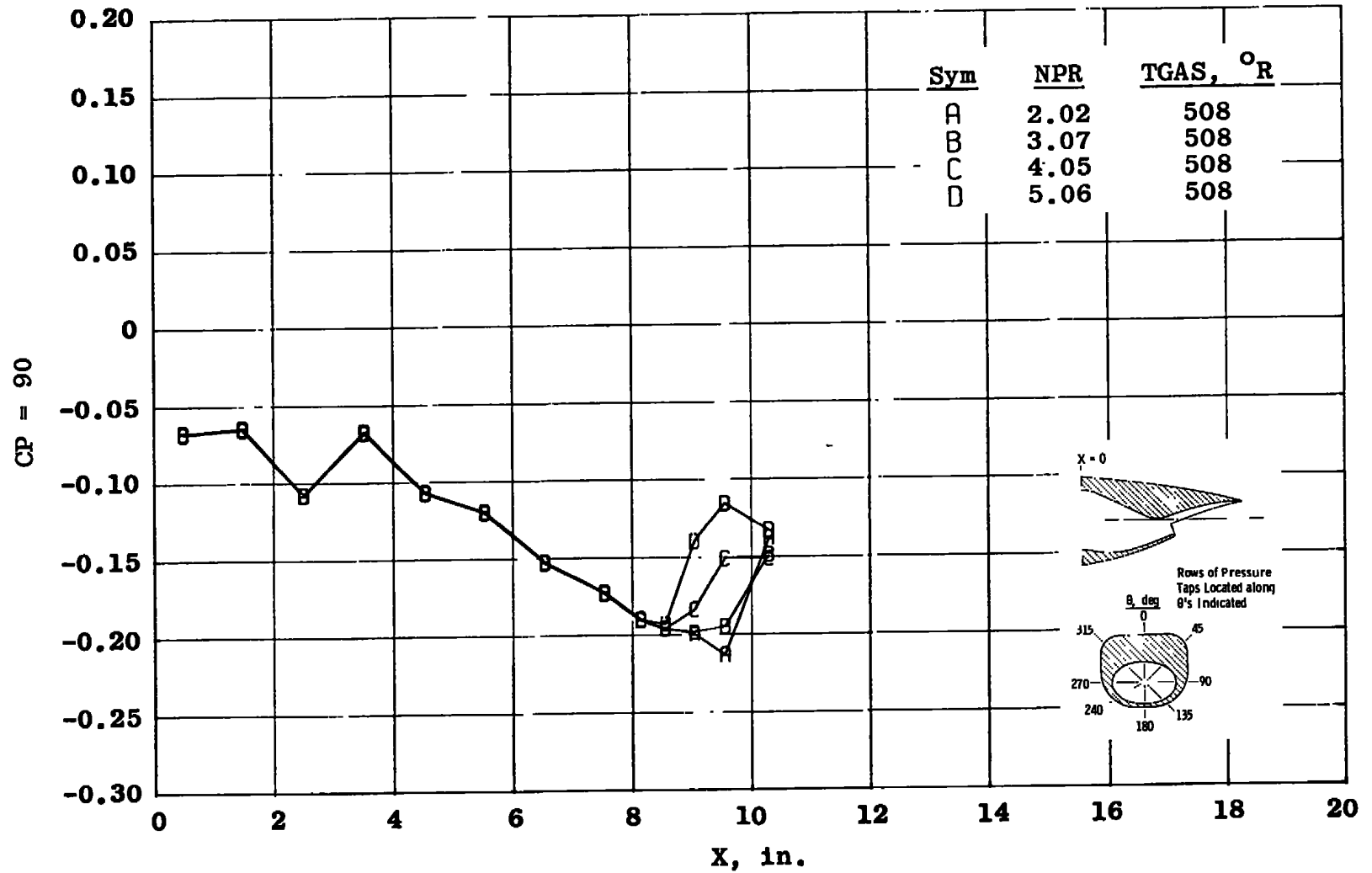
a. $\theta = 0$

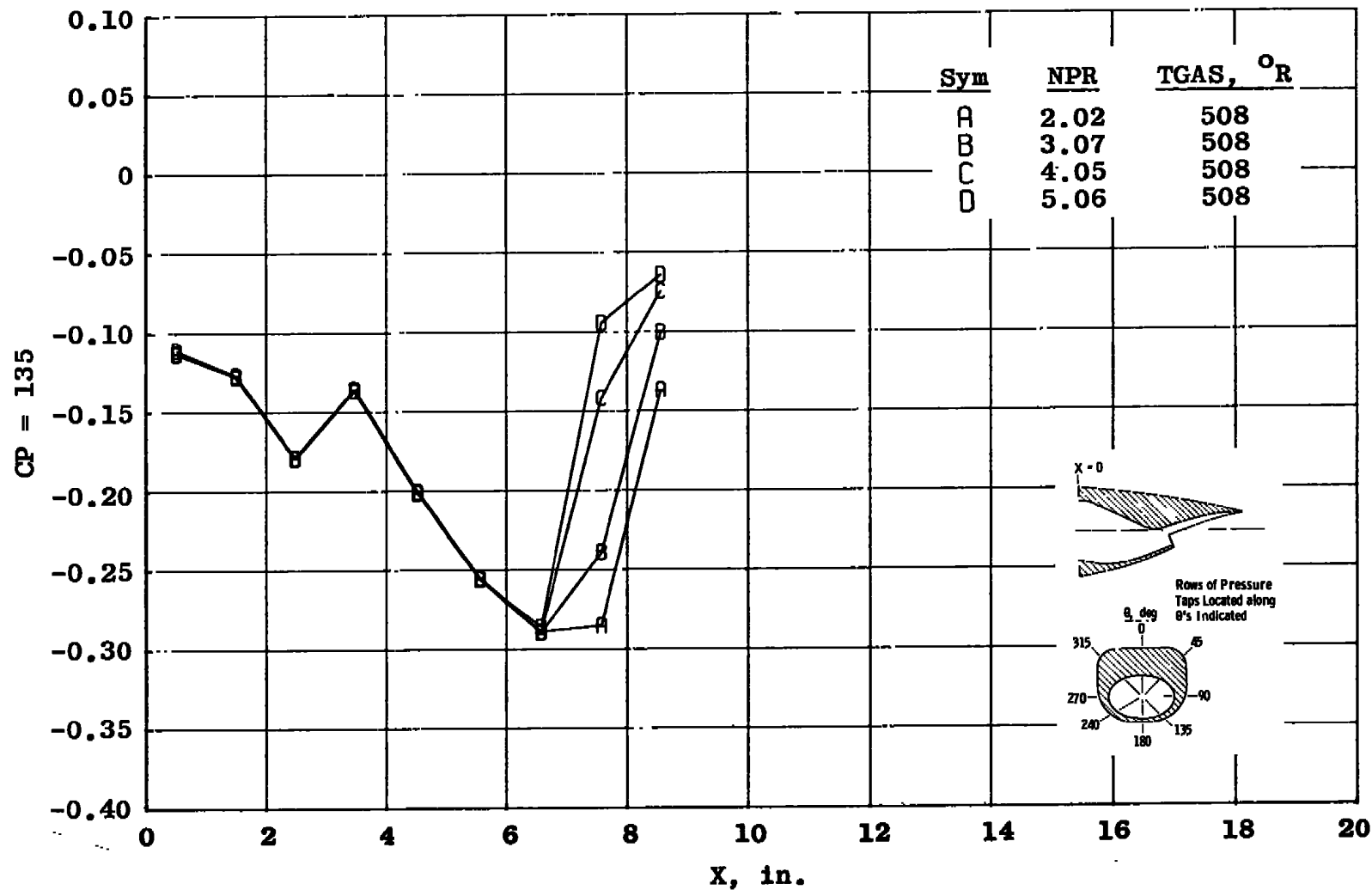
Figure 7. Nozzle afterbody pressure distribution at Mach number 1.4.



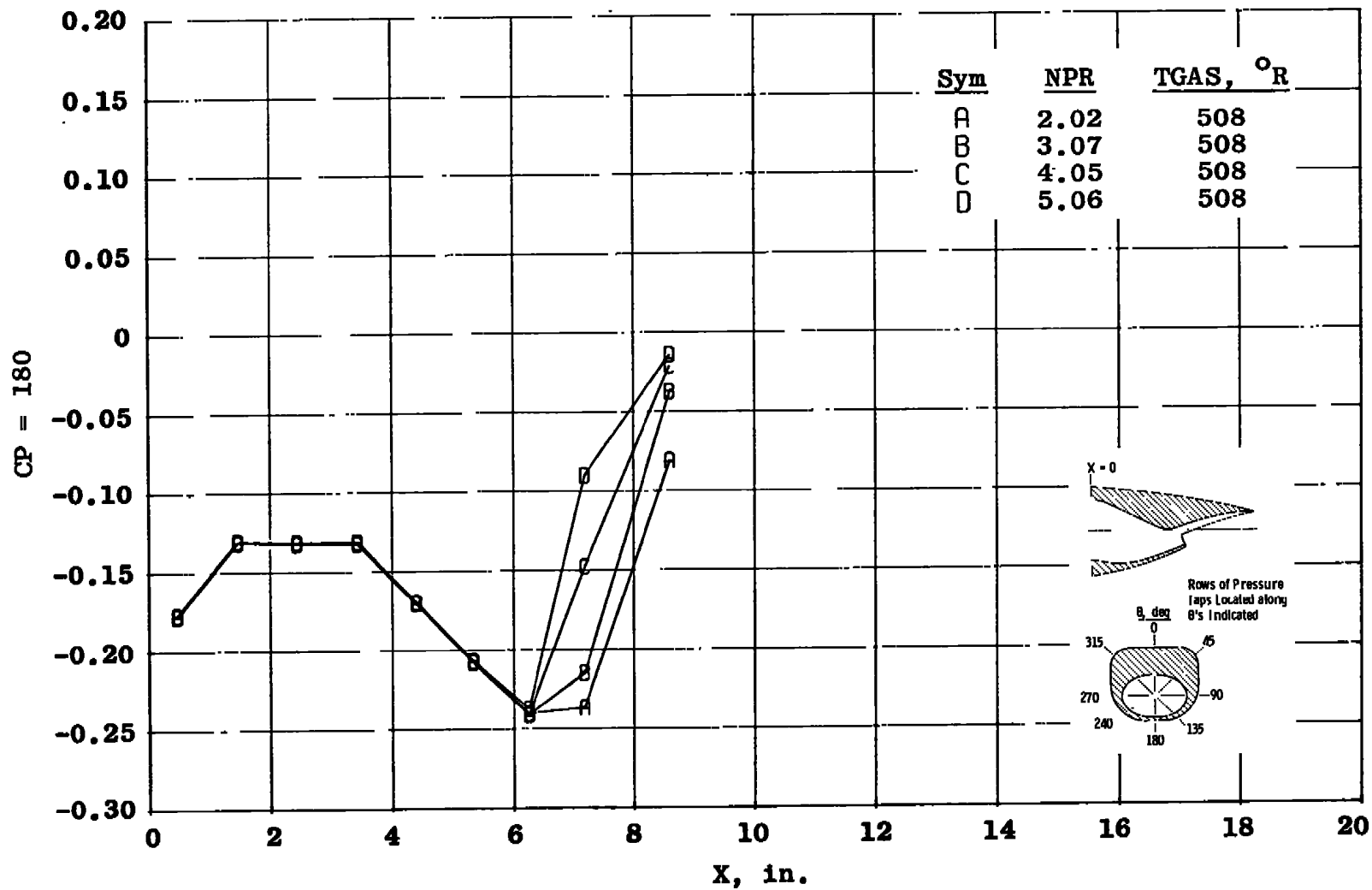
b. $\theta = 45$ deg
Figure 7. Continued.



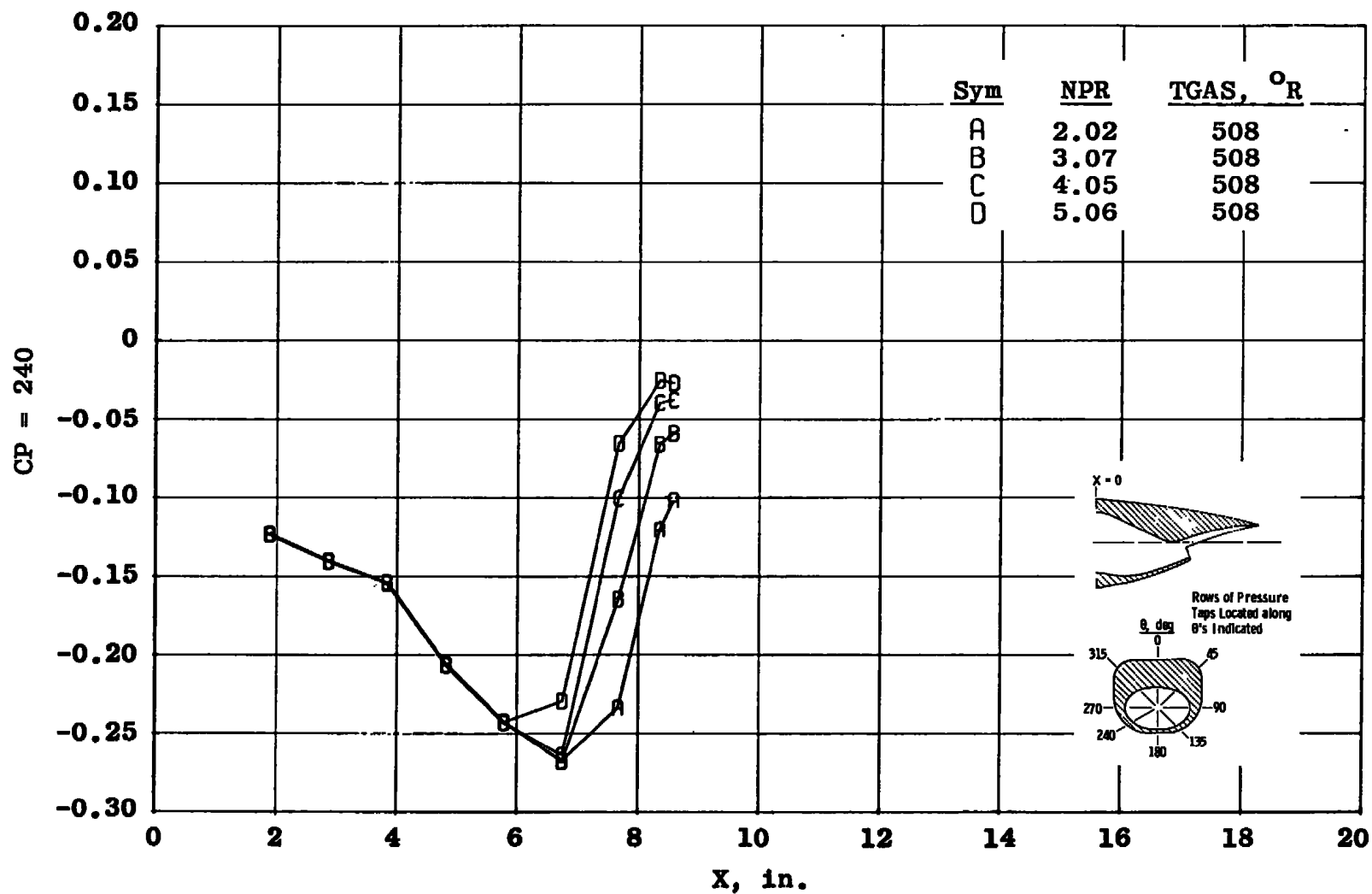
c. $\theta = 90$ deg
Figure 7. Continued.



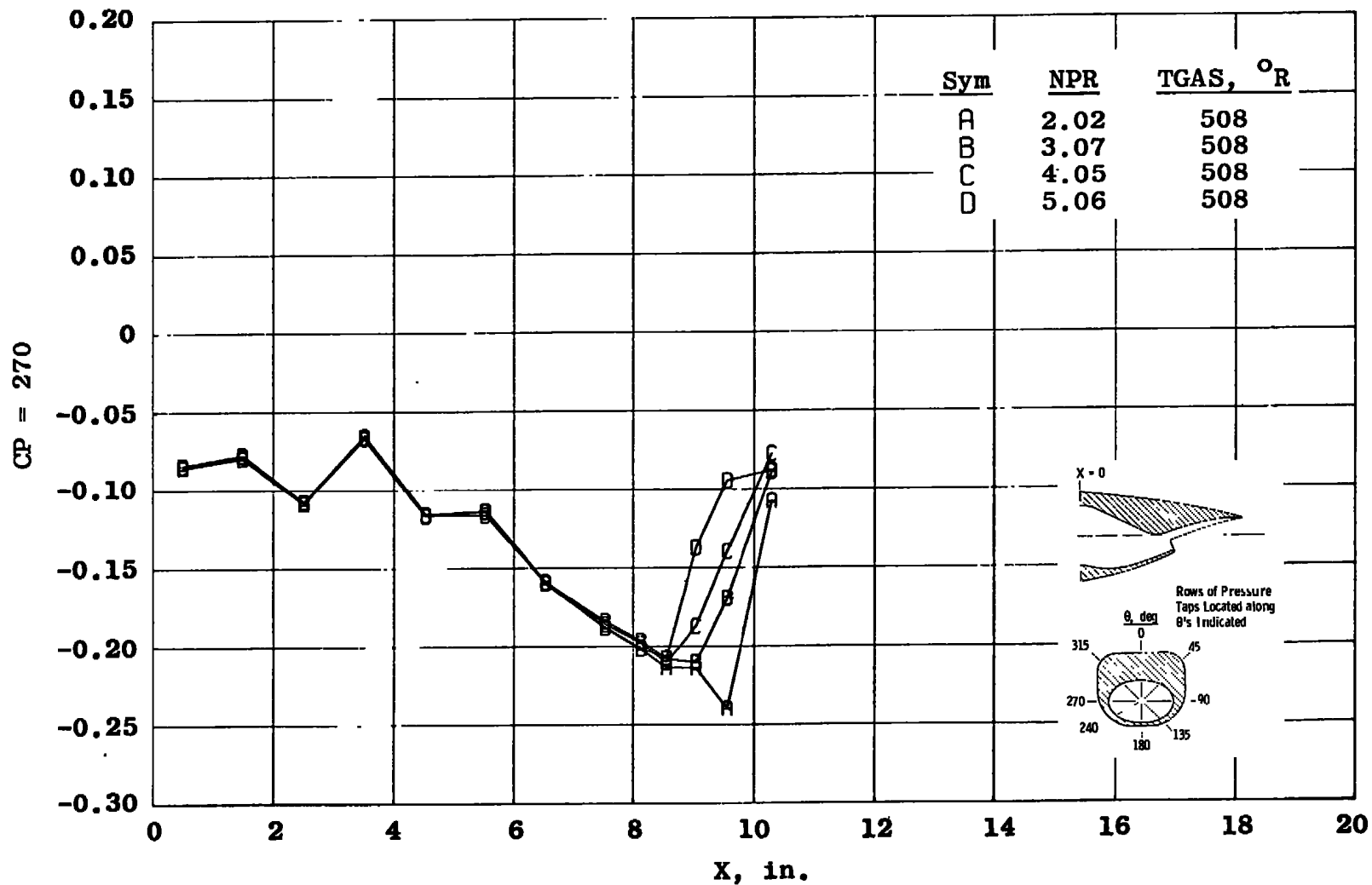
d. $\theta = 135$ deg
Figure 7. Continued.



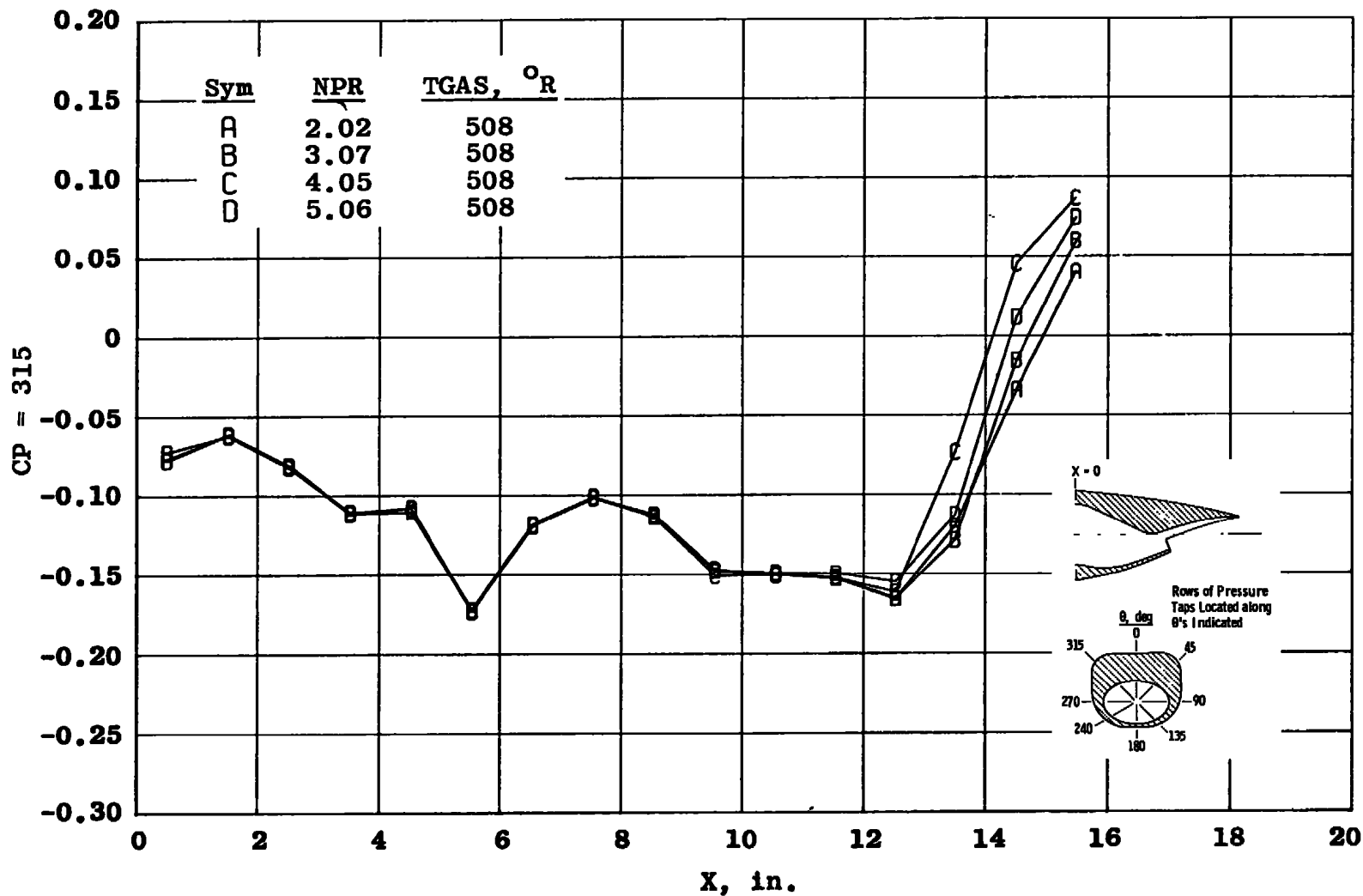
e. $\theta = 180$ deg
Figure 7. Continued.



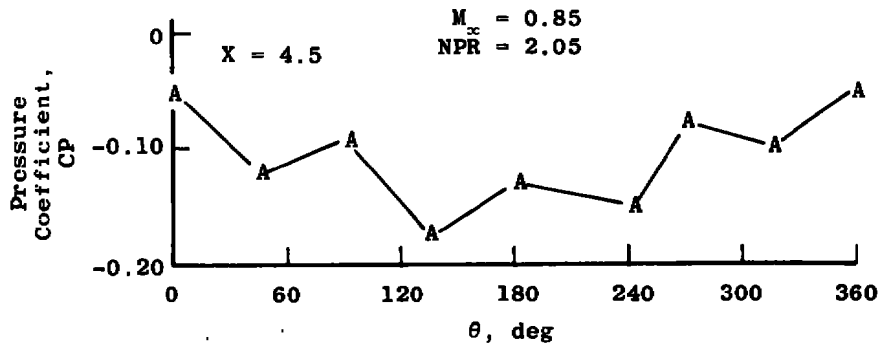
f. $\theta = 240$ deg
Figure 7. Continued.



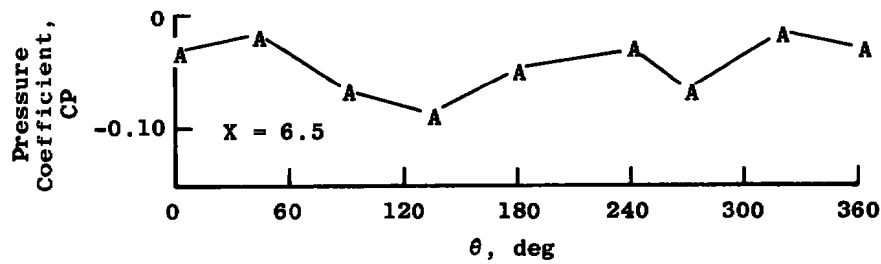
g. $\theta = 270$ deg
Figure 7. Continued.



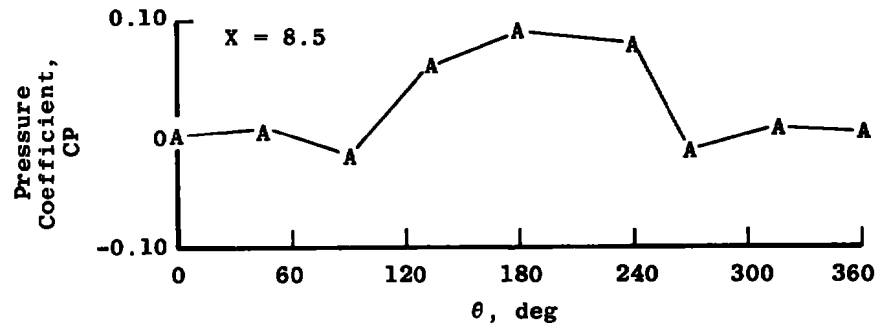
h. $\theta = 315$ deg
Figure 7. Concluded.



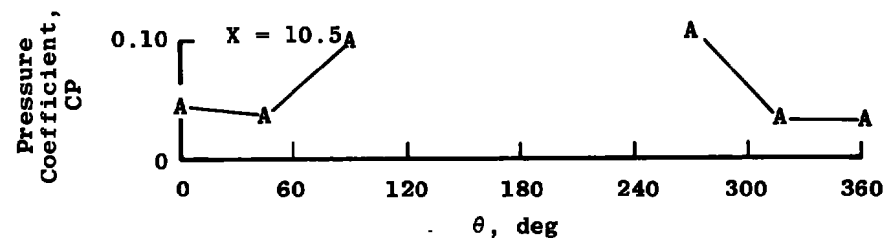
a. $X = 4.5$ in.



b. $X = 6.5$ in.



c. $X = 8.5$ in.



d. $X = 10.5$ in.

Figure 8. Circumferential pressure distribution.

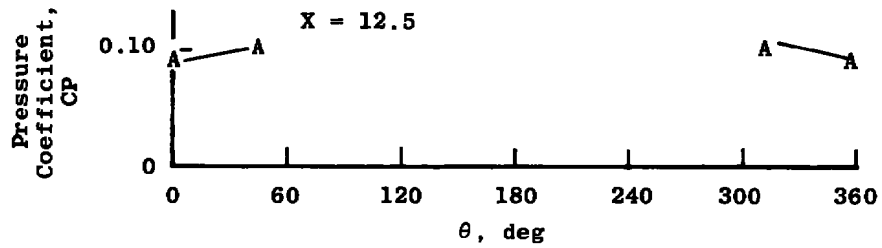
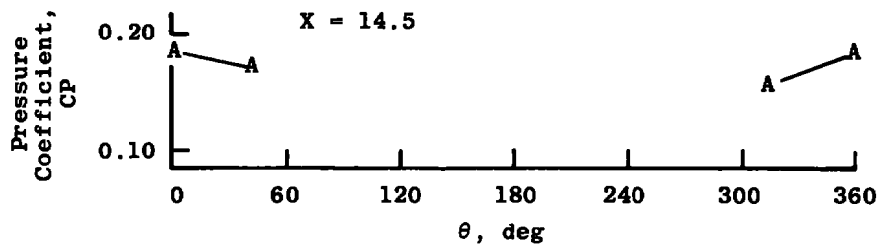
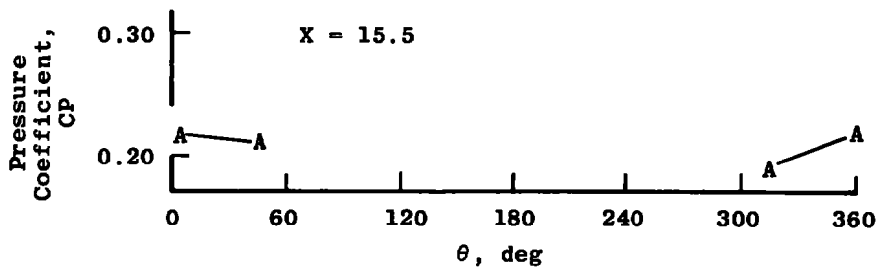
e. $X = 12.5$ in.f. $X = 14.5$ in.g. $X = 15.5$ in.

Figure 8. Concluded.

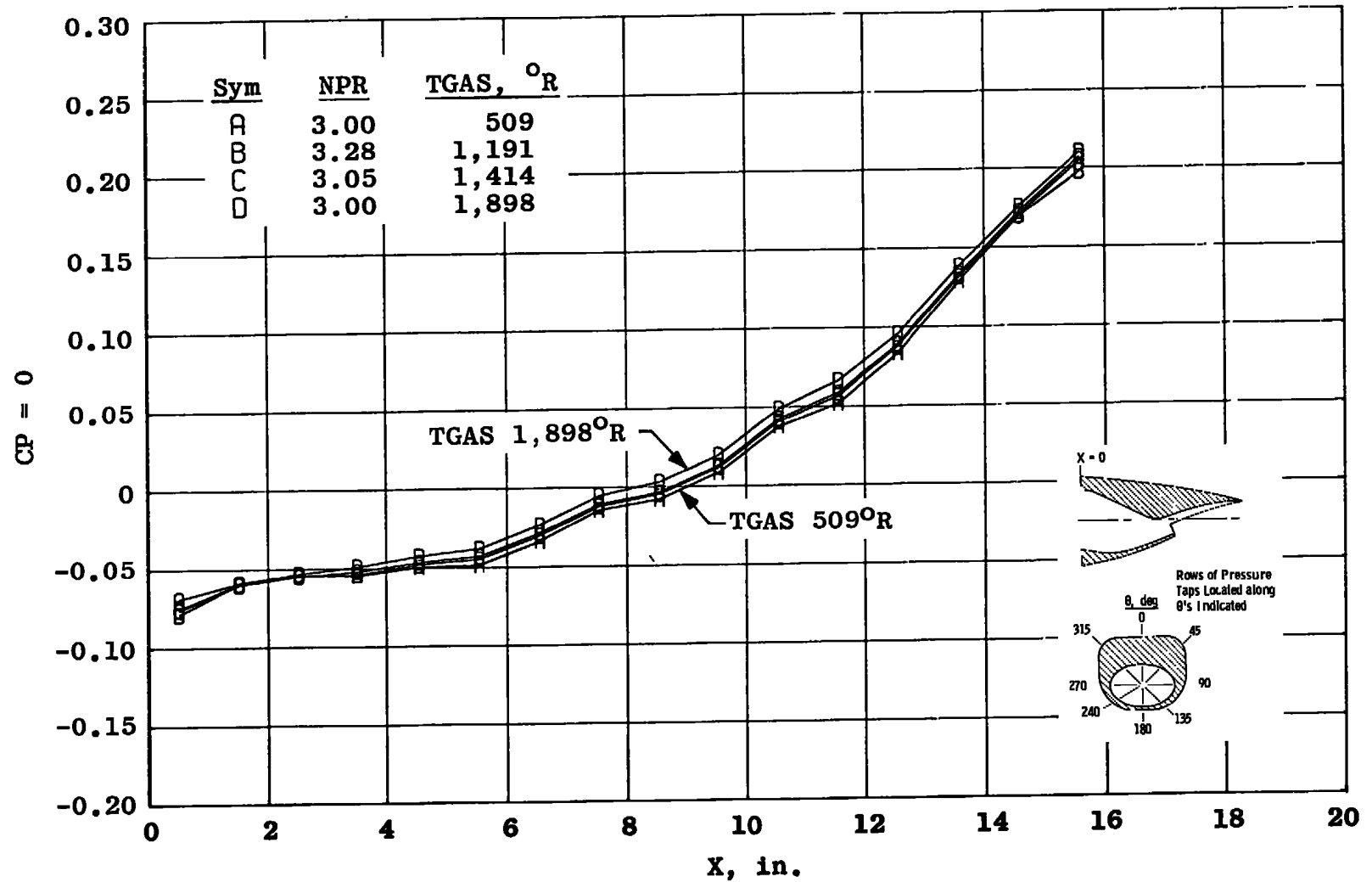
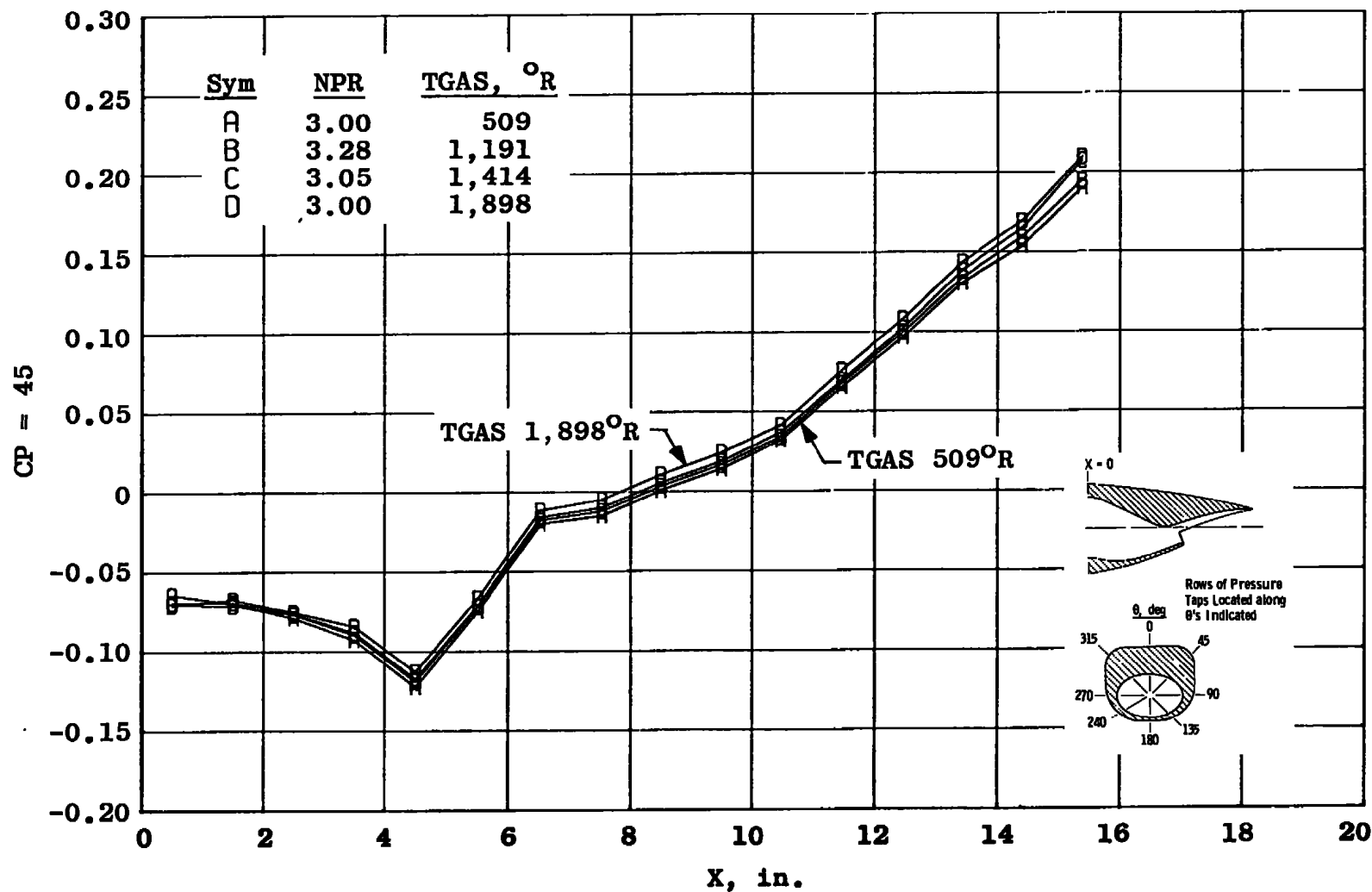
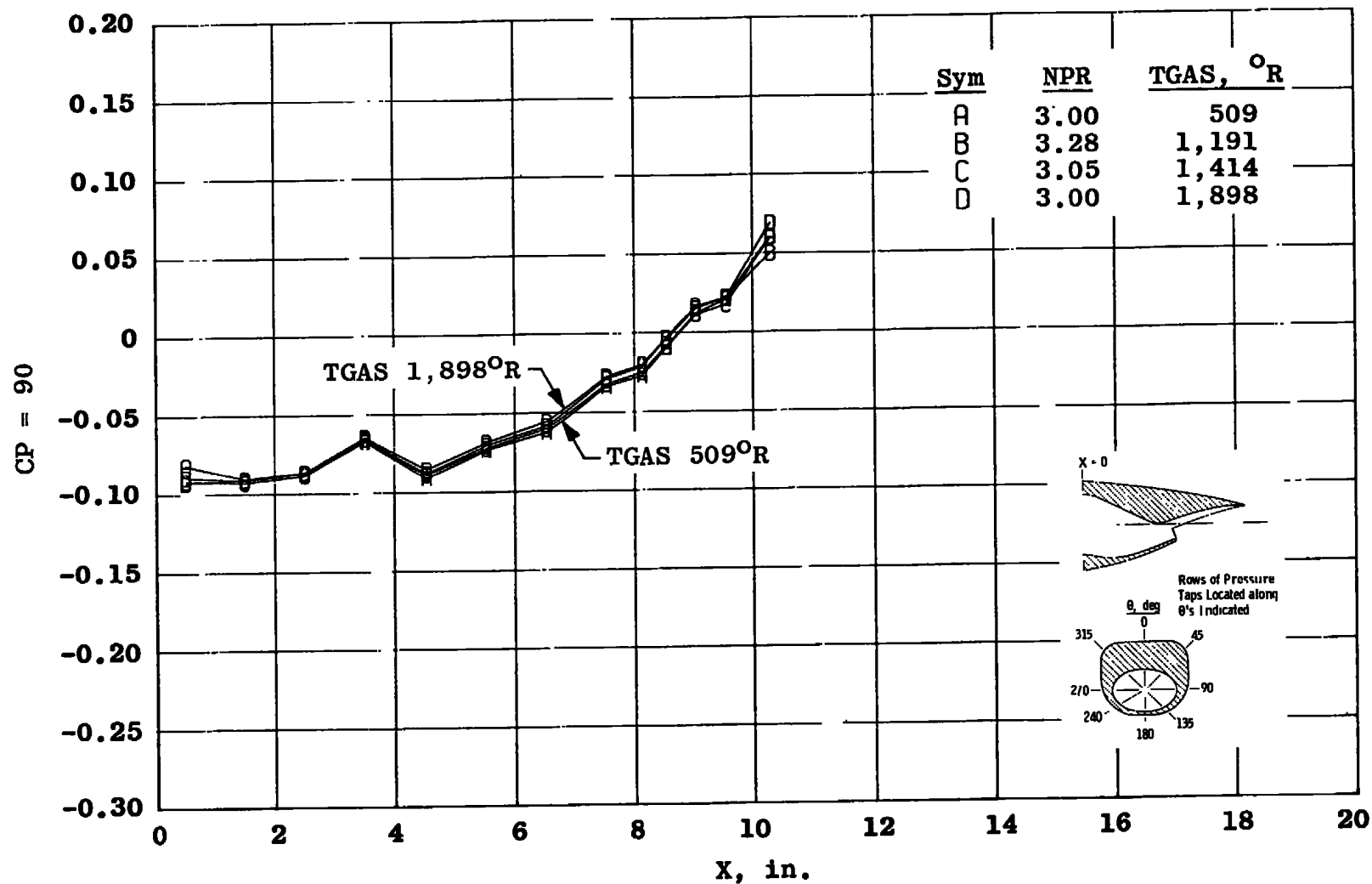
a. $\theta = 0$

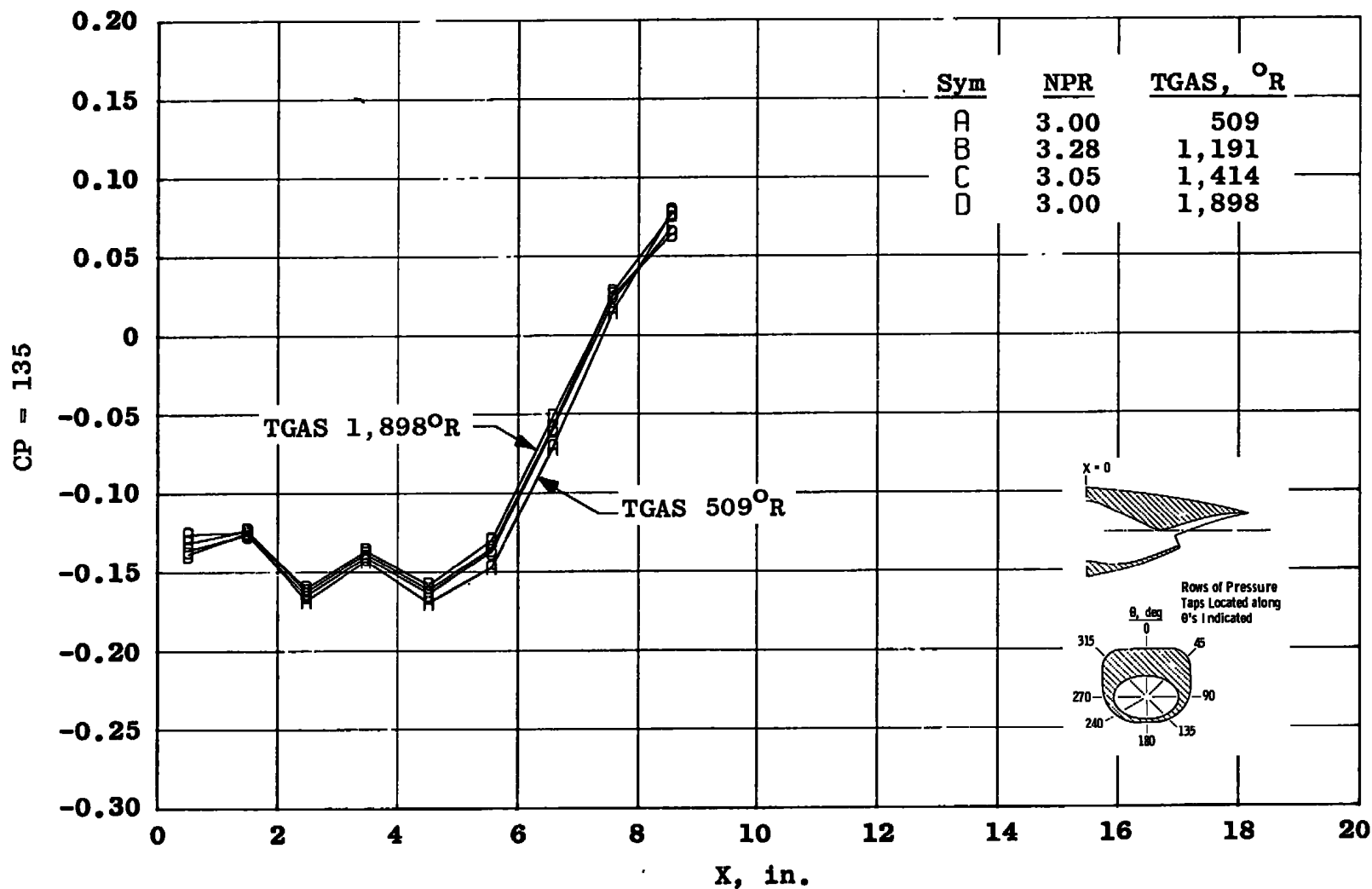
Figure 9. Nozzle afterbody pressure distribution at four exhaust plume temperatures, $M_\infty = 0.85$.



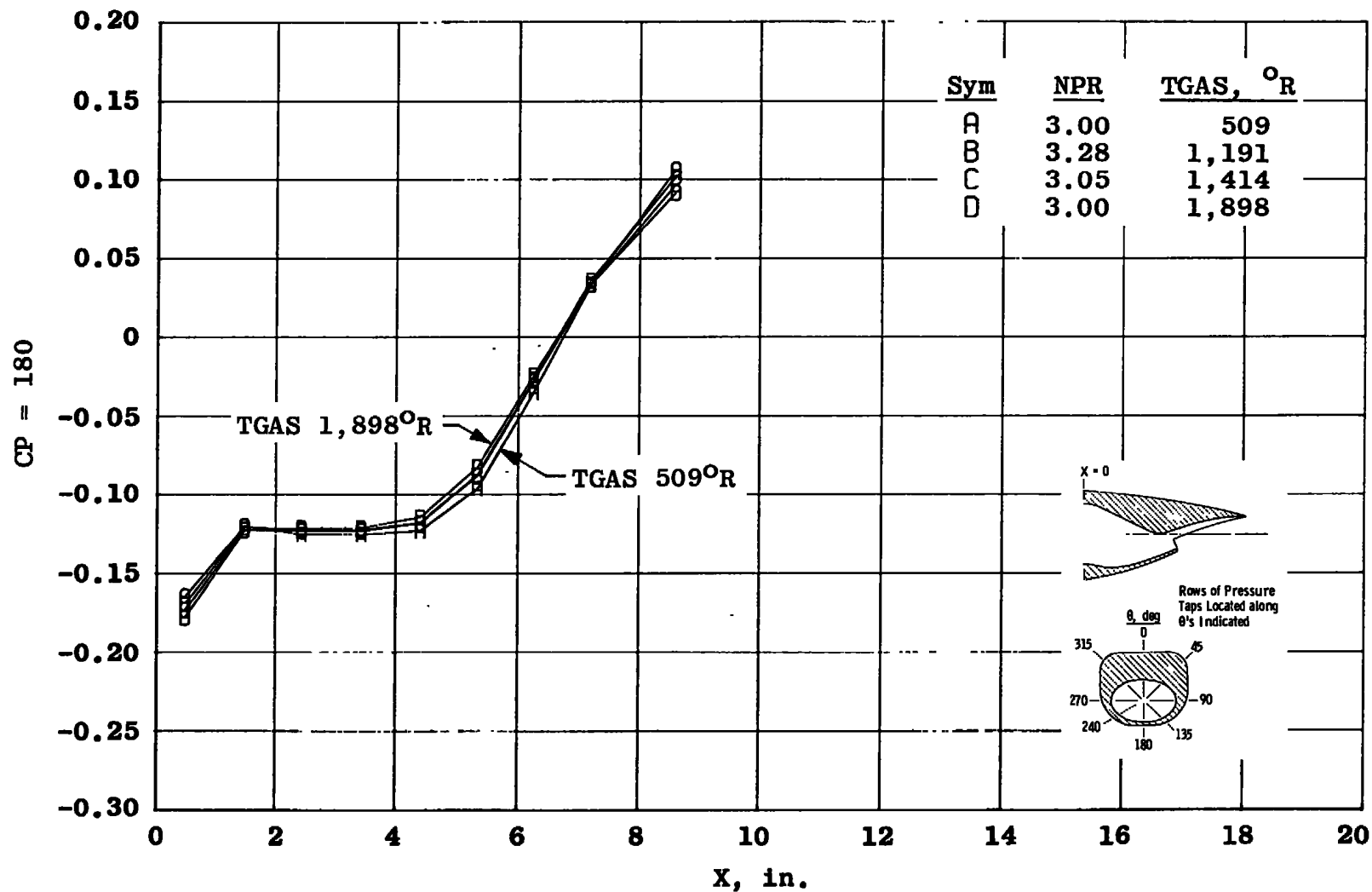
b. $\theta = 45$ deg
Figure 9. Continued.



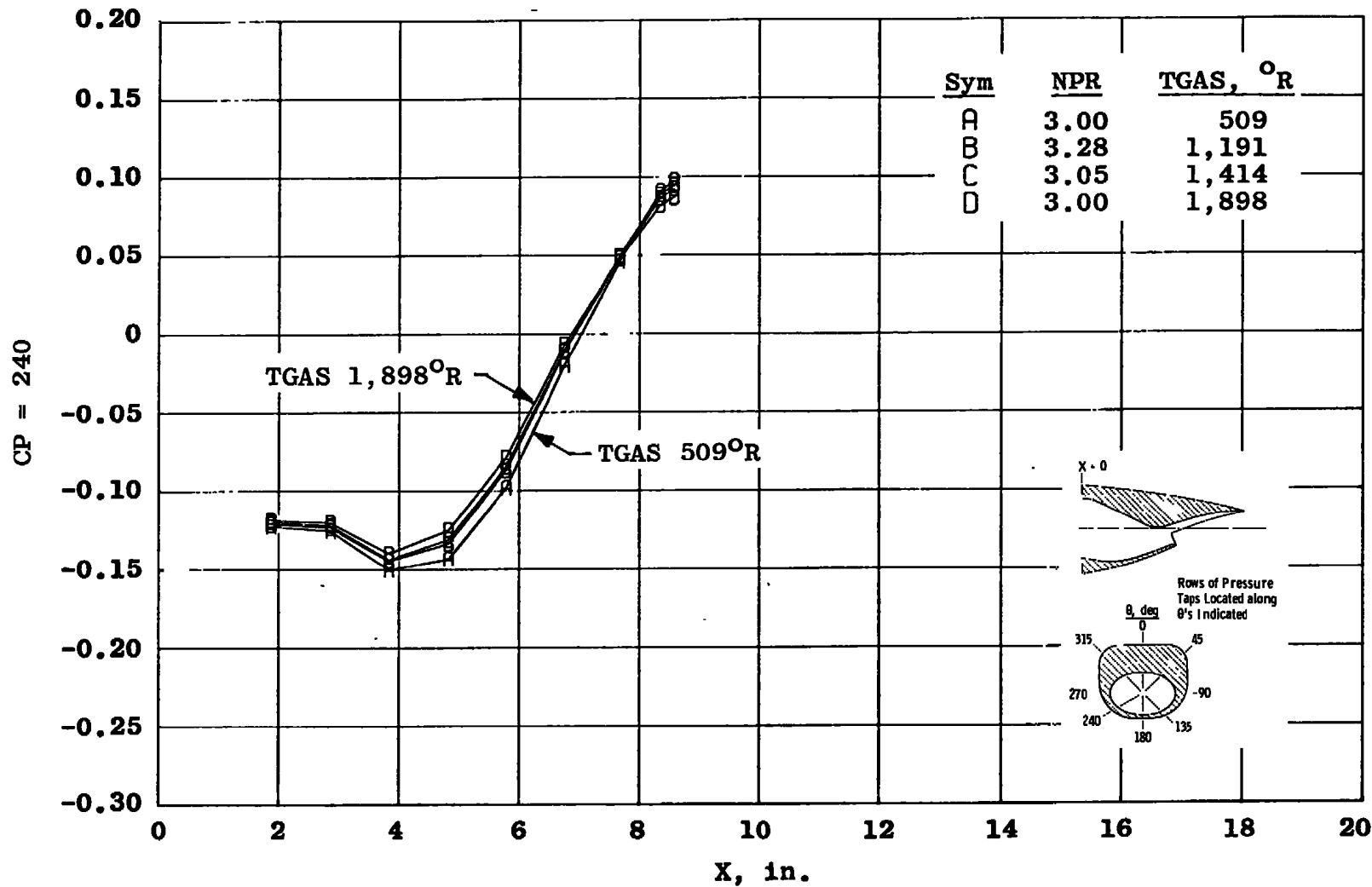
c. $\theta = 90$ deg
Figure 9. Continued.



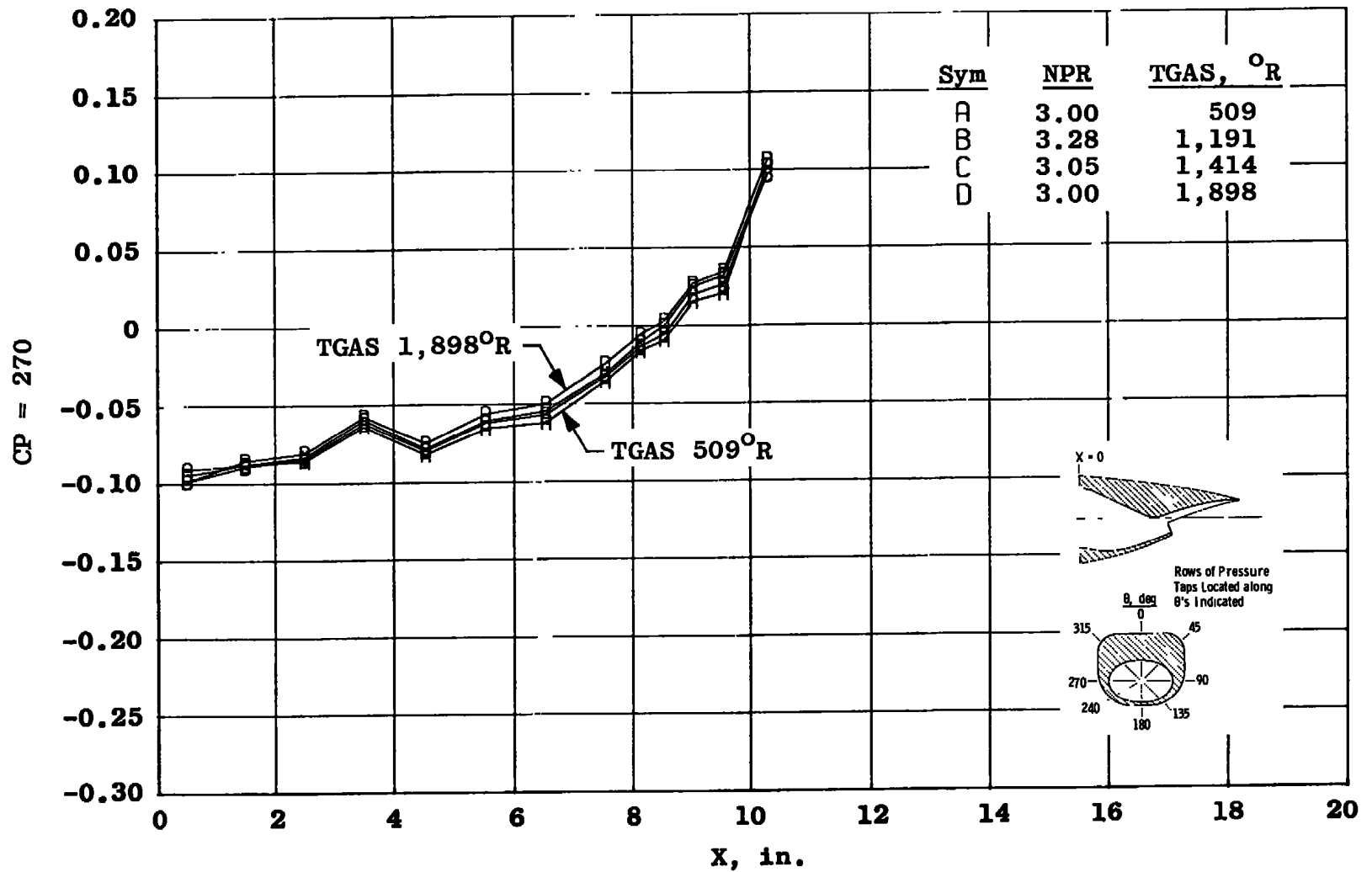
d. $\theta = 135$ deg
Figure 9. Continued.



e. $\theta = 180$ deg
Figure 9. Continued.



f. $\theta = 240$ deg
Figure 9. Continued.



g. $\theta = 270$ deg
Figure 9. Continued.

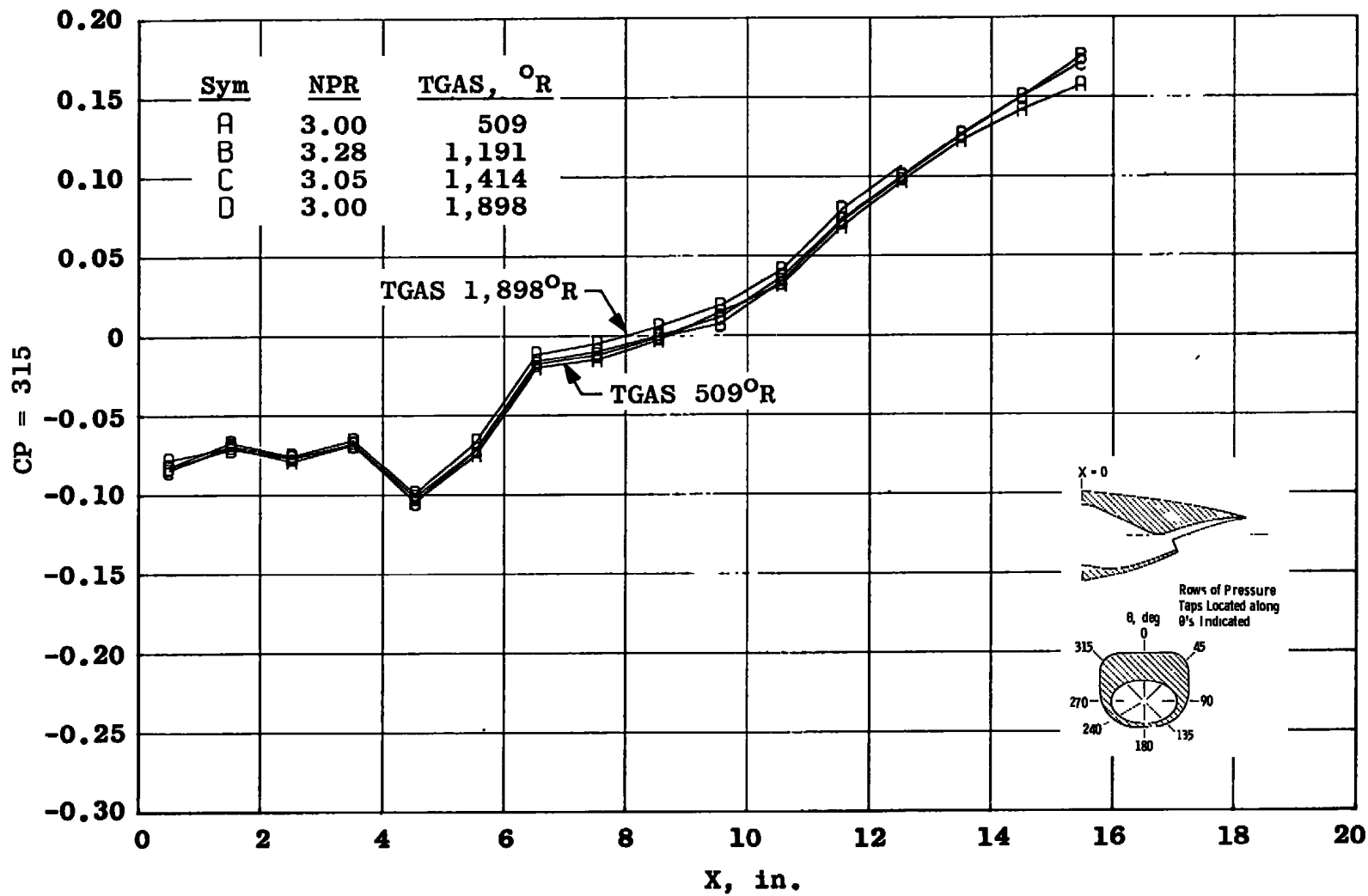
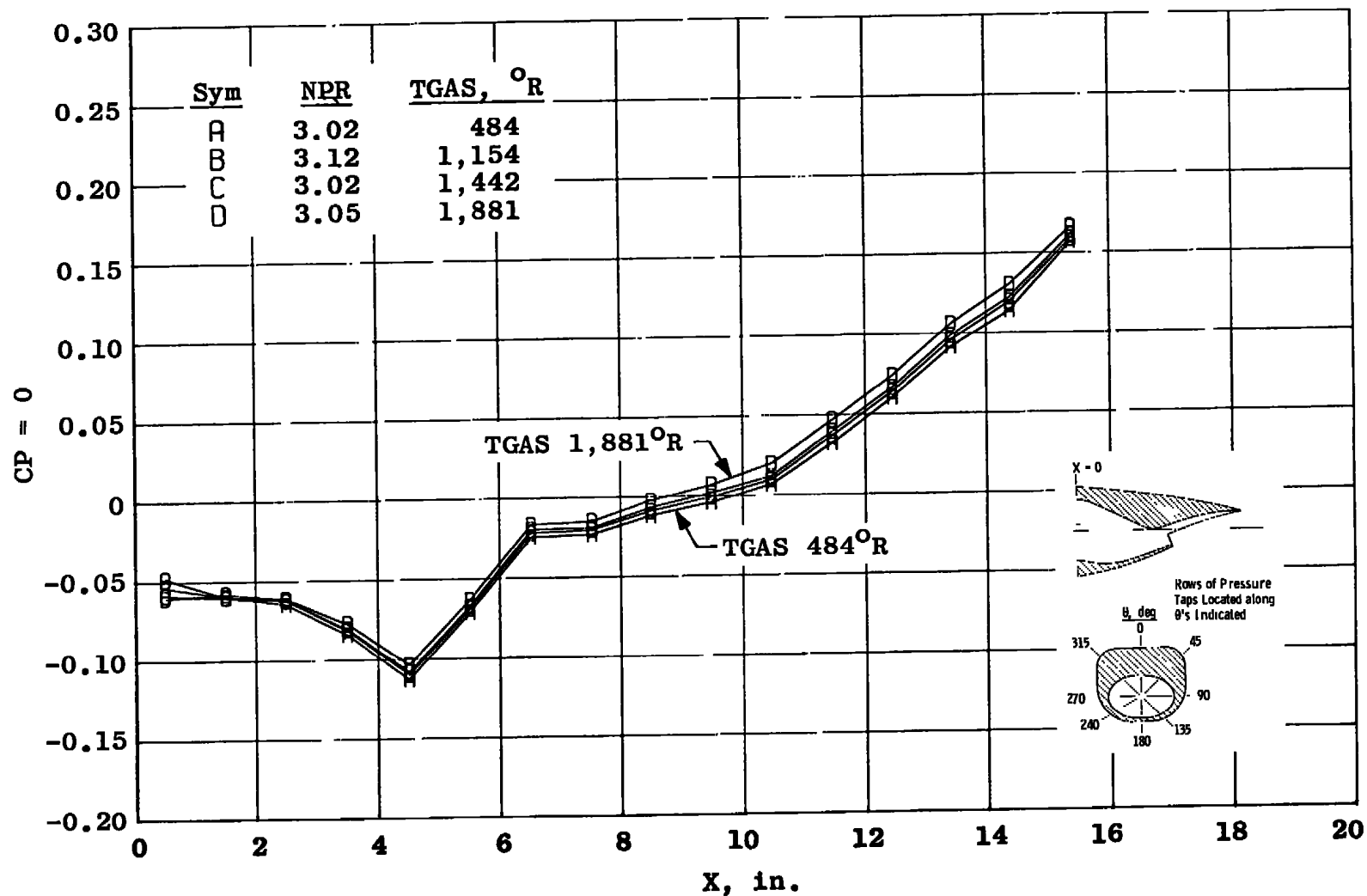
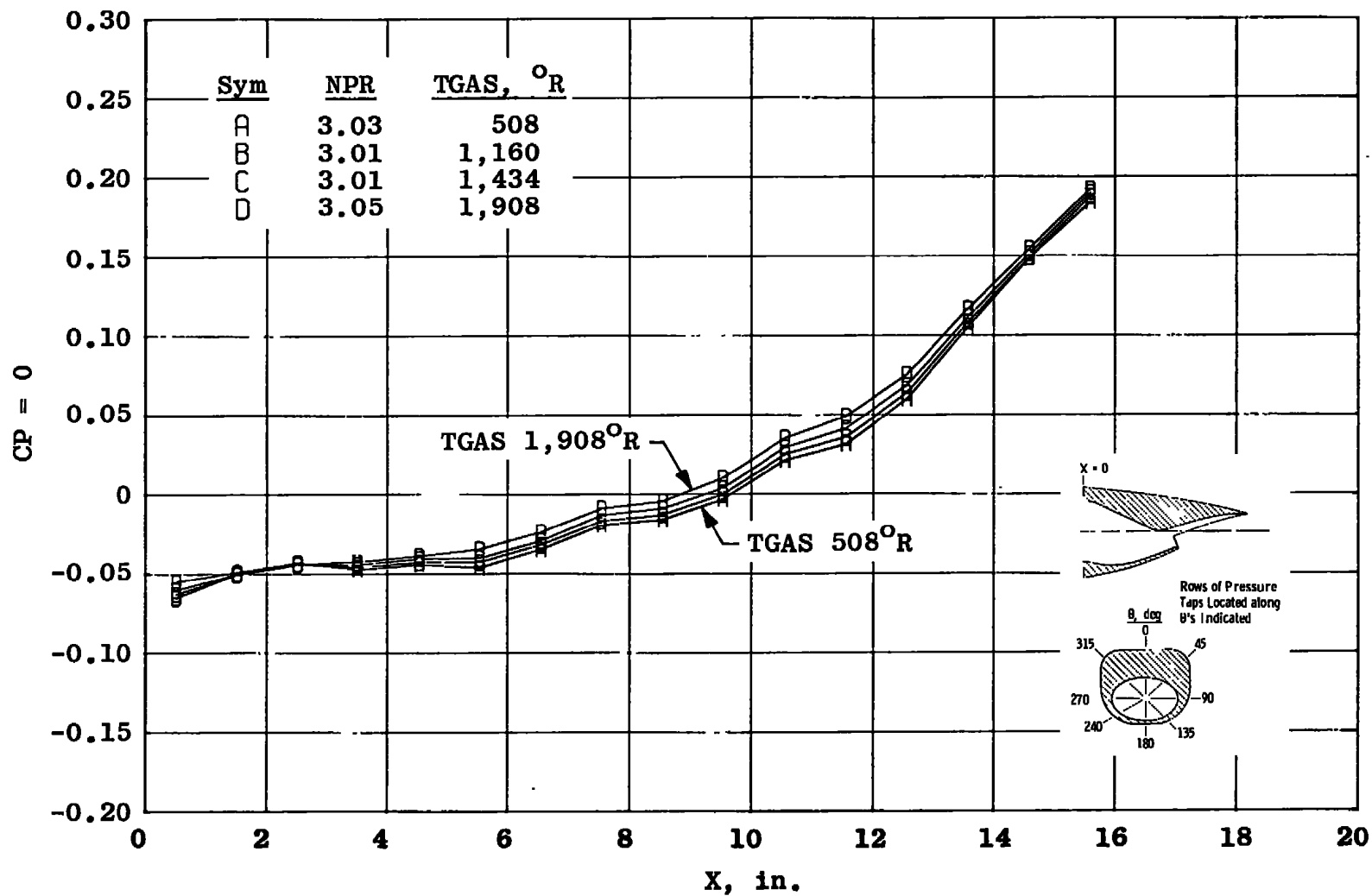
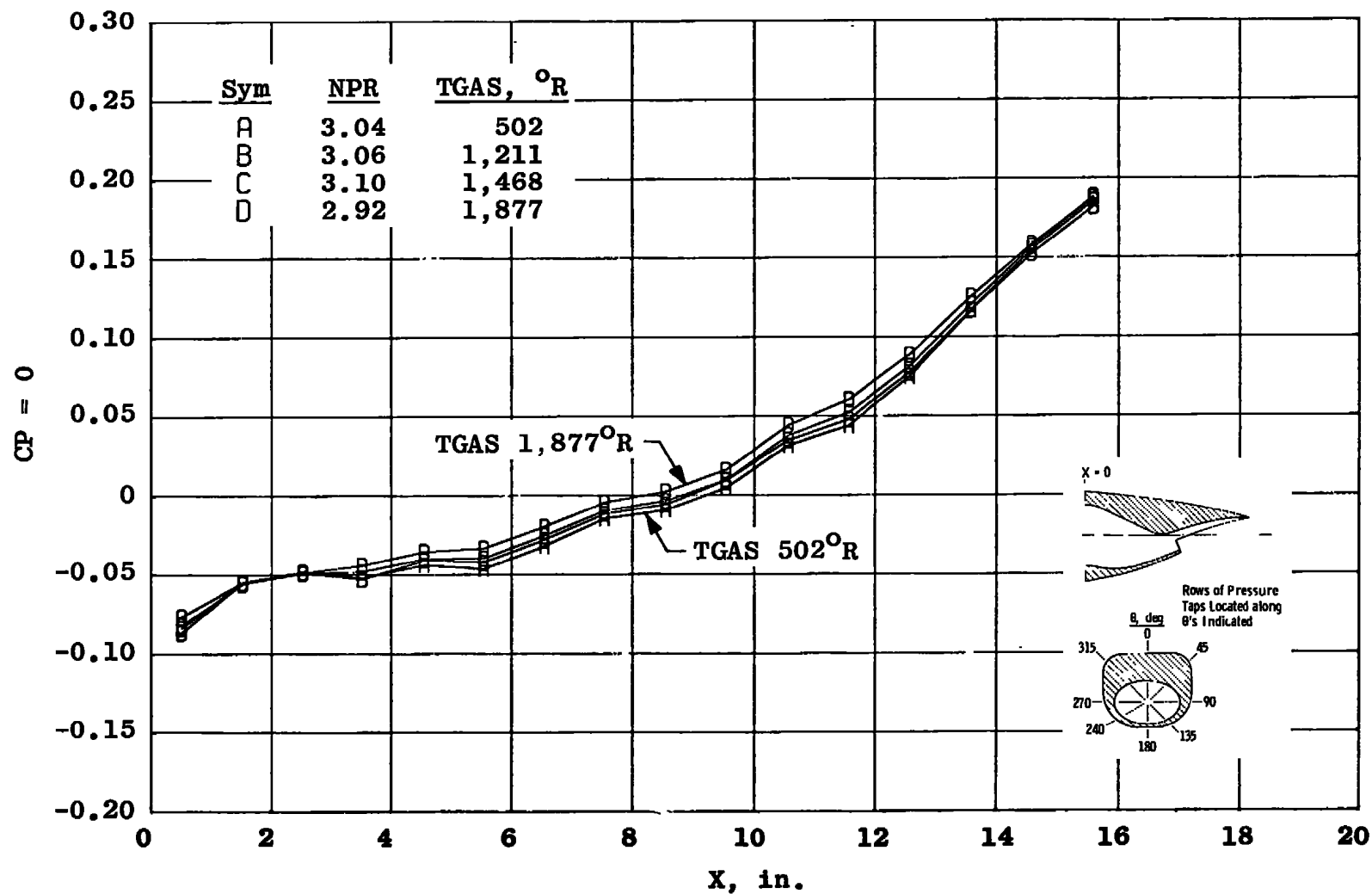


Figure 9. Concluded.

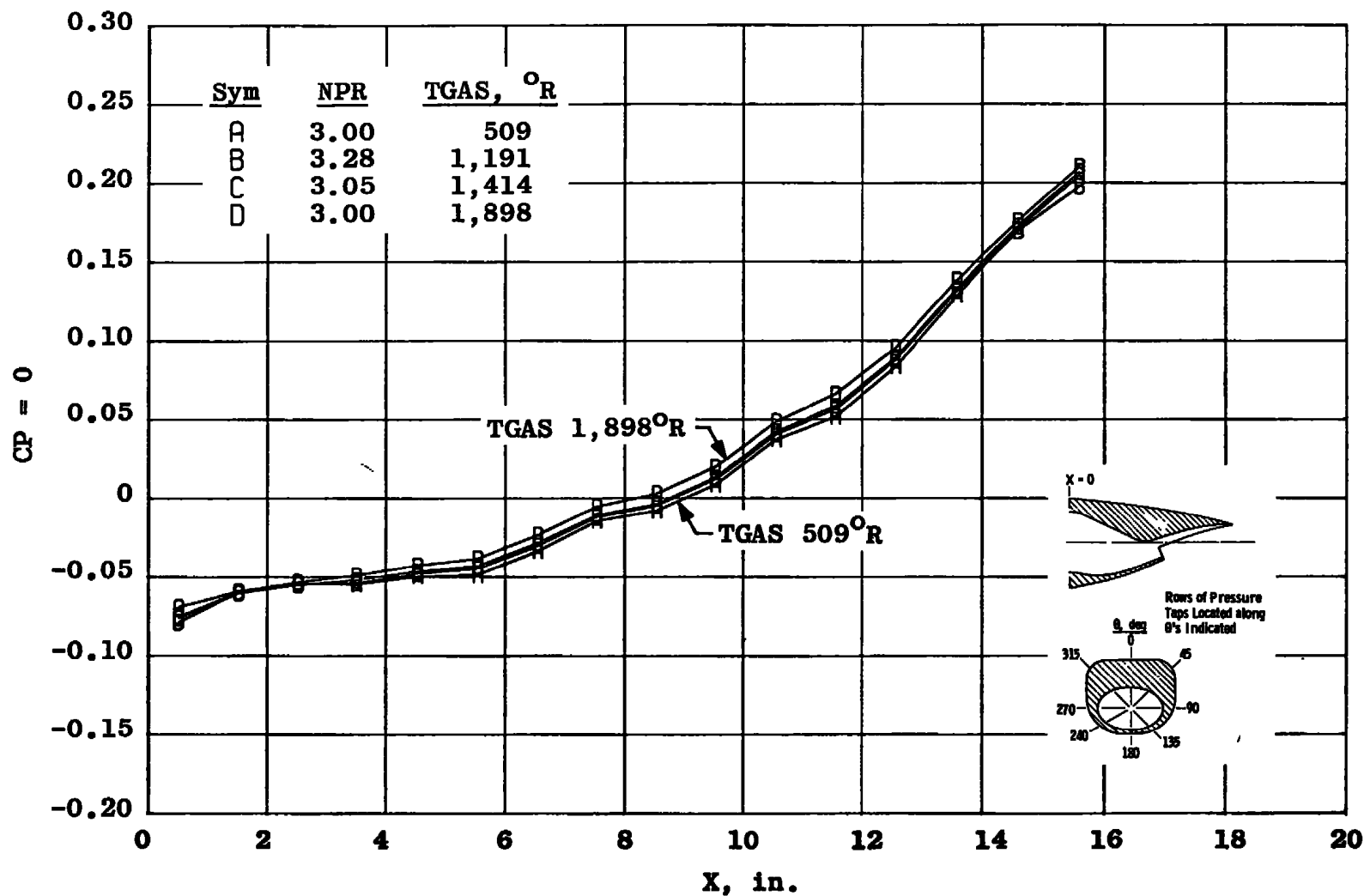
a. $M_\infty = 0.60$ Figure 10. Effect of Mach number on nozzle afterbody pressure distribution, $\theta = 0$.



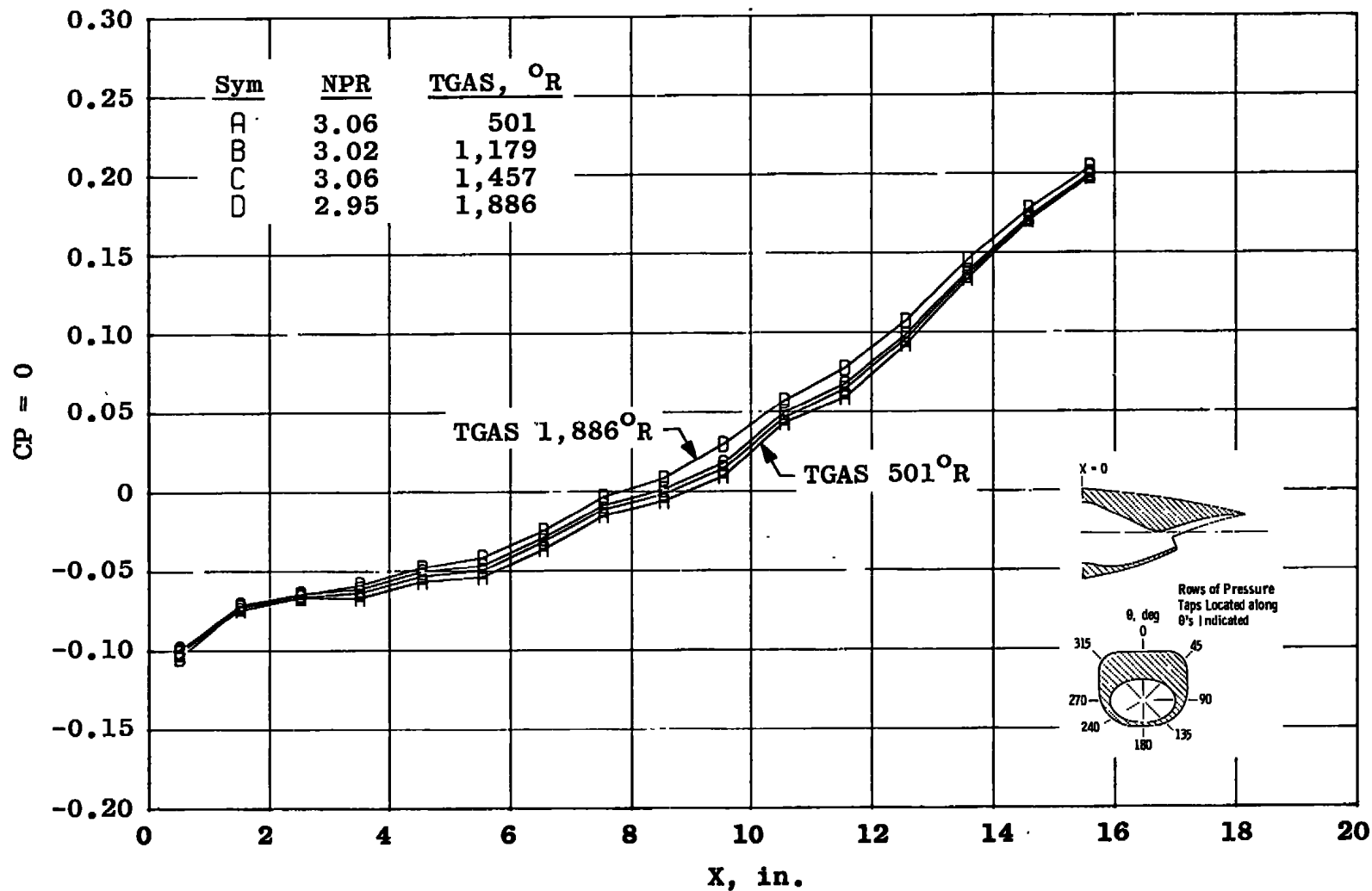
b. $M_\infty = 0.70$
Figure 10. Continued.



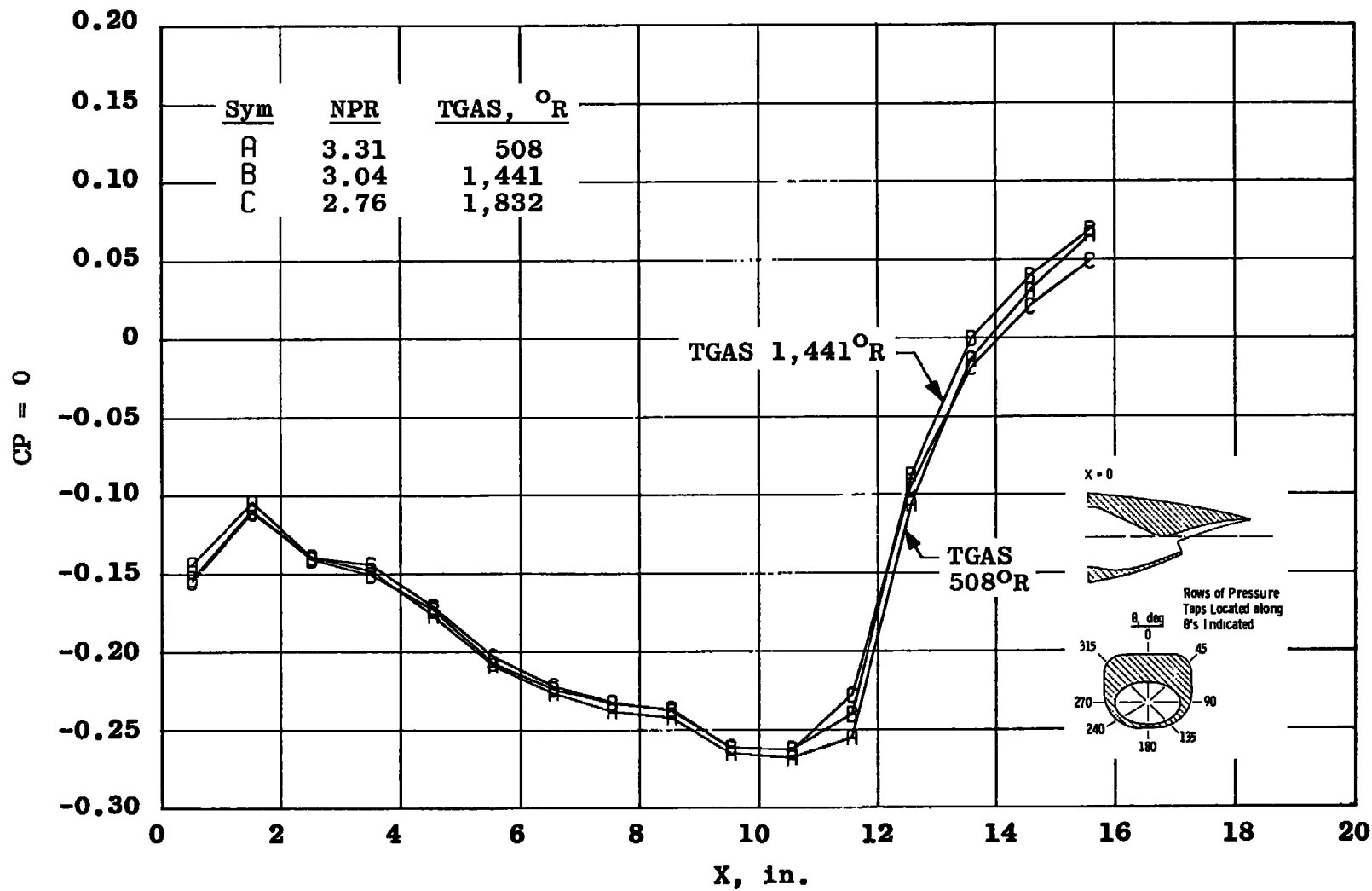
c. $M_{\infty} = 0.80$
Figure 10. Continued.



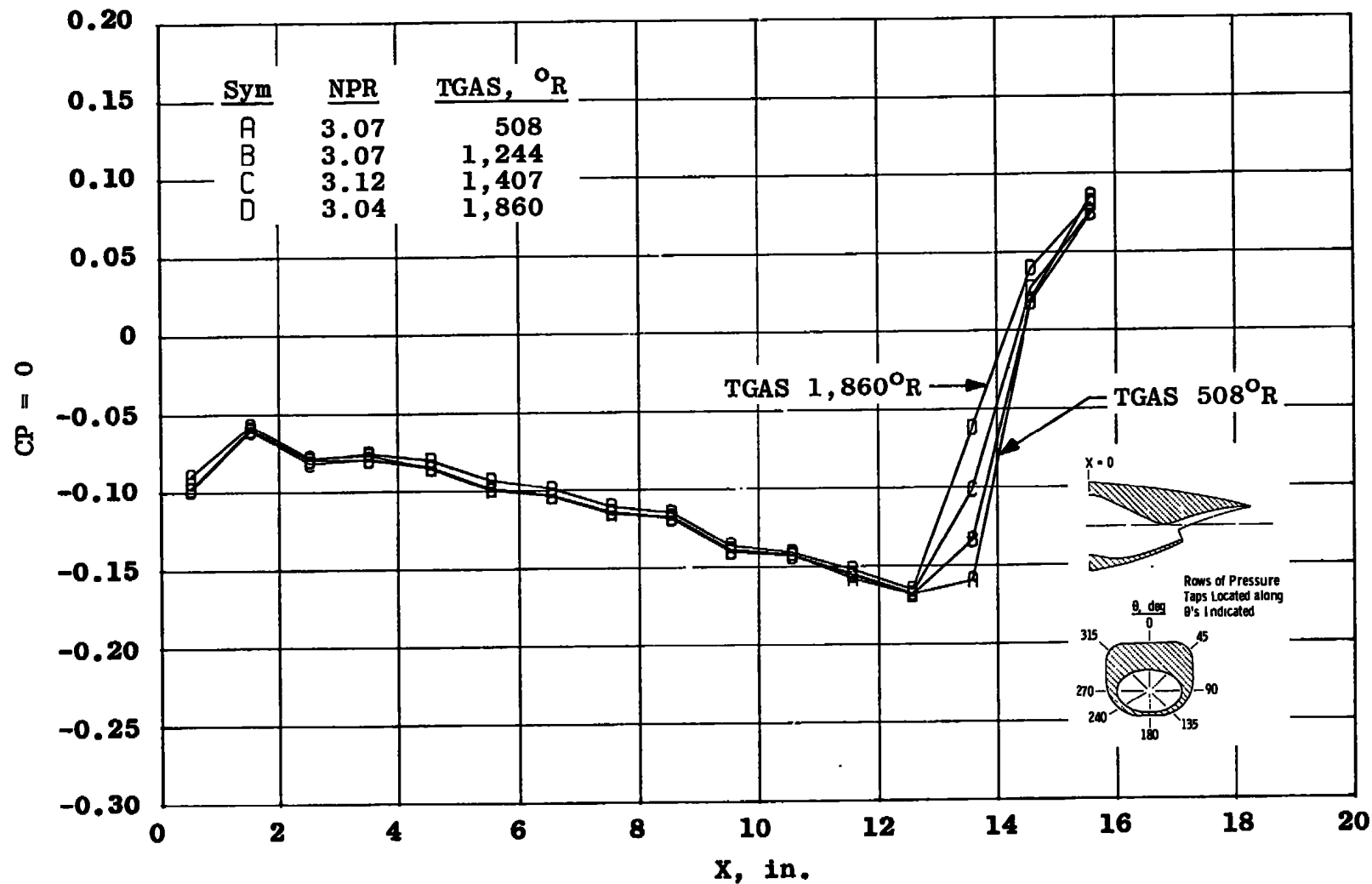
d. $M_\infty = 0.85$
Figure 10. Continued.



e. $M_\infty = 0.90$
Figure 10. Continued.



f. $M_\infty = 1.20$
Figure 10. Continued.



g. $M_\infty = 1.40$
Figure 10. Concluded.

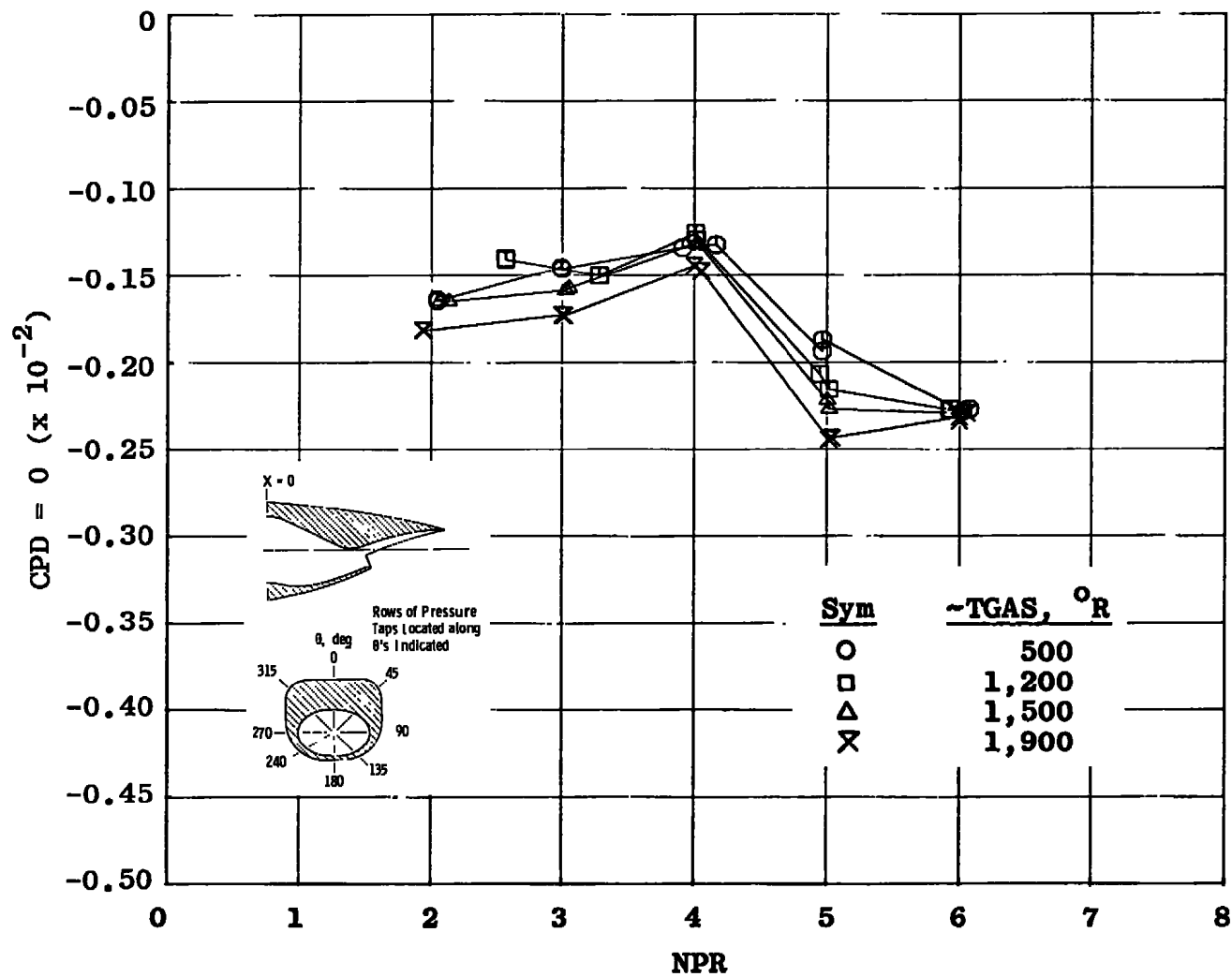
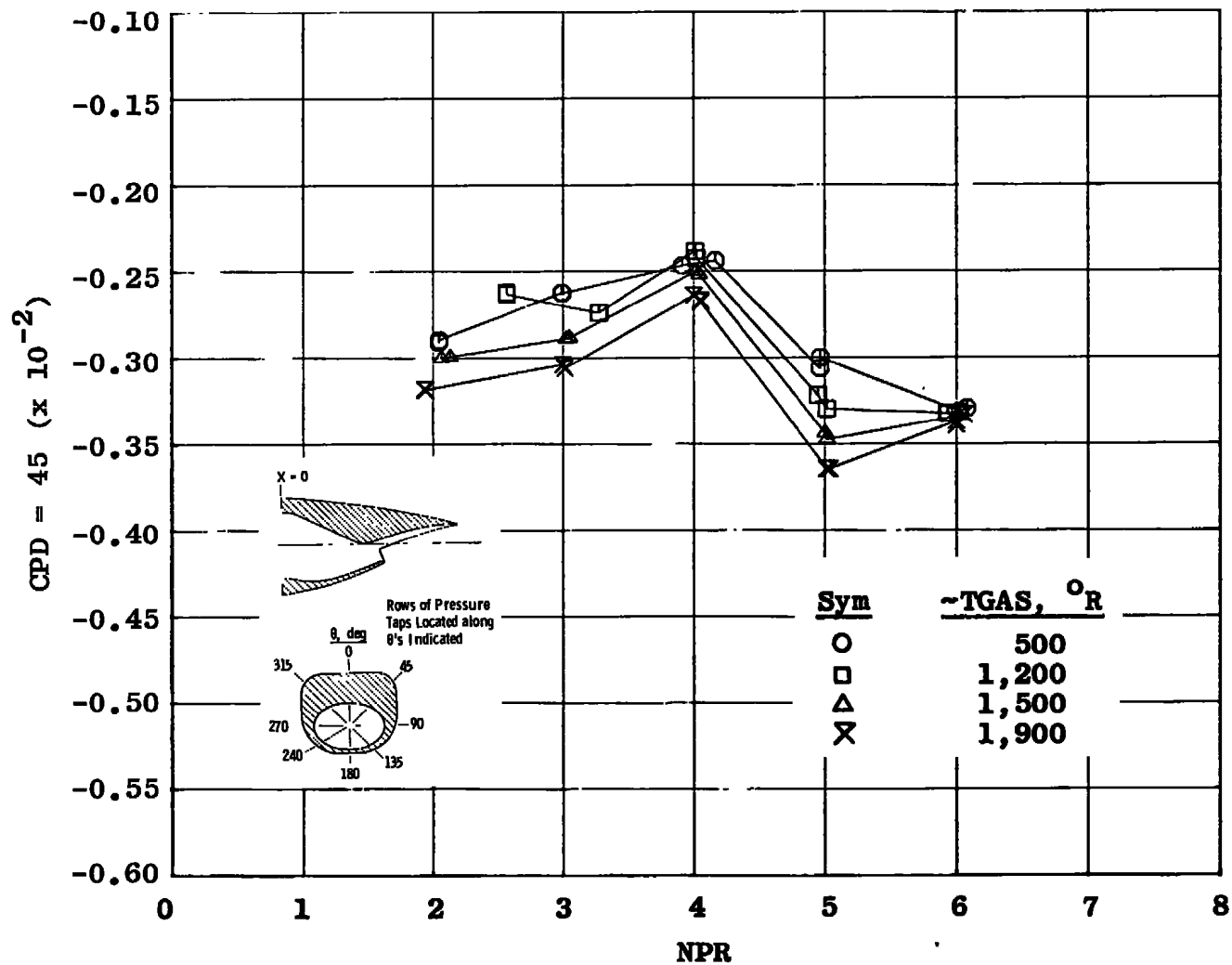
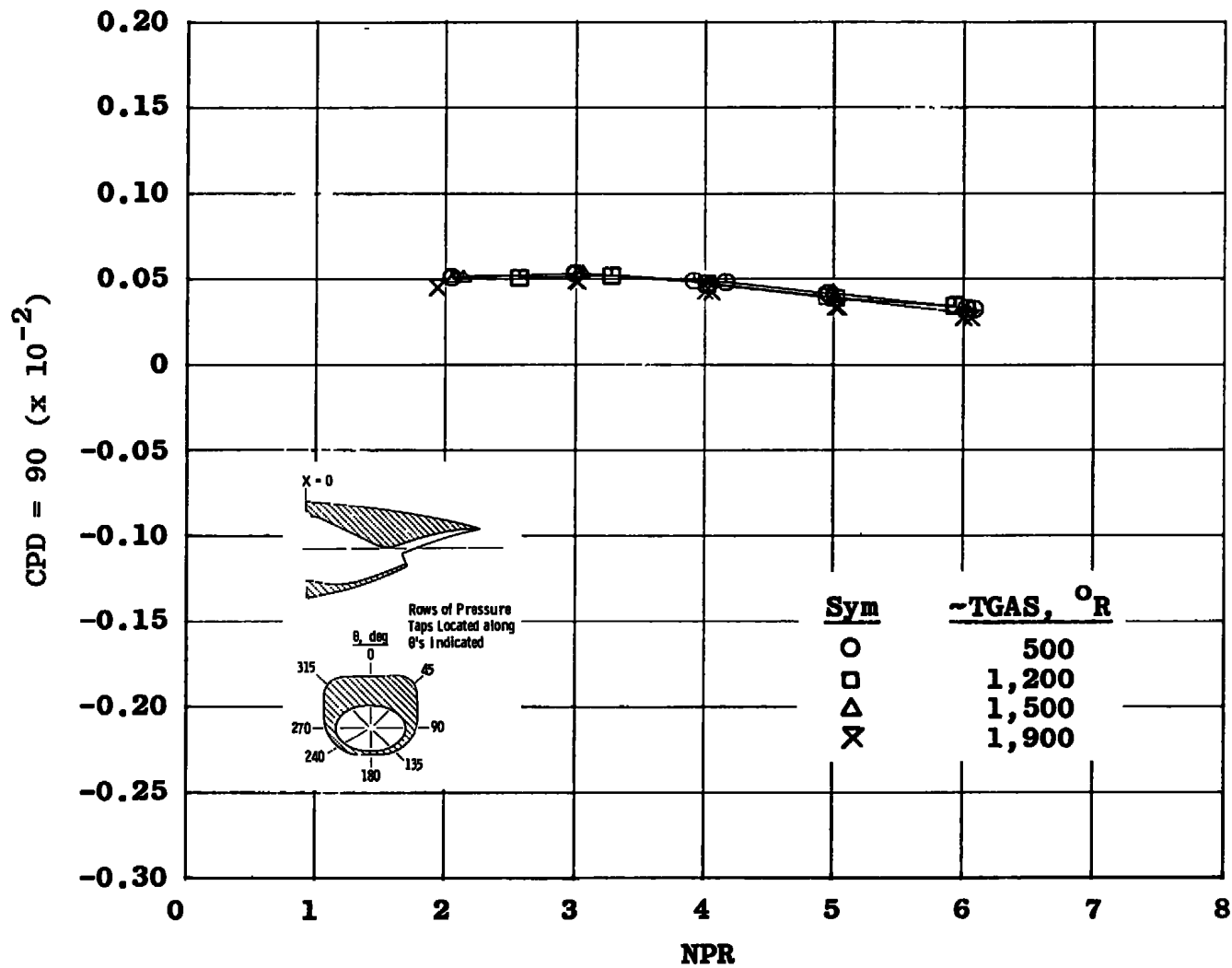


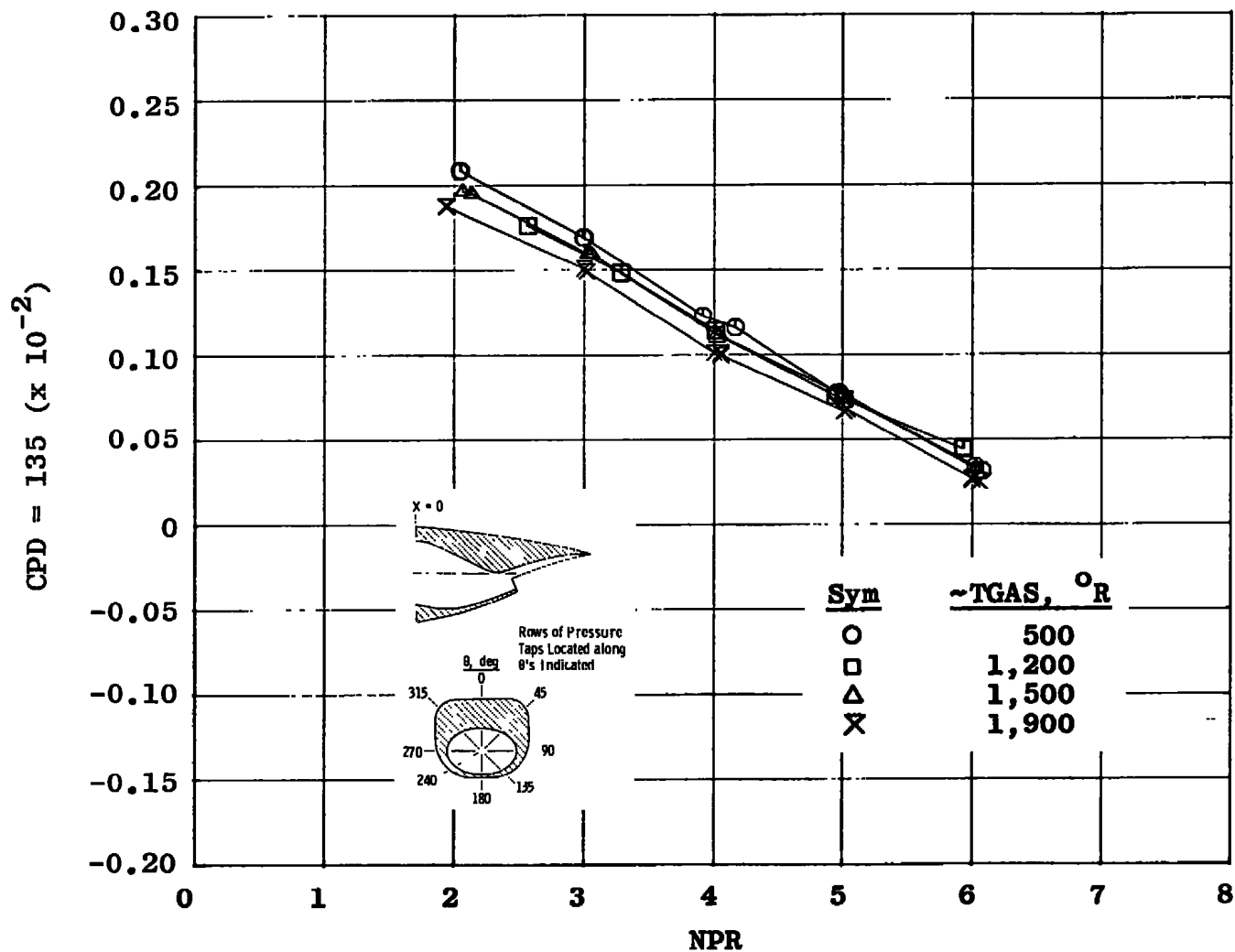
Figure 11. Pressure drag coefficient as function of NPR for four exhaust plume temperatures, $M_{\infty} = 0.85$.



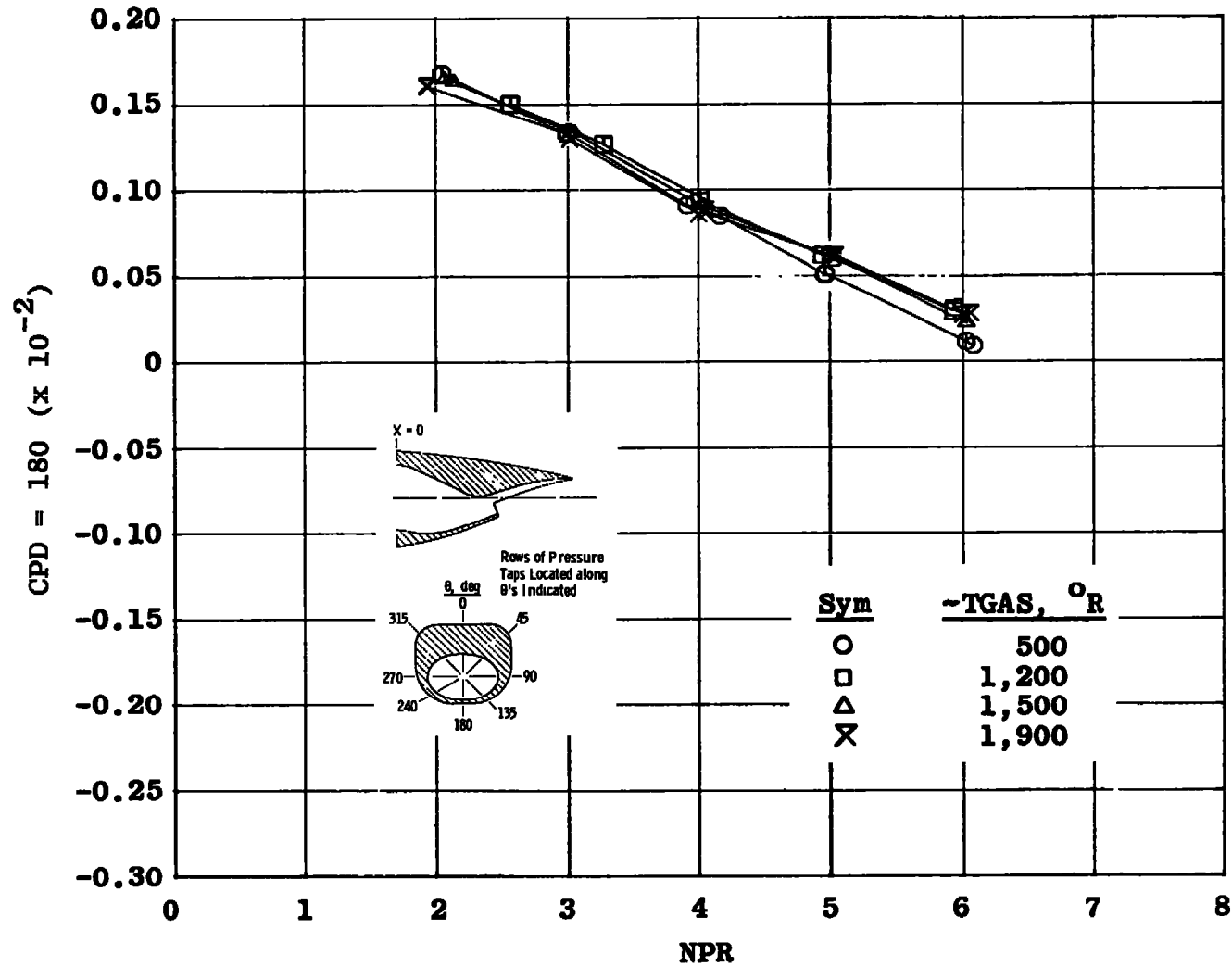
b. $\theta = 45$ deg
Figure 11. Continued.



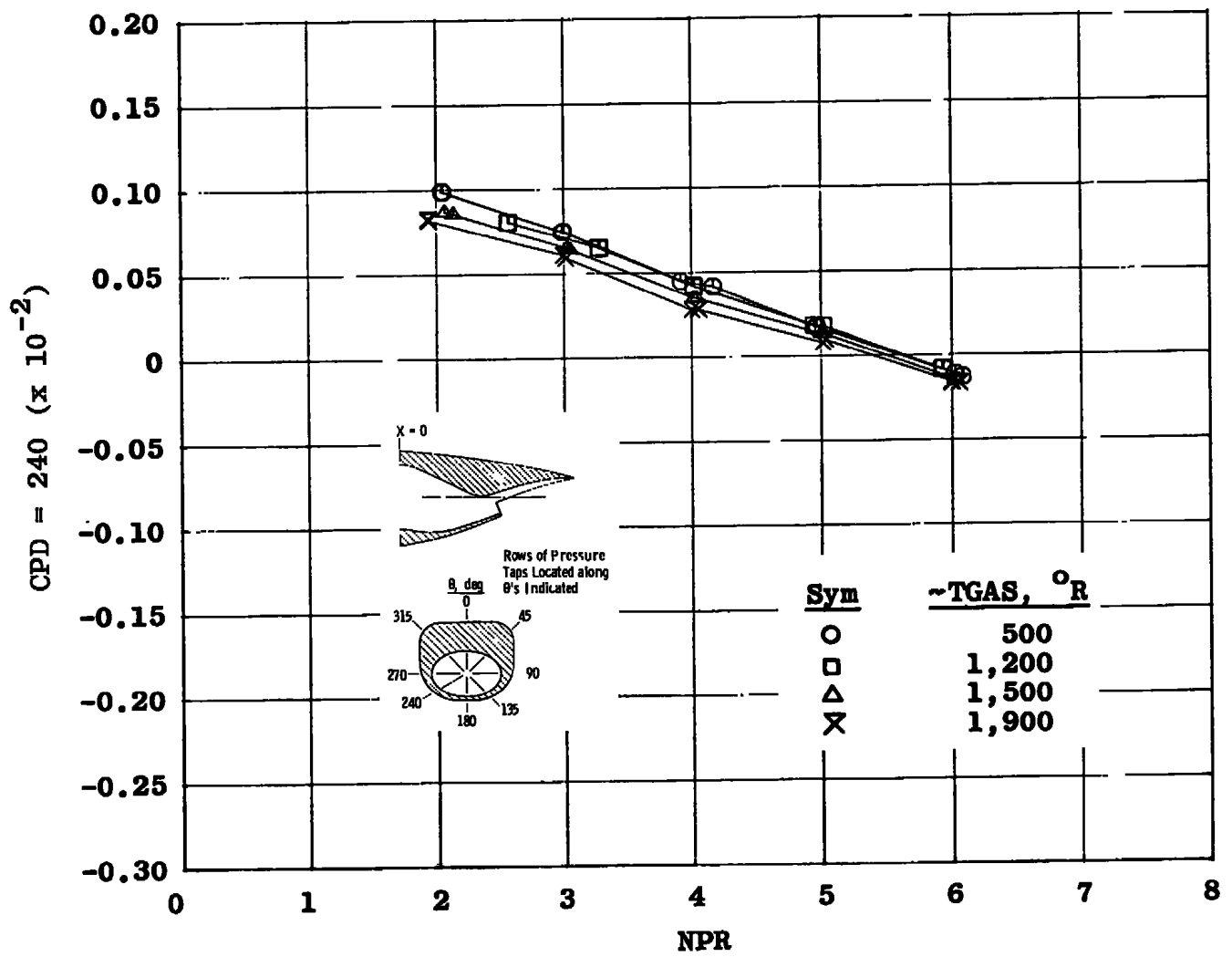
c. $\theta = 90$ deg
Figure 11. Continued.



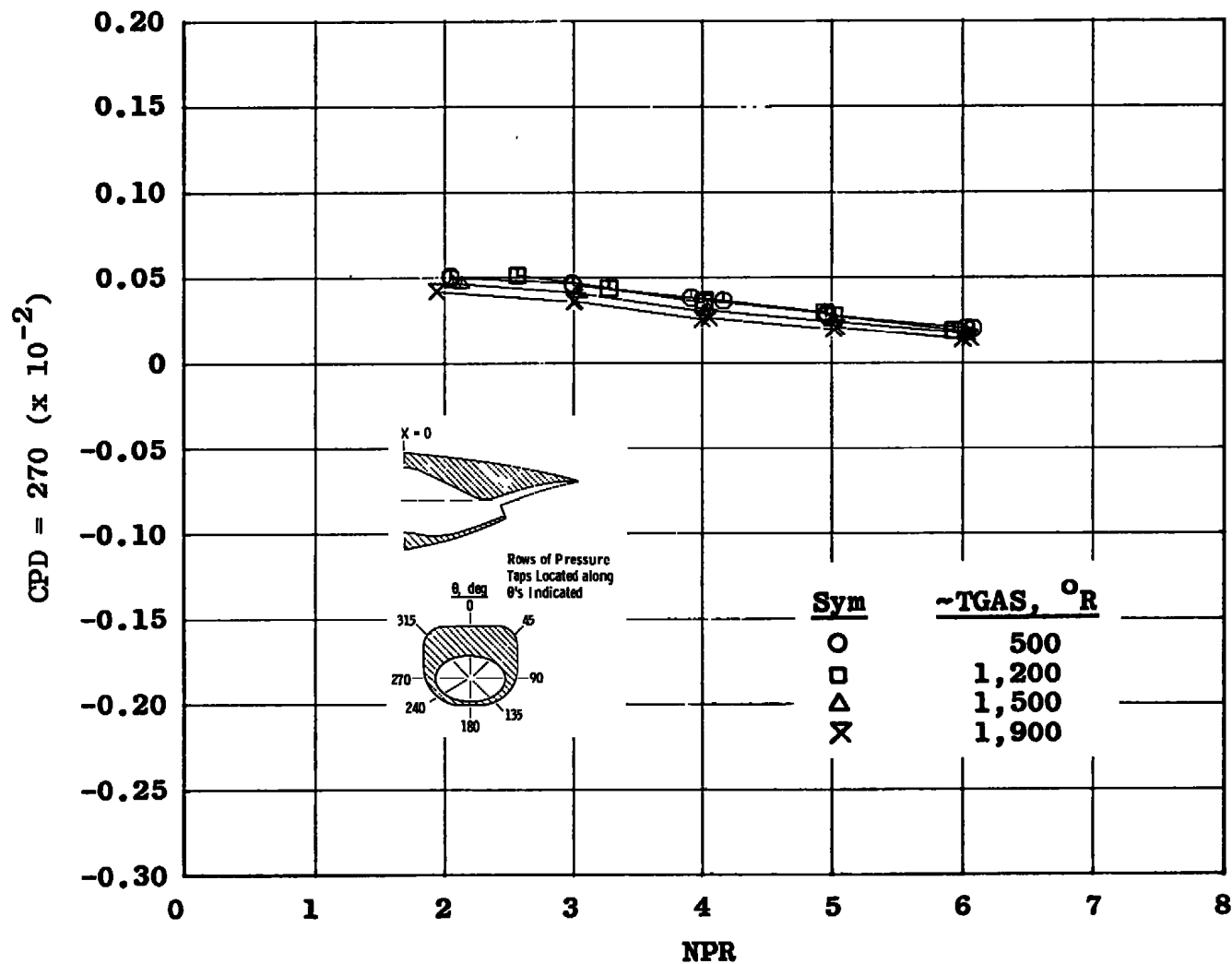
d. $\theta = 135$ deg
Figure 11. Continued.



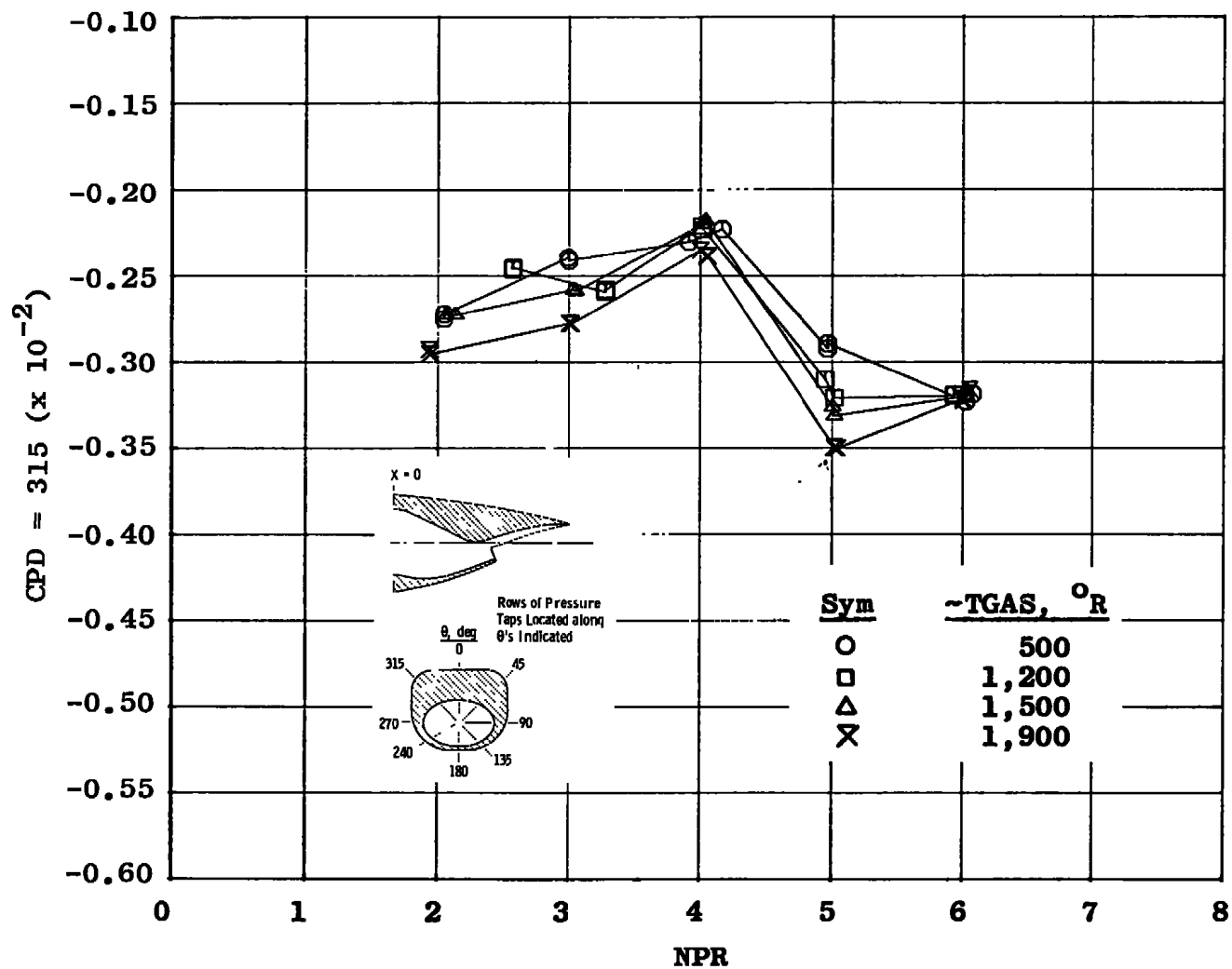
e. $\theta = 180$ deg
Figure 11. Continued.



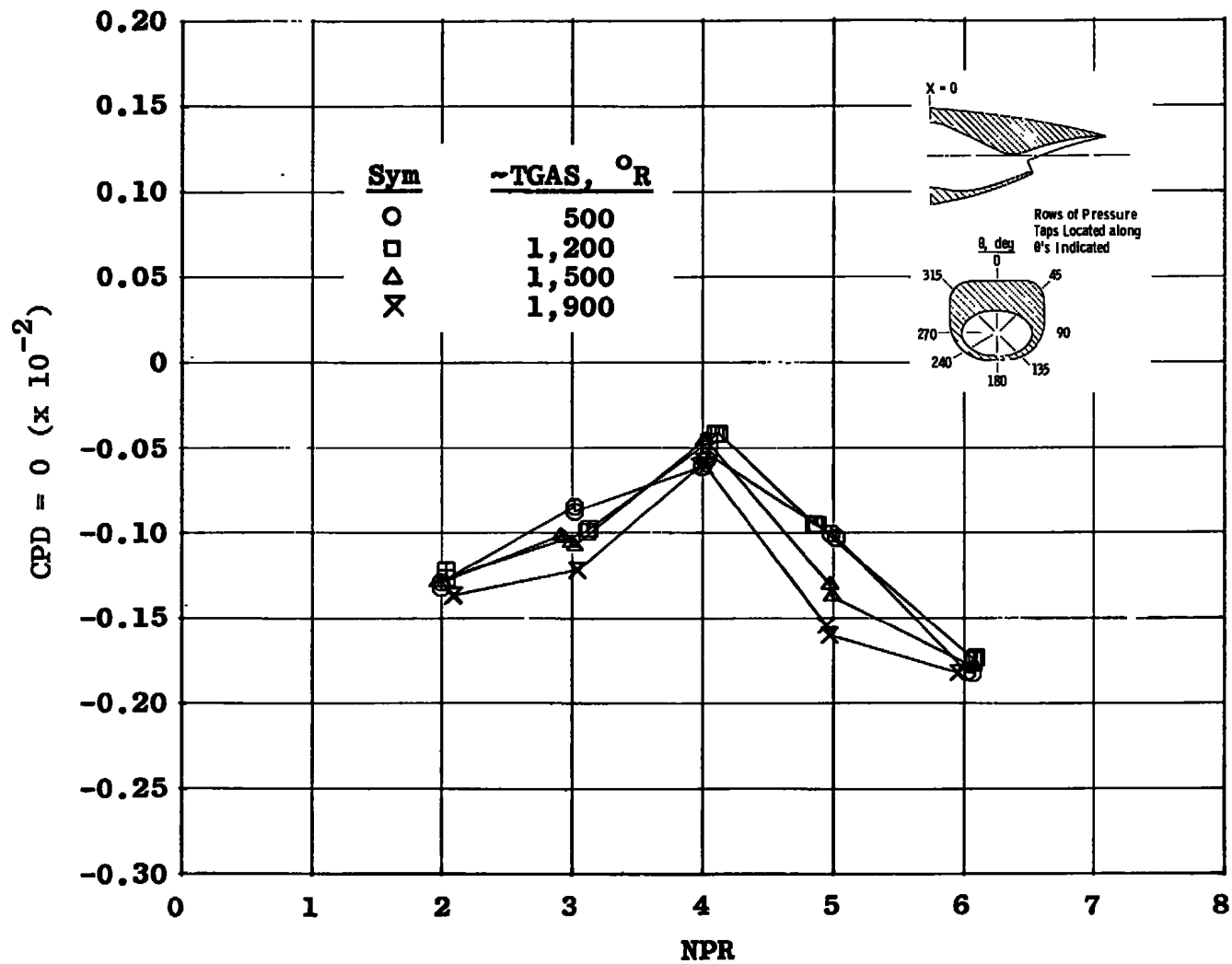
f. $\theta = 240$ deg
Figure 11. Continued.



g. $\theta = 270$ deg
Figure 11. Continued.

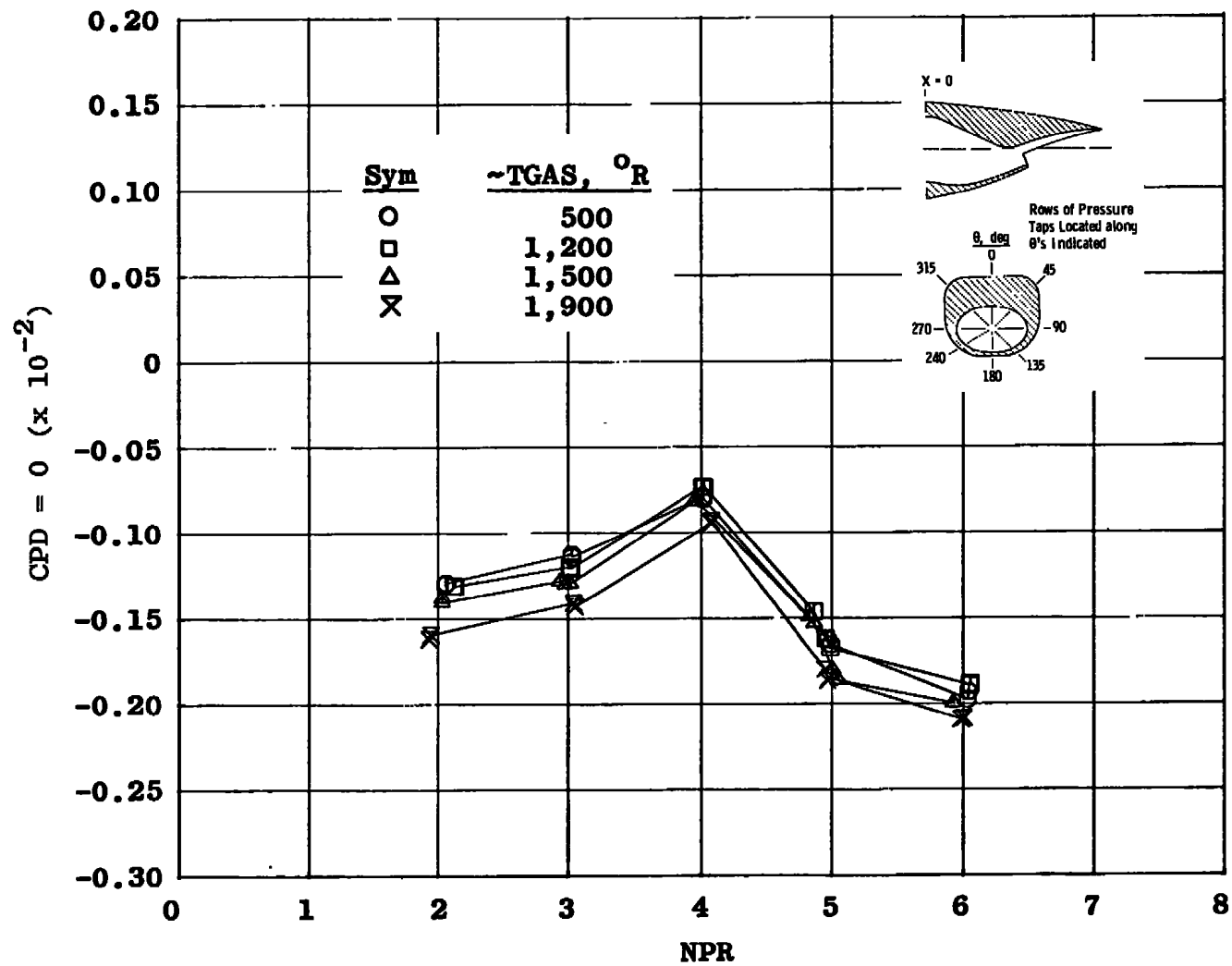


h. $\theta = 315$ deg
Figure 11. Concluded.

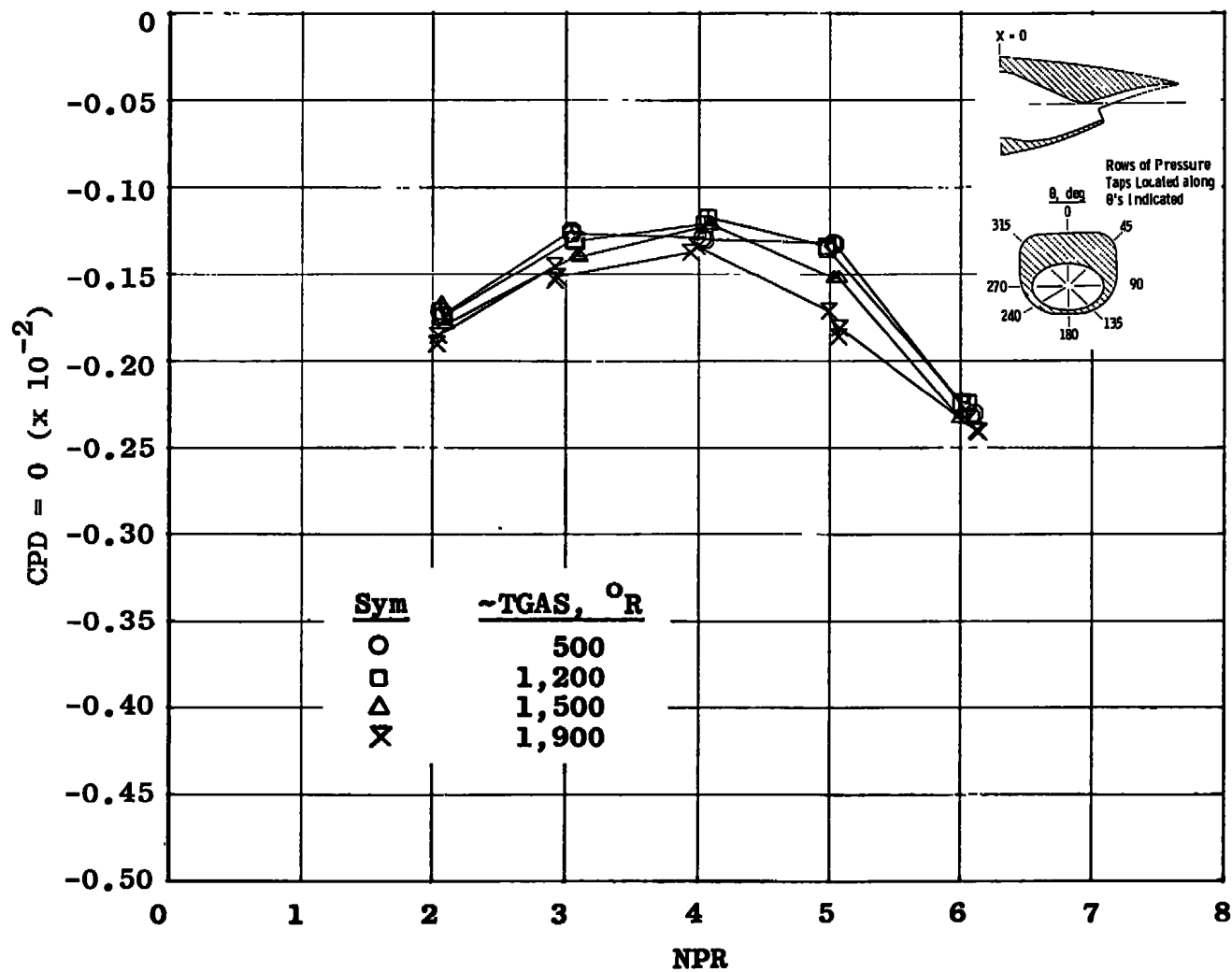


a. $M_\infty = 0.60$

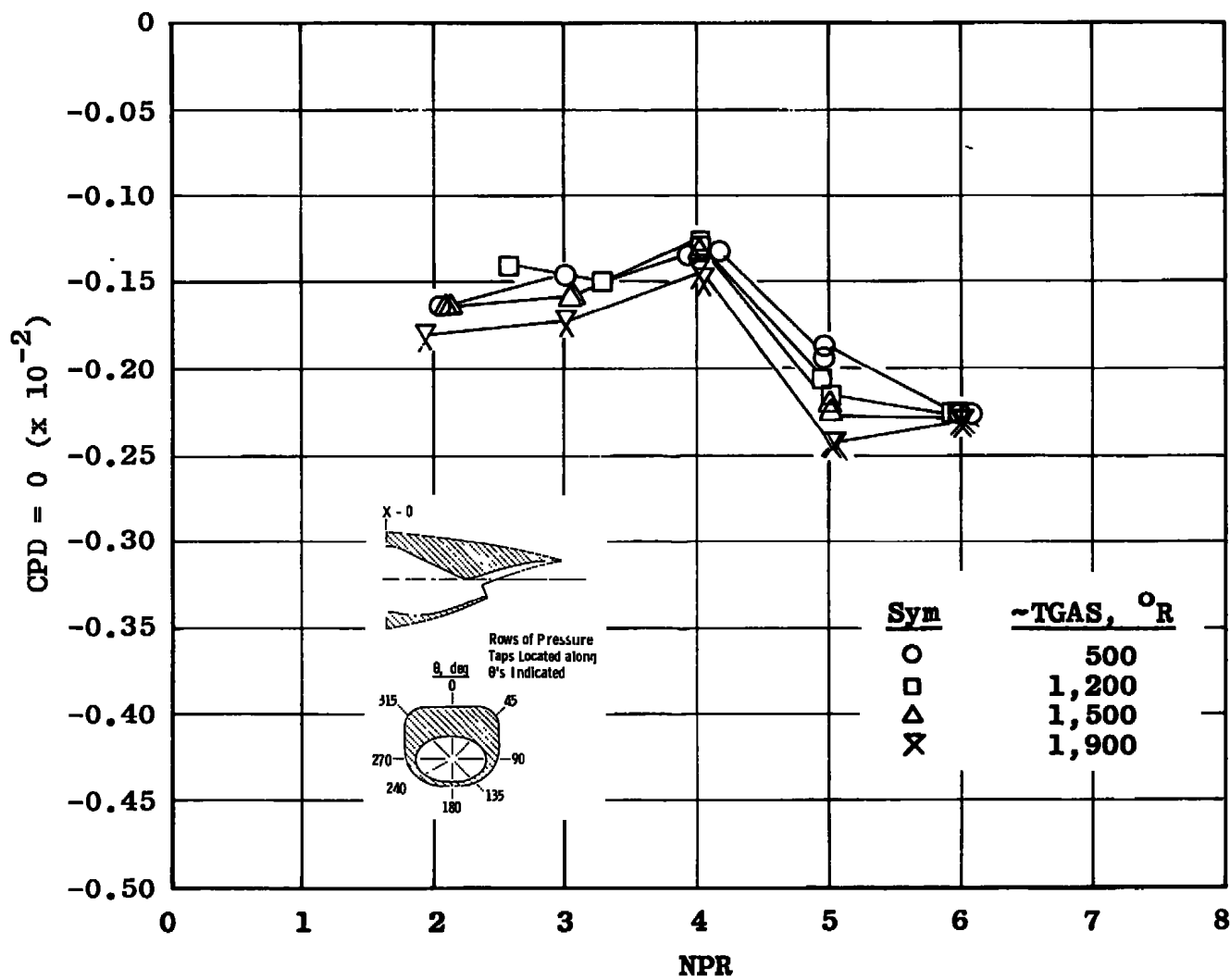
Figure 12. Effect of Mach number on pressure drag coefficient at four exhaust plume temperatures, $\theta = 0$.



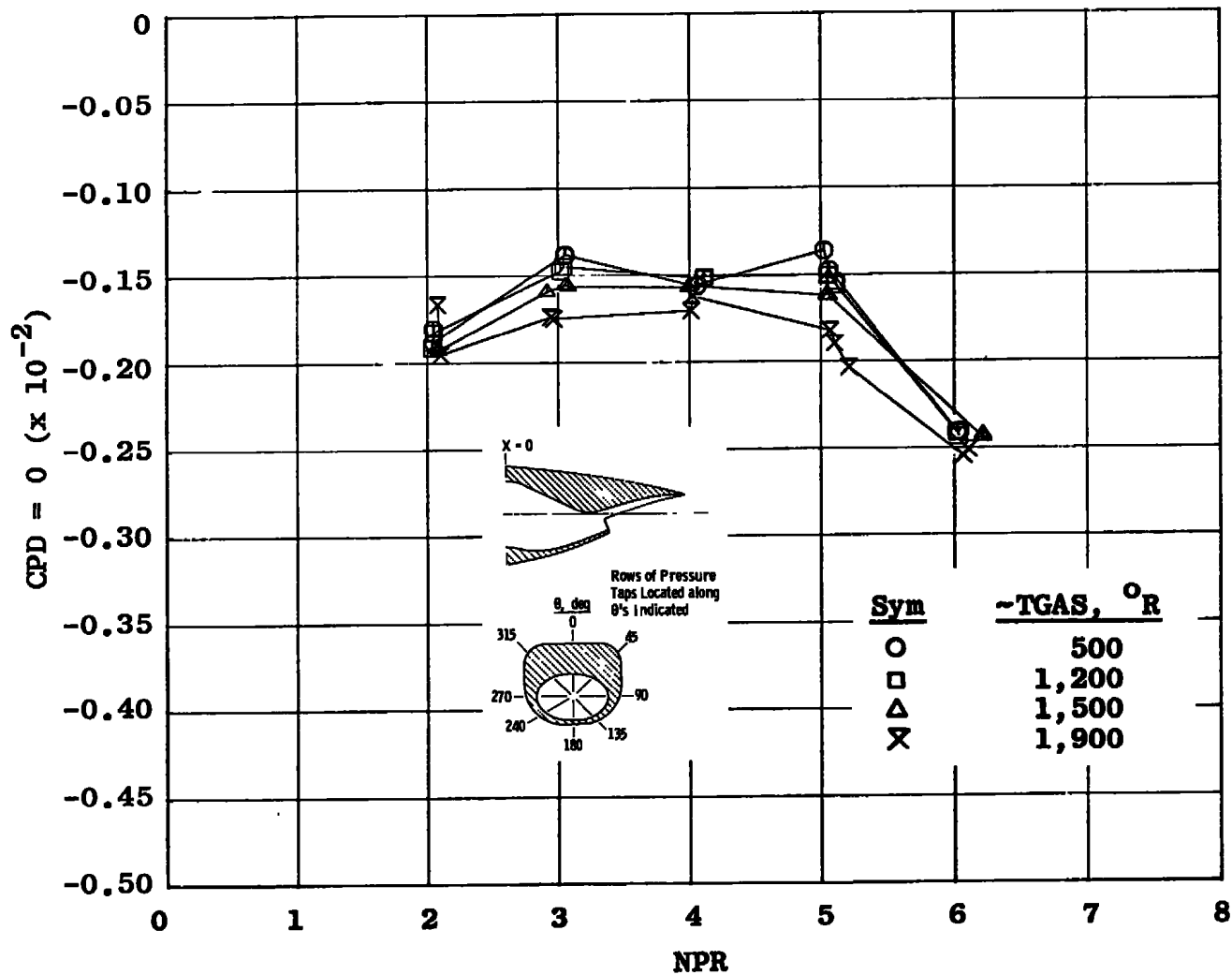
b. $M_\infty = 0.70$
Figure 12. Continued.



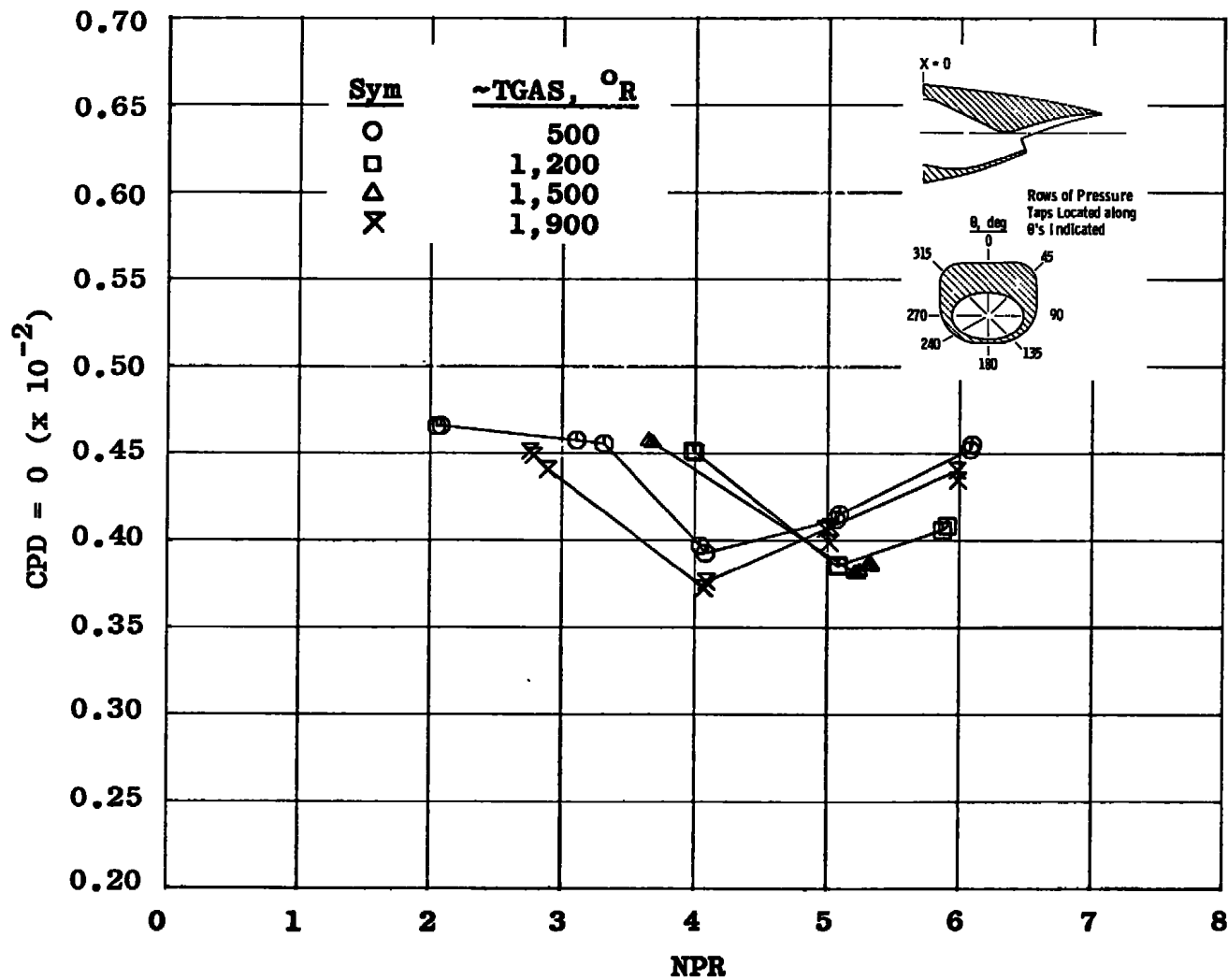
c. $M_\infty = 0.80$
Figure 12. Continued.



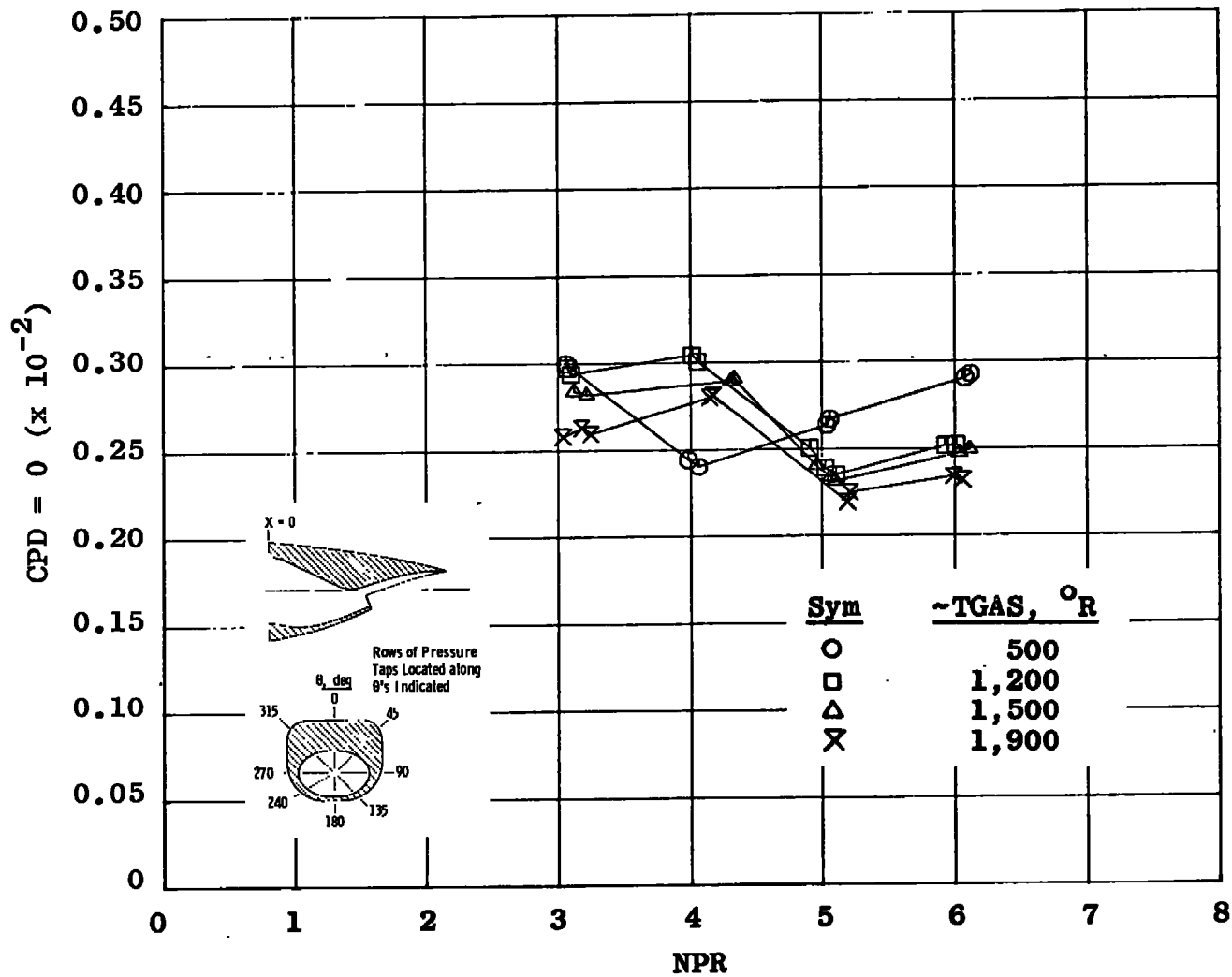
d. $M_{\infty} = 0.85$
Figure 12. Continued.



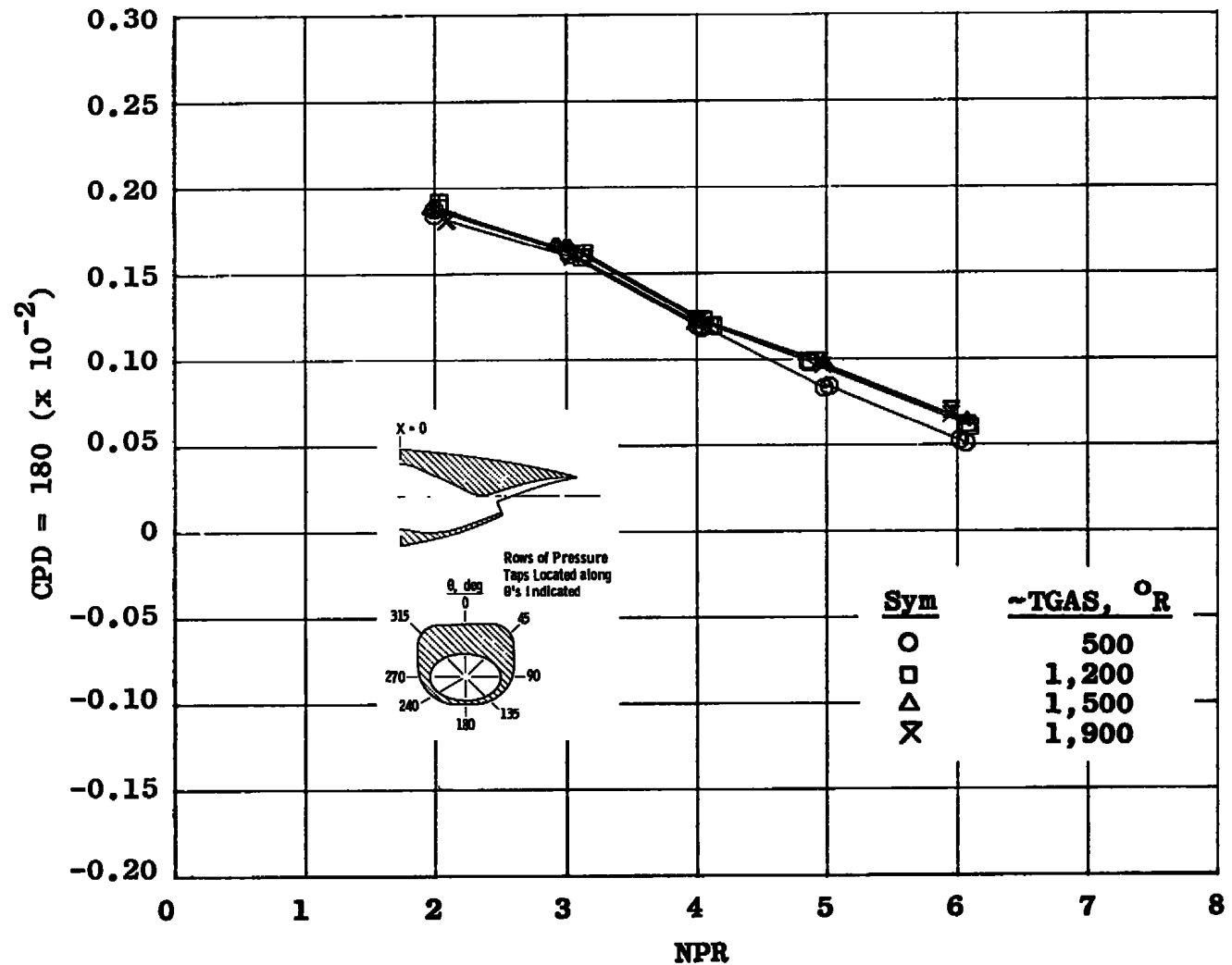
e. $M_\infty = 0.90$
Figure 12. Continued.



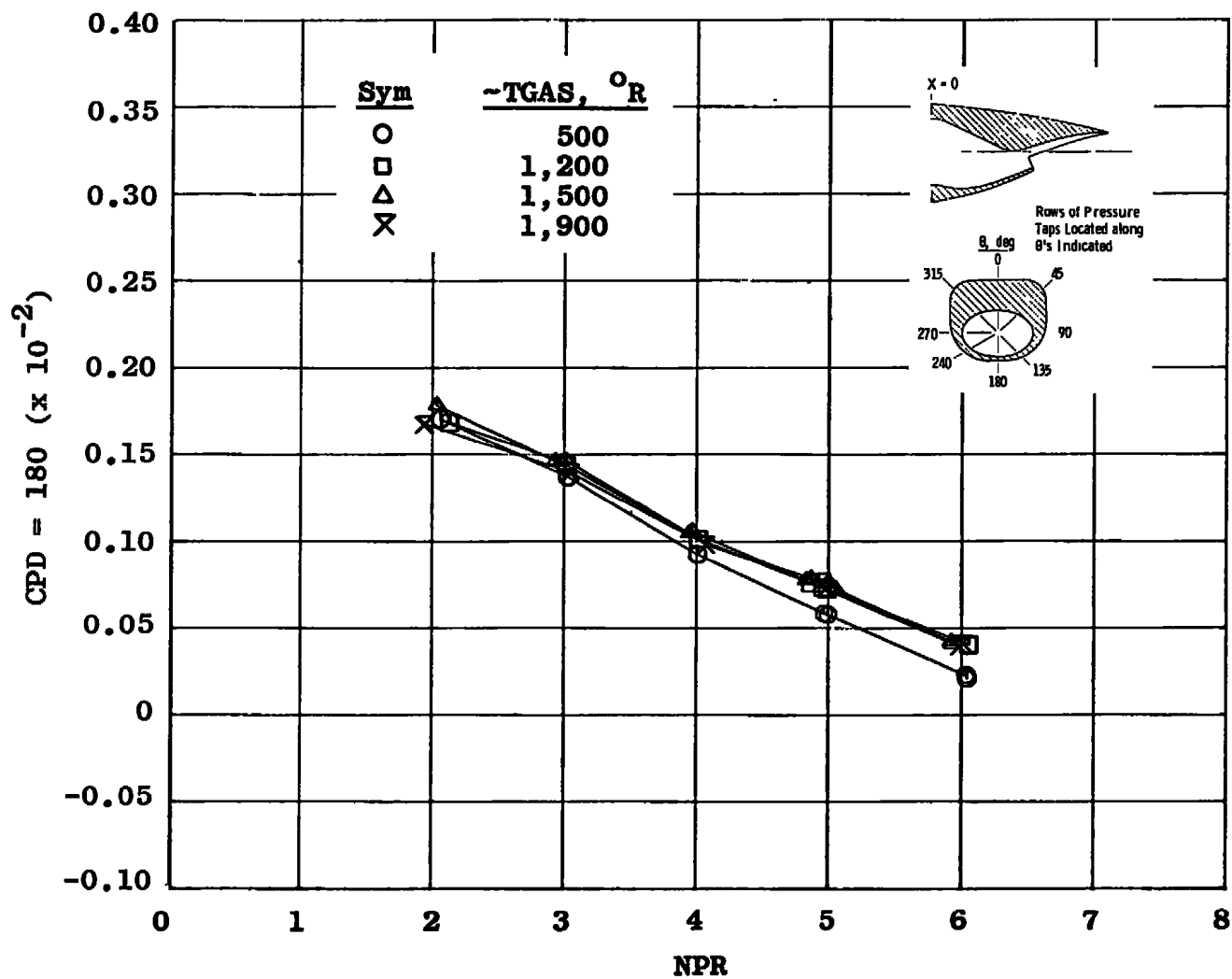
f. $M_\infty = 1.20$
Figure 12. Continued.



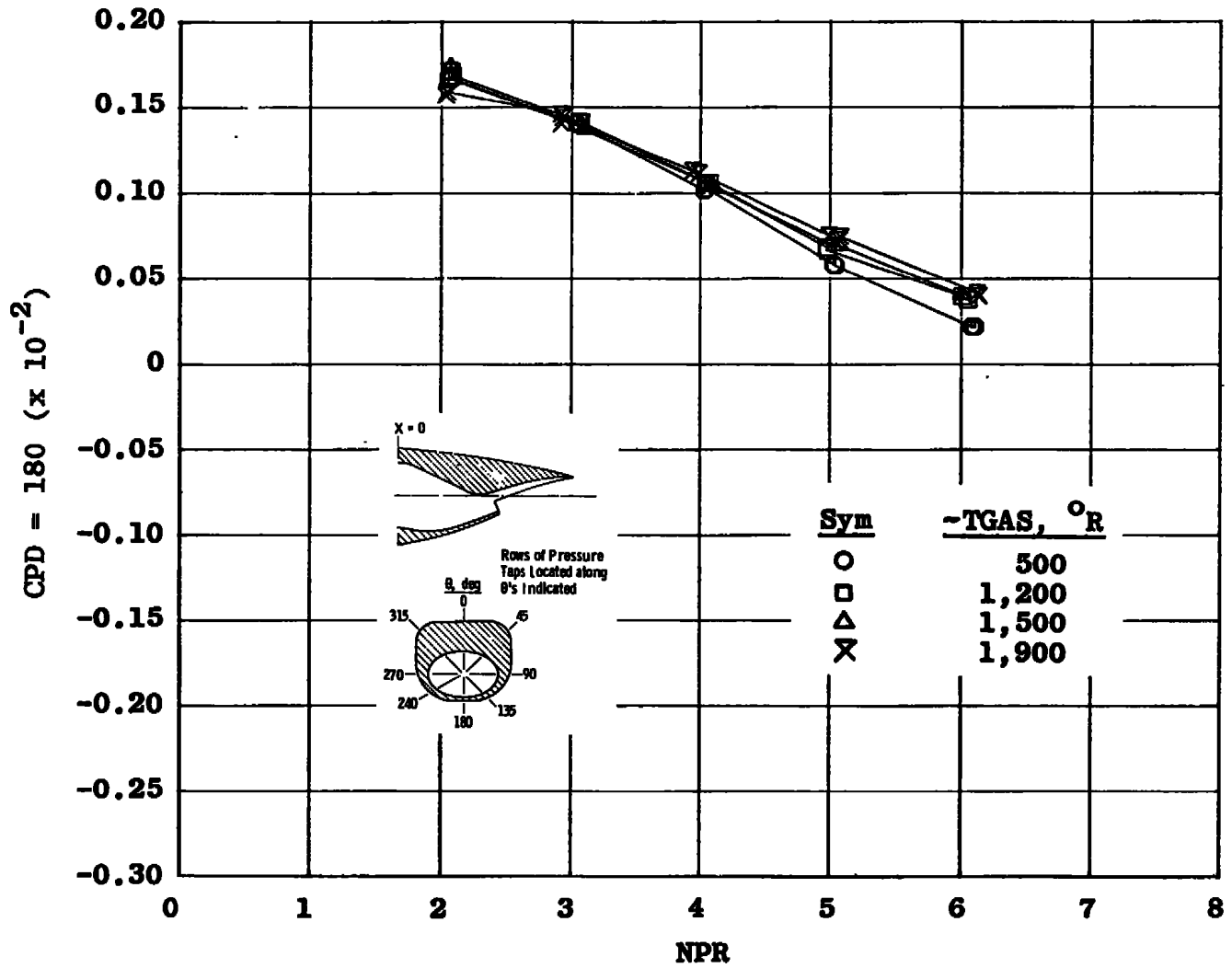
g. $M_\infty = 1.40$
Figure 12. Concluded.



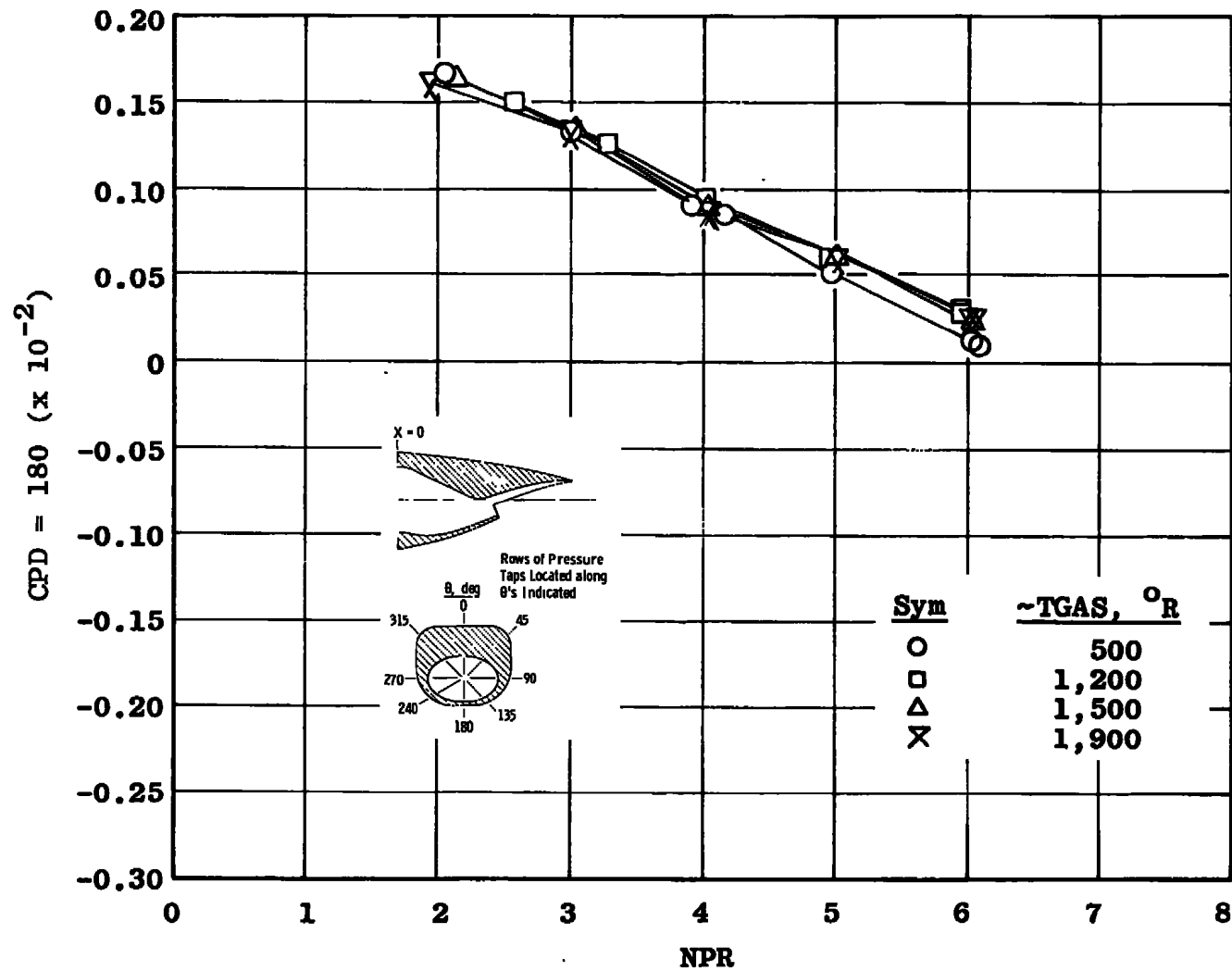
a. $M_\infty = 0.60$
 Figure 13. Effect of Mach number on pressure drag coefficient at four exhaust plume temperatures, $\theta = 180$ degrees.



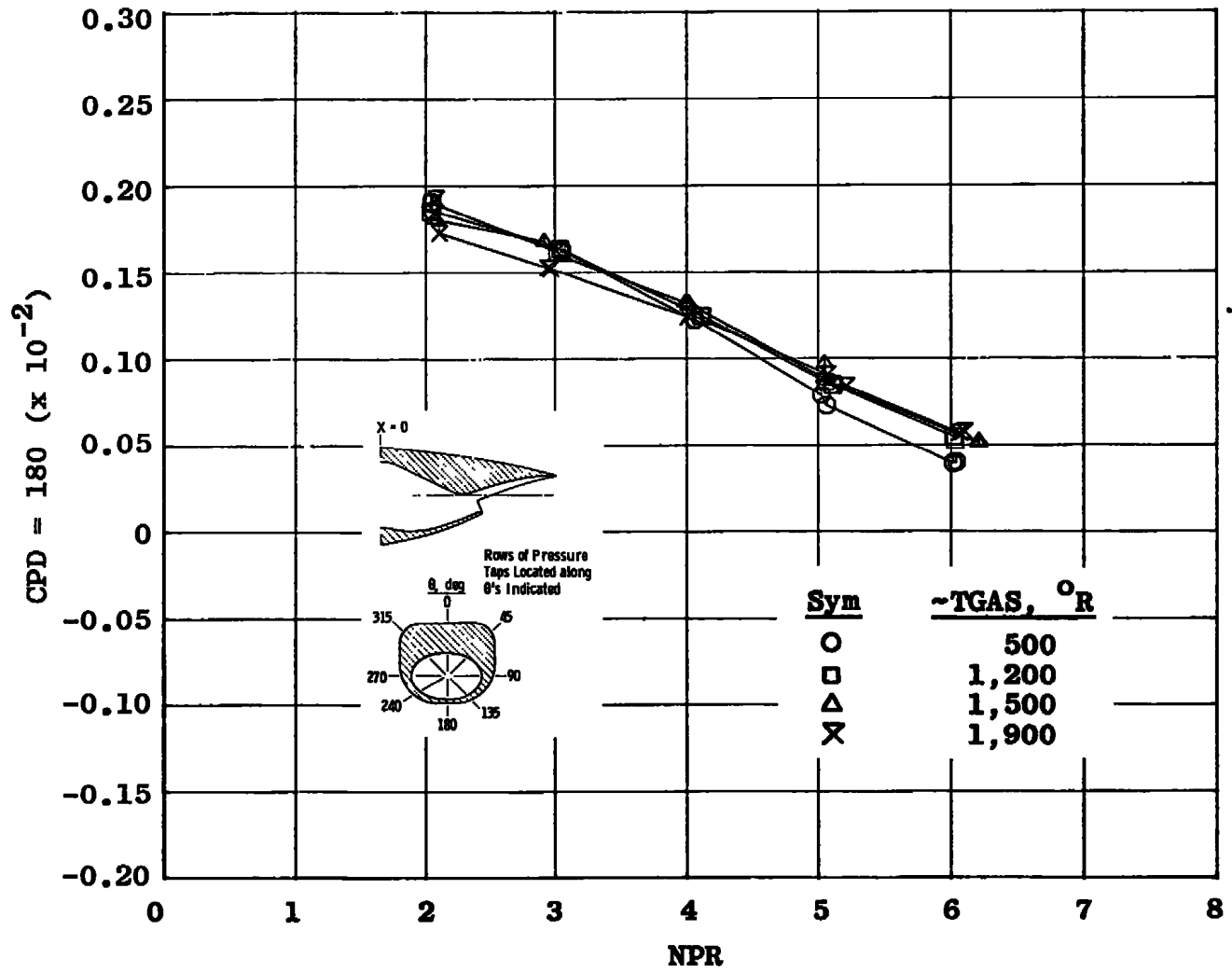
b. $M_{\infty} = 0.70$
Figure 13. Continued.



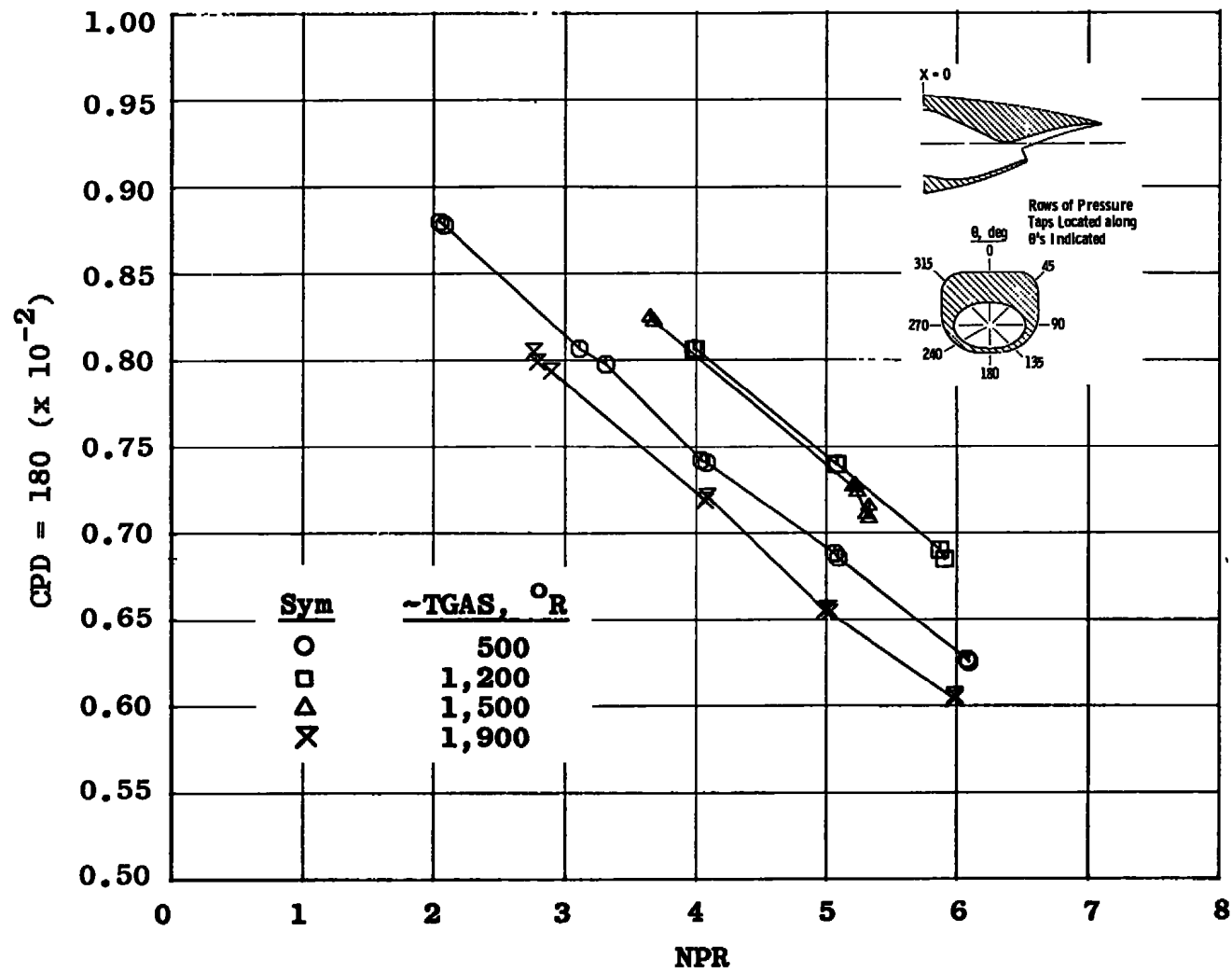
c. $M_\infty = 0.80$
Figure 13. Continued.



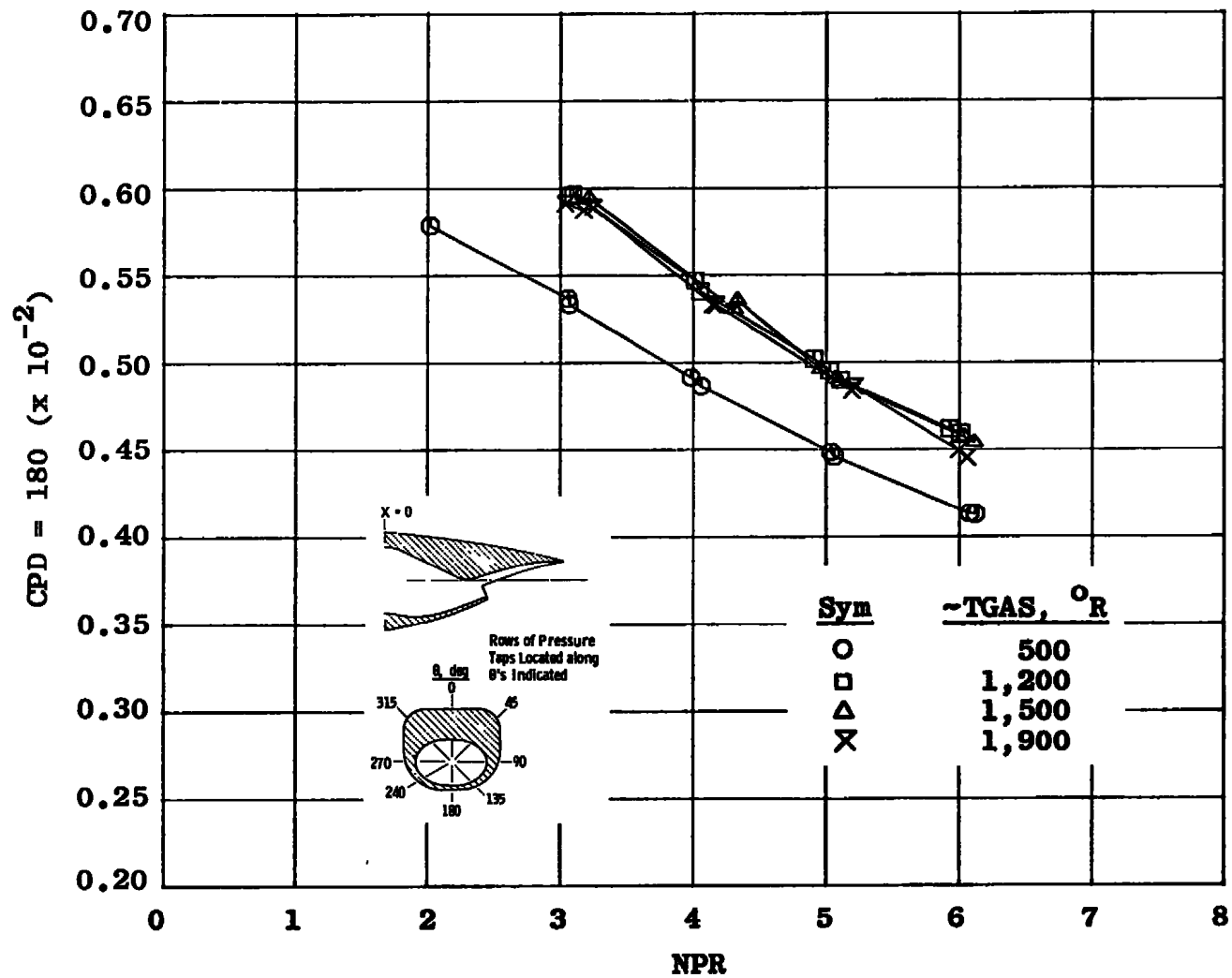
d. $M_{\infty} = 0.85$
Figure 13. Continued.



e. $M_\infty = 0.90$
Figure 13. Continued.



f. $M_{\infty} = 1.20$
Figure 13. Continued.



g. $M_\infty = 1.40$
Figure 13. Concluded.

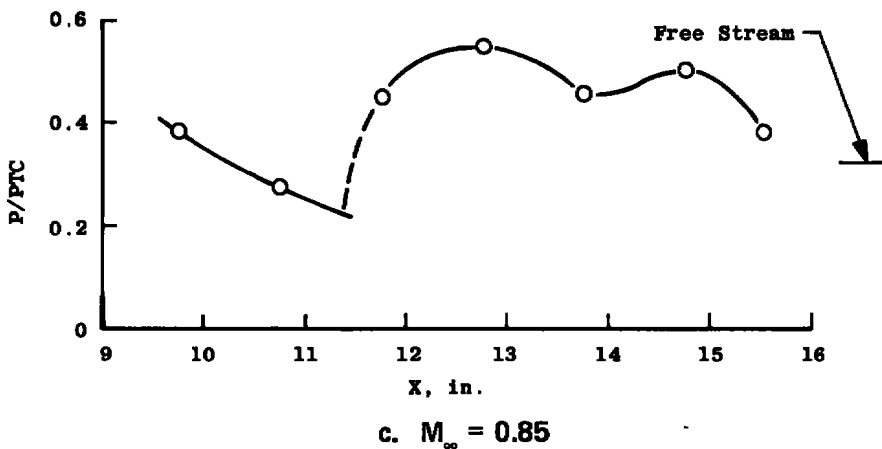
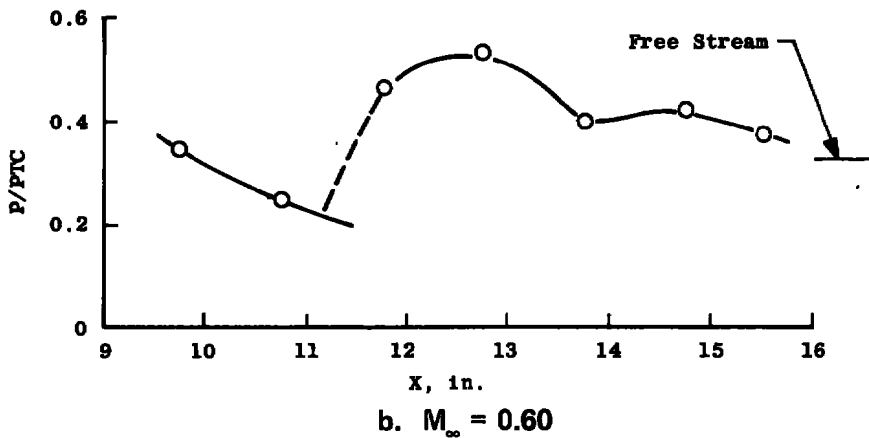
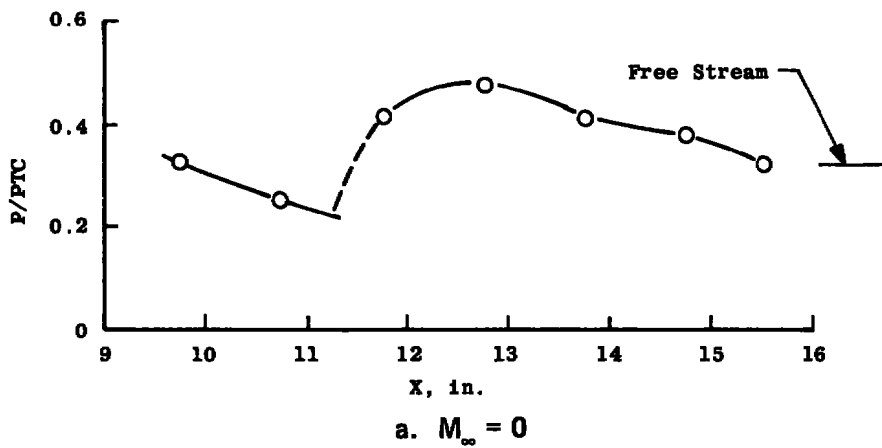
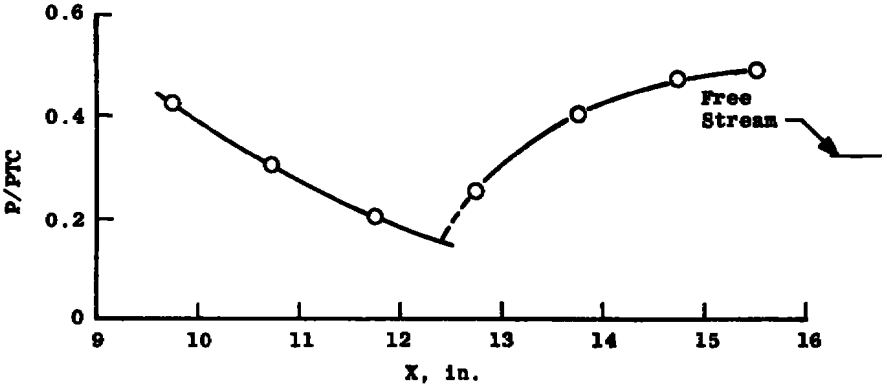
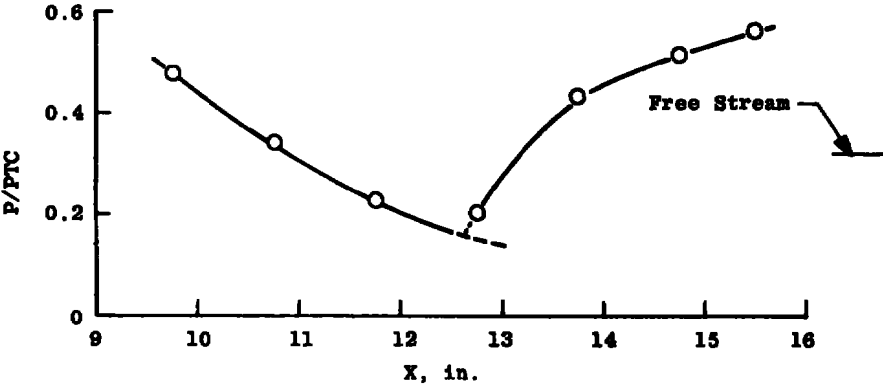


Figure 14. Effect of free-stream Mach number on pressure distribution, internal cowl surface at an NPR of 3.0.



d. $M_{\infty} = 1.20$



e. $M_{\infty} = 1.40$

Figure 14. Concluded.

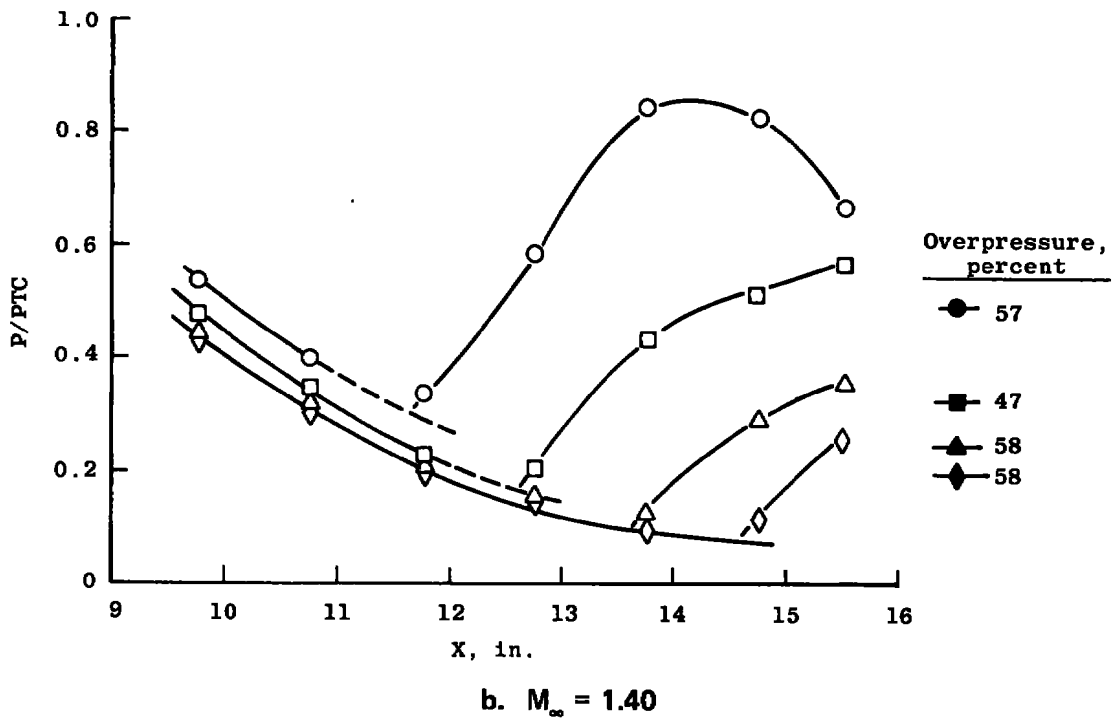
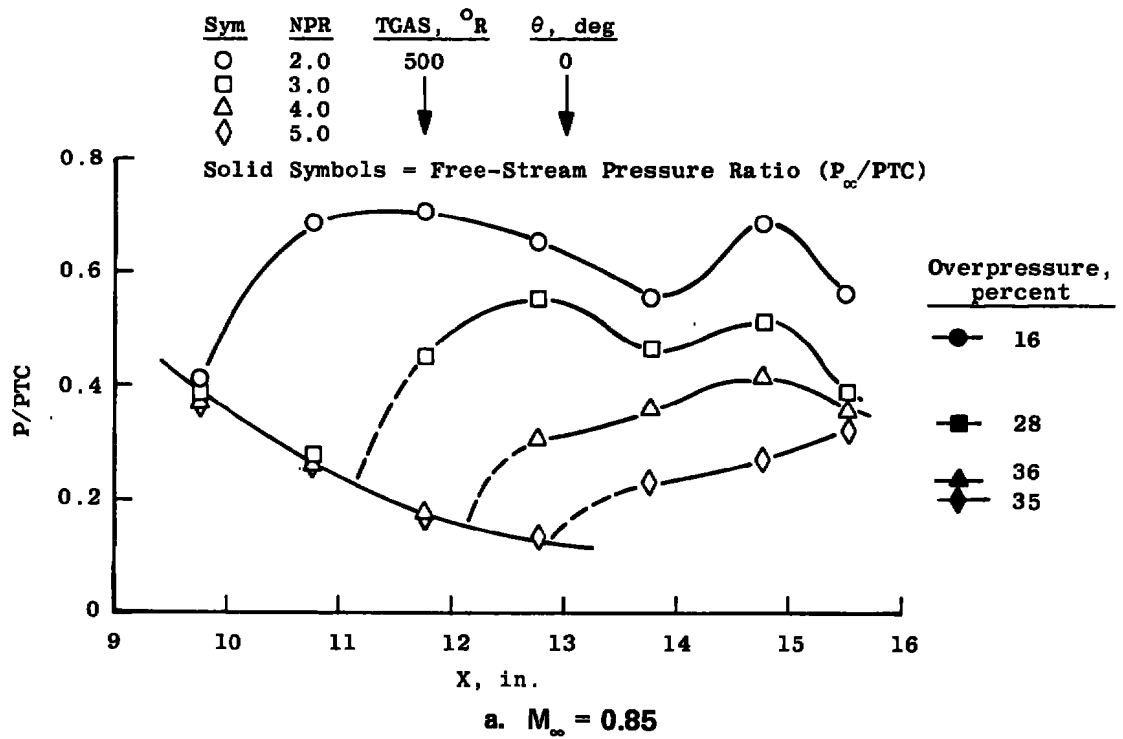


Figure 15. Effect of pressure ratio on pressure distribution, internal cowl surface.

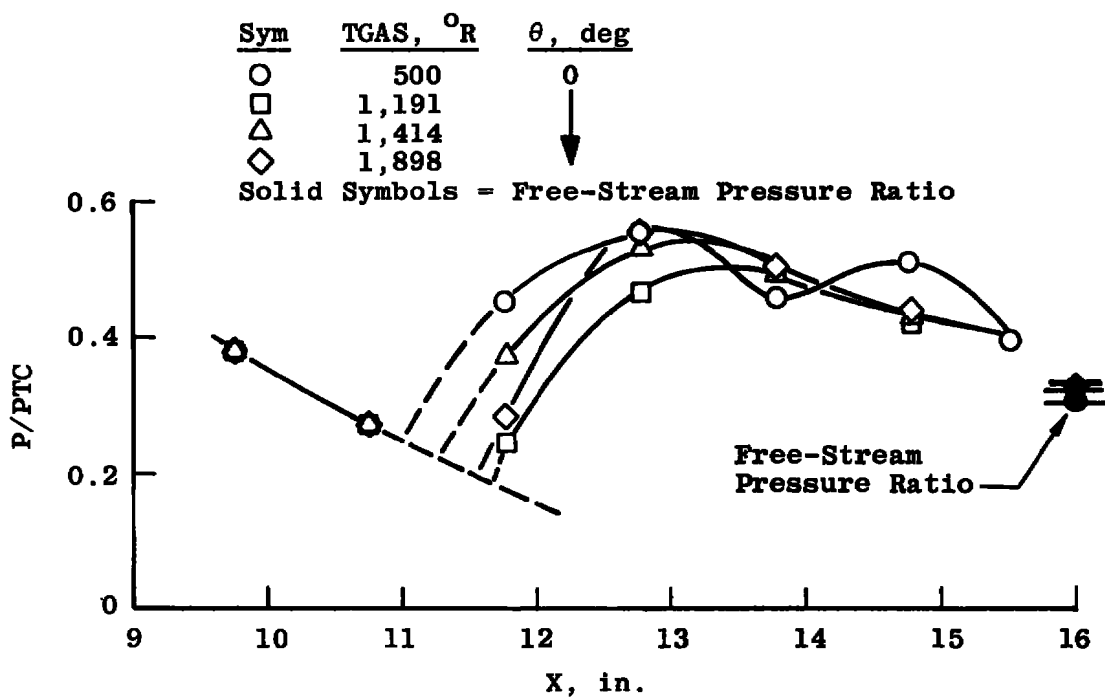
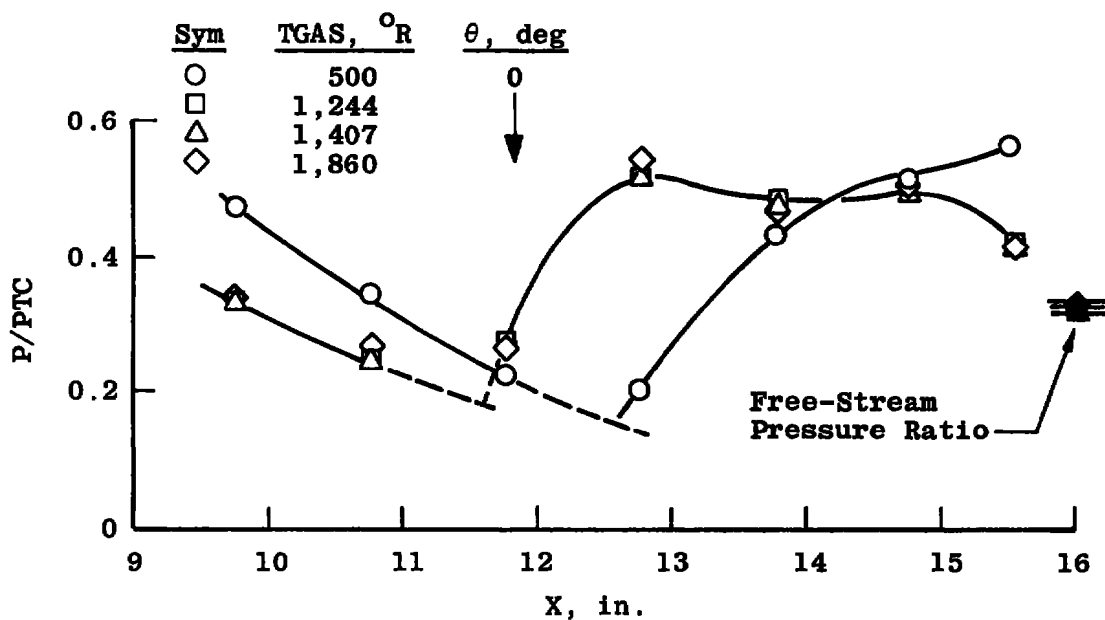
a. $M_\infty = 0.85$ b. $M_\infty = 1.40$

Figure 16. Effect of exhaust plume temperature on pressure distribution, internal cowl surface.

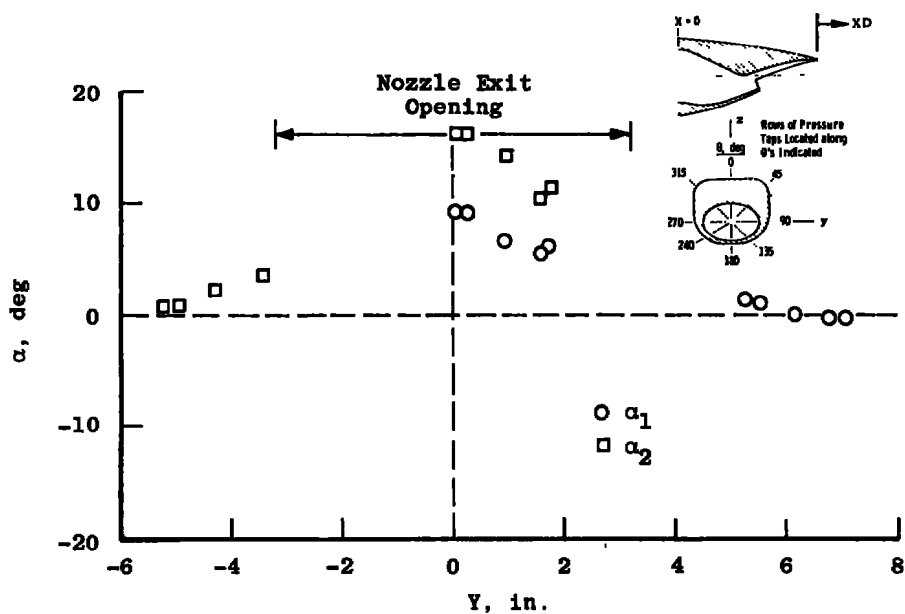
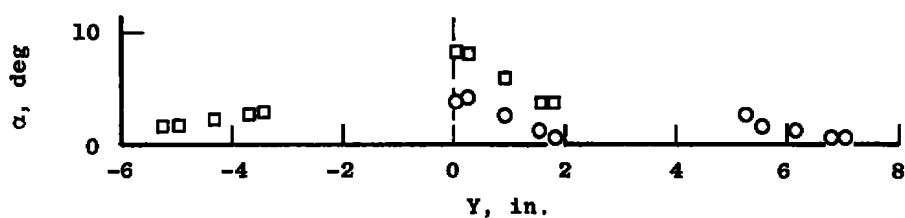
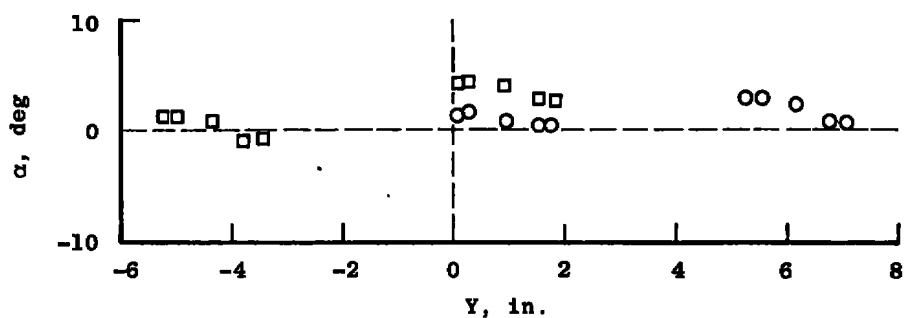
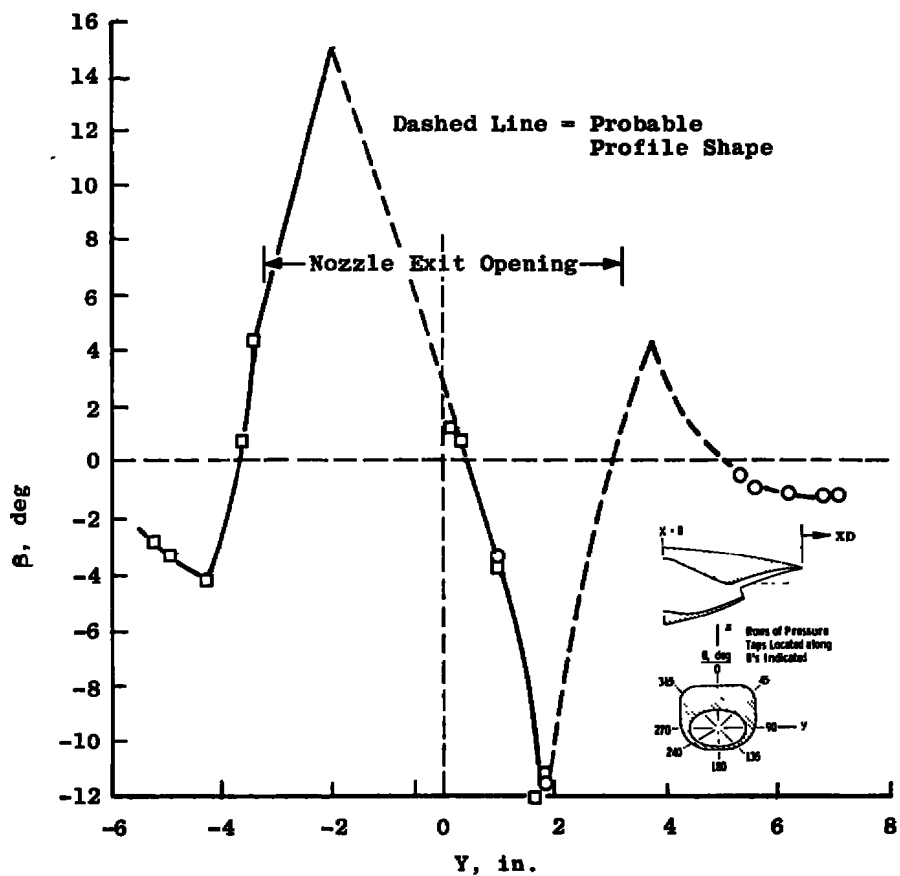
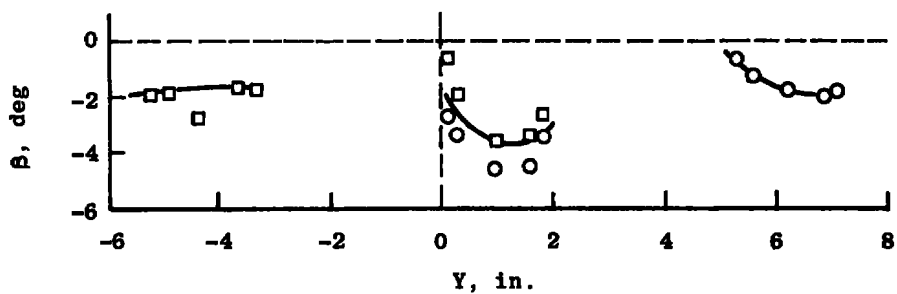
a. $XD = 1$ b. $XD = 9$ c. $XD = 21.7$

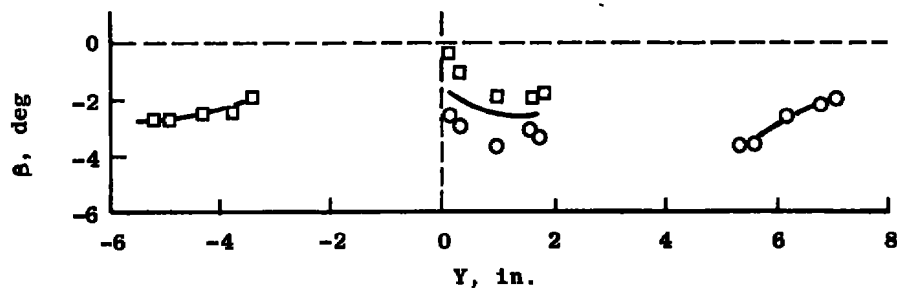
Figure 17. Flow angularity measured in the exhaust plume at three downstream locations, $M_\infty = 0.8$.



d. XD = 1



e. XD = 9



f. XD = 21.7

Figure 17. Concluded.

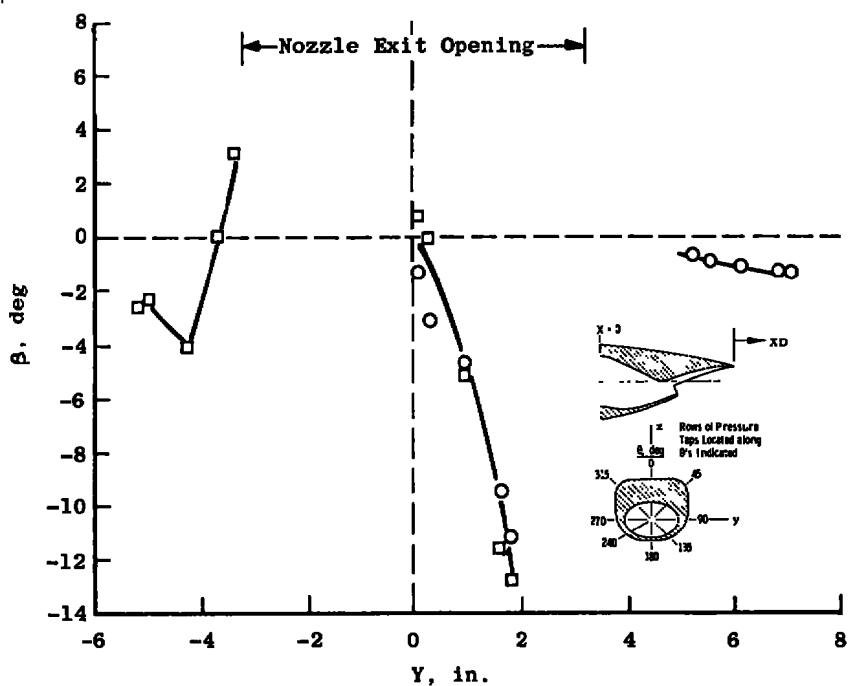
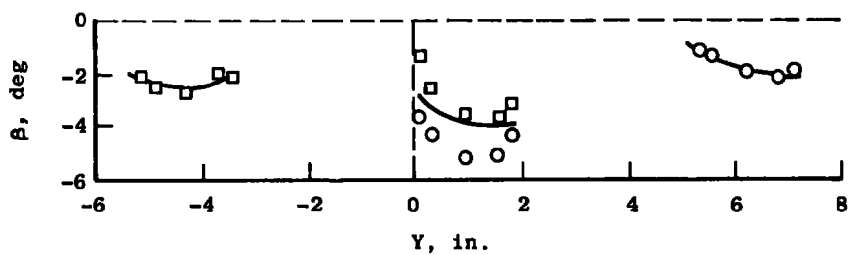
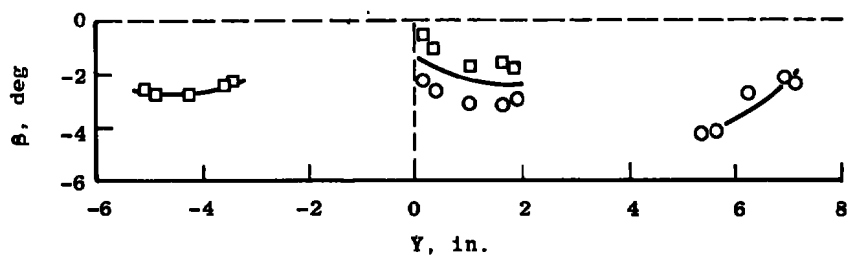
a. $XD = 1$ b. $XD = 9$ c. $XD = 21.7$

Figure 18. Flow angularity measured in the exhaust plume at three downstream locations, $M_\infty = 0.9$.

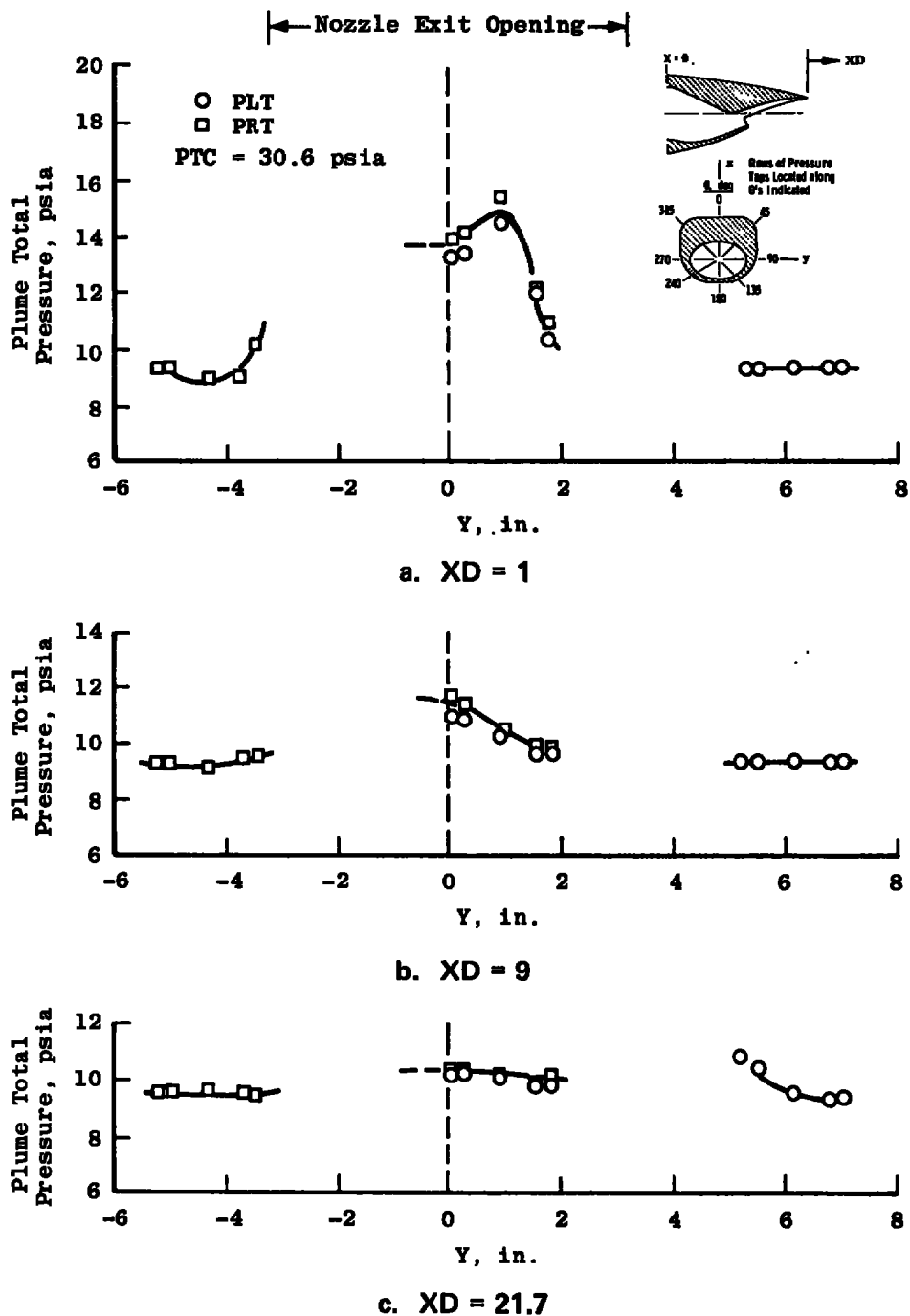


Figure 19. Total pressure profile of exhaust plume at three downstream locations, $M_\infty = 0.85$.

Table 1. Nozzle Afterbody Pressure Tap Locations
a. Nonaxisymmetric outside surface pressure instrumentation

Pressure Tap Location*	$\psi = 0$ deg	Pressure Tap Location	$\psi = 45$ deg	Pressure Tap Location	$\psi = 90$ deg	$\psi = 270$ deg	Pressure Tap Location	$\psi = 135$ deg
0.510	401	0.496	417	0.496	433	490	0.510	446
1.520	402	1.496	418	1.492	434	491	1.496	447
2.516	403	2.496	419	2.498	435	492	2.482	448
3.512	404	3.496	420	3.510	436	493	3.474	449
4.535	405	4.496	421	4.533	437	494	4.518	450
5.541	406	5.514	422	5.531	438	495	5.563	451
6.545	407	6.517	423	6.537	439	496	6.571	452
7.537	408	7.526	424	7.539	440	497	7.567	453
8.545	409	8.503	425	8.142	441	498	8.559	454
9.539	410	9.494	426	8.553	442	499	8.768	475
10.555	411	10.467	427	9.037	443	301	8.333	476
11.557	412	11.463	428	9.547	444	302		
12.565	413	12.447	429	10.293	445	303		
13.579	414	13.415	430					
14.579	415	14.392	431					
15.591	416	15.380	432					
14.500	479							
15.490	480							

*Measured in Inches from Model Station 141.359

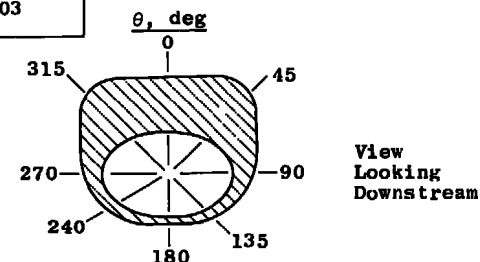


Table 1. Continued
a. Continued

Pressure Tap Location*	$\theta = 180$ deg	Pressure Tap Location	$\theta = 240$ deg	Pressure Tap Location	$\theta = 315$ deg
0.484	459	1.878	481	0.502	304
1.474	460	2.860	482	1.518	305
2.427	461	3.828	483	2.522	306
3.415	462	4.825	484	3.524	307
4.392	463	5.787	485	4.533	308
5.329	464	6.750	486	5.537	309
6.254	465	7.669	487	6.539	310
7.191	466	8.354	488	7.537	311
8.600	467	8.581	489	8.549	312
8.142	472	7.939	469	9.557	313
8.366	473	8.400	470	10.555	314
8.819	474	8.638	471	11.537	315
				12.524	316
				13.506	317
				14.498	318
				15.474	319

* Measured in Inches from Model Station 141.359

See Previous Page for Angular Orientation

Table 1. Continued
b. Internal Surface Cowl Pressure Instrumentation

Pressure Tap Location*	Row 1	Row 2	Row 3	Row 4	Row 5
9.246	—	—	—	222	224
9.740	201	208	215	—	—
10.246	—	—	—	223	225
10.746	202	209	216	—	—
11.748	203	210	217	—	—
12.756	204	211	218	—	—
13.755	205	212	219	—	—
14.754	206	213	220	—	—
15.565	207	214	227	—	—

*Measured in Inches from Model Station 141.359

NOTE: Row Location in Reference to Centerline (0 deg)

Row 1 - Centerline (0 deg)

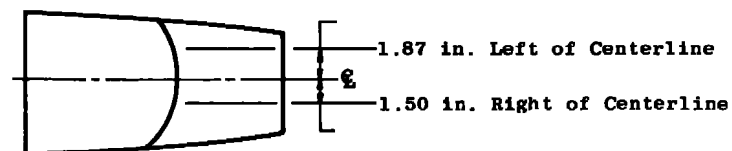
Row 2 - 1.50 in. Right of Centerline

Row 3 - 1.87 in. Left of Centerline

Row 4 - 1 in. Right of Centerline

Row 5 - 1.25 in. Left of Centerline

Views Looking Upstream



Bottom View

Table 1. Concluded
c. Nonaxisymmetric Internal Throat Static Pressure Taps

Model* Station, in.	Pressure Tap No.	Location Description
7.746	101	Upper Surface on Centerline (0 deg)
8.663	102	Upper Surface on Centerline (0 deg)
8.230	103	1 in. Right of Centerline Upper Surface
7.736	104	1.5 in. Right of Centerline Upper Surface
8.744	105	1.5 in. Right of Centerline Upper Surface
8.251	106	1.25 in. Left of Centerline Upper Surface
7.746	107	1.87 in. Left of Centerline Upper Surface
8.746	108	1.87 in. Left of Centerline Upper Surface
7.780	109	Side Surface Left (270 deg)
7.772	110	Side Surface Right (90 deg)
8.041	111	Lower Surface on Centerline (180 deg)
8.736	112	Lower Surface on Centerline (180 deg)
7.770	113	Lower Surface 1.0 in. Right of Centerline
8.705	114	Lower Surface 1.0 in. Right of Centerline
7.758	115	Lower Surface 1.87 in. Left of Centerline
8.685	116	Lower Surface 1.87 in. Left of Centerline

* Measured from Model Station 141.359

Table 2. Test Matrix
a. Nozzle Afterbody Performance Data

<u>Mach No.</u>	<u>Reynolds No./ft</u>	<u>Approximate Exhaust Plume Temp, °R</u>	<u>Remarks</u>
0	- 0 -	500	NPR Variable
0	- 0 -	500	
0.60	2.5×10^6	500	
↓		1,200	
↓		1,500	
↓		1,900	
0.70		500	
↓		1,200	
↓		1,500	
↓		1,900	
0.80		500	
↓		1,200	
↓		1,500	
↓		1,900	
0.85		500	
↓		1,200	
↓		1,500	
↓		1,900	
0.90		500	
↓		1,200	
↓		1,500	
↓		1,900	
1.20		500	
↓		1,200	
↓		1,500	
↓		1,900	
1.40		500	
↓		1,200	
↓		1,500	
↓		1,900	

Table 2. Concluded
a. Concluded

<u>Mach No.</u>	<u>Reynolds No./ft</u>	<u>Approximate Exhaust Plume Temp, °R</u>	<u>Remarks</u>
0.70	2.0×10^6	500	NPR Variable
↓	2.0×10^6	1,200	↓
	2.0×10^6	1,500	
	3.0×10^6	500	
↓	3.0×10^6	1,900	
0.60	1.15×10^6	500	↓

b. Exhaust Plume Gas Dynamics Data

<u>Mach No.</u>	<u>Reynolds No./ft</u>	<u>Axial Position Downstream from Nozzle Exit, in.</u>	<u>NPR</u>	<u>Exhaust Plume Temp, °R</u>
0.80	2.5×10^6	1	5.0	500
↓	↓	9	5.0	↓
		21.7	5.0	
↓		1	2.5	
0.90		1	5.0	
0.90	↓	9	5.0	
0.90	↓	21.7	5.0	↓

NOMENCLATURE

AREF	Maximum body cross-sectional area, in. ²
A θ	Delta area between adjacent pressure taps, in. ²
C	Coefficient for curve fit, Eq. (4)
CC	Coefficient for curve fit, Eq. (7)
CP	Pressure coefficient
CPD	Pressure drag coefficient
M $_{\infty}$	Free-stream Mach number
NPR	Nozzle total to free-stream static pressure ratio, PTC/P $_{\infty}$
PS	Static pressure, psia
PCS	Combustor static pressure, psia
PL1-4	Static pressure on hemispherical probe 1, psia
PLT	Total pressure on hemispherical probe 1, psia
PR1-4	Static pressure on hemispherical probe 2, psia
PRT	Total pressure on hemispherical probe 2, psia
PTC	Combustor total pressure, psia, calculated
q	Free-stream dynamic pressure
Sta	Model station, in.,
TGAS	Exhaust plume total temperature based on experimental results, °R
TTGAS	Theoretical exhaust plume total temperature, °R
X	Axial station on model, in.
XD	Distance downstream from nozzle exit plane, in.

Y	Horizontal distance from nozzle centerline, in.
Z	Vertical distance from nozzle centerline, in.
α	Exhaust plume flow angle in vertical plane, deg
β	Exhaust plume flow angle in horizontal plane, deg
γ	Ratio of specific heats
θ	Angular orientation of pressure tap rows, deg

SUBSCRIPTS

i	Individual pressure tap designation
∞	Free-stream conditions